Solveig Therese Eiane

CFD simulations in a blade cascade rig

June 2019

Master's thesis

2019

Master's thesis

Solveig Therese Eiane

NTNU
Norwegian University of
Science and Technology
Faculty of Engineering
Department of Energy and Process Engineering

NTNU
Norwegian University of
Science and Technology

NTNU
Norwegian University of
Science and Technology

NTNU
Norwegian University of
Science and Technology

CFD simulations in a blade cascade rig

Solveig Therese Eiane

MASTER THESIS

for

student Solveig T. Eiane

Spring 2019

CFD simulations in a blade cascade rig

CFD simuleringer i en bladkaskaderig

Background

A new design concept for hydrofoils operating in turbulent industrial flow regimes has been proposed. The design is intended to reduce the frequency and strength of the vortex shedding at the trailing edge, and mitigate some of the negative effects that this vortex shedding phenomenon gives, e.g increased fatigue in lock-in. The design concept has been numerically verified, though further computational fluid dynamics (CFD) simulations should be undertaken to compare the accuracy/computational cost relation of some state of the art turbulence models. To do this, a detailed comparison of Reynolds averaged Navier-Stokes (RANS) simulations comprising turbulence models, such as the Realizable k-epsilon or the Menter SST k-omega model, with that of turbulent scaling models such as in large eddy simulations (LES) or detached eddy simulations, should be conducted. Although the problem at hand is largely a fluid structure interaction (FSI) problem, the validity of the pure CFD approach selected in a FSI simulation must be thoroughly investigated. Once the CFD approach is validated, a comparison of a two-way FSI coupling vs a one way coupling for the hydrofoil in lock-in would be highly valuable for ongoing research.

For experimental validation of CFD results, a blade cascade rig in the Waterpower laboratory is used. An experimental investigation has been performed using Particle Image Velocimetry (PIV) techniques, a high-performance technique utilizing high-speed camera and laser illumination for determining the flow field characteristics.

Objective

The candidate shall perform and validate, with existing data, CFD simulations to determine the flow field characteristics behind the trailing edge of a hydrofoil in the blade cascade rig at the waterpower laboratory.

The following tasks are to be considered:

1. Literature review of state of the art CFD techniques and turbulence modelling, in particular formulations of detached eddy simulations (DES), and large eddy simulations (LES).
2. 3D RANS simulation of a reference hydrofoil with a two-equation turbulence model, complete with a grid and turbulence dependence study.

a. Herein a study of dependence on location of inlet boundary and turbulence parameters should be considered.

b. Comparison of fully turbulent RANS approach with a laminar to turbulent transition simulation, with emphasis on the developing boundary layer and consequent wake and shedding frequencies of the hydrofoil.

3. After an assessment of suitability with respect to time and computational resources, compare either a DES simulation or a LES simulation to RANS simulations of reference geometry.

4. If time: Compare the wake structure of DES/LES simulation of reference hydrofoil with a modified hydrofoil, with emphasis on wake structures and spectral analysis.

-- " --

The master thesis work comprises 30 ECTS credits.

The work shall be edited as a scientific report, including a table of contents, a summary in Norwegian, conclusion, an index of literature etc. When writing the report, the candidate must emphasise a clearly arranged and well-written text. To facilitate the reading of the report, it is important that references for corresponding text, tables and figures are clearly stated both places.

By the evaluation of the work the following will be greatly emphasised: The results should be thoroughly treated, presented in clearly arranged tables and/or graphics and discussed in detail.

The candidate is responsible for keeping contact with the subject teacher and teaching supervisors.

Risk assessment of the candidate's work shall be carried out according to the department's procedures. The risk assessment must be documented and included as part of the final report. Events related to the candidate's work adversely affecting the health, safety or security, must be documented and included as part of the final report. If the documentation on risk assessment represents a large number of pages, the full version is to be submitted electronically to the supervisor and an excerpt is included in the report.

According to "Utfyllende regler til studieforskriften for teknologistudiet/sivilingeniørstudiet ved NTNU" § 20, the Department of Energy and Process Engineering reserves all rights to use the results and data for lectures, research and future publications.

Submission deadline: 11 June 2019.

Department for Energy and Process Engineering, 10/01 2019

Pål-Tore Storli
Supervisor

Co-Supervisor(s): Kristian Sagmo

Acknowledgements

Solveig Therese Eiane
Trondheim, June 2019

Abstract

In this master thesis, computational fluid dynamics (CFD) simulations of a hydrofoil in the blade cascade rig at the Waterpower laboratory at the Norwegian University of Science and Technology (NTNU) have been conducted using ANSYS CFX. The purpose was to determine the flow field characteristics behind the trailing edge of the hydrofoil, with emphasis on the developing boundary layer and consequent wake and shedding frequency. The hydrofoil has a blunt, asymmetrical trailing edge, and the chord-based Reynolds number is $2.4 \cdot 10^6$. A fully turbulent 3D Reynolds-averaged Navier-Stokes (RANS) approach with the SST $k-\omega$ turbulence model has been compared with a laminar to turbulent transition simulation, where the $\gamma - Re_\theta$ transition model has been used in combination with the SST $k - \omega$ model. For the fully turbulent RANS approach, the dependence on location of inlet boundary and on turbulence parameters have also been investigated. The simulation results have been validated with existing data of both numerical and experimental origin. It is observed that the numerical simulations generally underpredict the vortex shedding frequency and the velocity deficit in the wake, and overpredict the width of the wake. The underpredicted shedding frequency suggests that the separation points of the boundary layer are estimated to lie too far upstream on the foil surface. It is also clear that the transition model produces a better estimate of the shedding frequency than the SST $k - \omega$ model manages alone, compared with experiments.

Sammendrag

I denne masteroppgaven har det blitt foretatt simuleringer i form av numeriske strømningsberegninger på en hydrofoil i bladkaskaderiggen på Vannkraftlaboratoriet ved Norges teknisk-naturvitenskapelige universitet (NTNU). Simuleringene har blitt utført med ANSYS CFX. Formålet har vært å bestemme strømnings-karakteristikkene nedstrøms for foilens avløpskant, med fokus på grensesjiktets utvikling og følgende vake og virvelavløsningsfrekvens. Hydrofoilen har en stump, asymmetrisk avløpskant og det korde-baserte Reynoldstallet er om lag $2,4 \cdot 10^6$. En rent turbulent tilnærming med 3D Reynolds-averaged Navier-Stokes (RANS) og SST $k - \omega$ turbulensmodell har blitt sammenlignet med en laminær-til-turbulent overgangssimulering, hvor $\gamma - Re_\theta$ overgangsmodell har blitt brukt i kombinasjon med SST $k - \omega$ turbulensmodell. For den rent turbulente RANS-tilnærmingen har også avhengigheten av innløpsgrensens plassering og av turbulensparametre blitt undersøkt. Simuleringsresultatene har blitt validert med eksisterende data av både numerisk og eksperimentell opprinnelse. Det observeres at de numeriske simuleringene generelt underestimerer virvelavløsningsfrekvensen og hastighet-sunderskuddet i vaken, og overestimerer vakens bredde. Underestimeringen av virvelavløsningsfrekvensen foreslår at separasjonspunktene til grensesjiktet er estimert til å ligge for langt oppstrøms på foilens over-flate. Man ser imidlertid at overgangsmodellen gir et bedre estimat på virvelavløsningsfrekvensen enn SST $k - \omega$ modellen klarer alene, sammenlignet med eksperimenter.

Contents

Nomenclature

Symbol	Description	Unit
A	Cross-sectional area	[m^2]
C	Courant number	[-]
D	Blade thickness at trailing edge	[m]
D_h	Hydraulic diameter	[m]
e_a	Approximate relative error	[-]
e_{ext}	Extrapolated relative error	[-]
f_s	Strouhal shedding frequency	[Hz]
GCI	Grid convergence index	[-]
I	Turbulence intensity	[-]
k	Turbulence kinetic energy	[m^2/s^2]
L	Characteristic length	[m]
N	Number of nodes	[-]
P	Mean pressure	[Pa]
p	Pressure	[Pa]
p'	Fluctuating part of pressure	[Pa]
p_m	Apparent order of method	[-]
Q	Mass flow rate	[kg/m^3]
r	Grid refinement factor	[-]
Re	Reynolds number	[-]
S	Source term	[-]
S_{ij}	Mean rate of strain	[1/s]
St	Strouhal number	[-]
T	Averaging interval	[s]
t	Time	[s]
Δt	Timestep size	[s]
U	Mean velocity in the x-direction	[m/s]
$\mathbf{U}$	Mean velocity vector	[m/s]
U_∞	Free stream velocity	[m/s]
u	Velocity	[m/s]
u'	Fluctuating part of velocity u	[m/s]
$\mathbf{u}$	Velocity vector	[m/s]
$\mathbf{u'}$	Fluctuating part of velocity $\mathbf{u}$	[m/s]
u_i	Velocity in i-direction	[m/s]
u_τ	Shear velocity	[m/s]
V	Mean velocity in the y-direction	[m/s]
v	Velocity in the y-direction	[m/s]
v'	Fluctuating part of velocity v	[m/s]
W	Mean velocity in the z-direction	[m/s]
W_{ref}	Reference velocity	[m/s]
w	Velocity in the z-direction	[m/s]
w'	Fluctuating part of velocity w	[m/s]
Δx	Cell length	[m]
x_i	x, y or z	[m]
y^+	Dimensionless wall distance	[-]

Greek letters

Symbol	Description	Unit
Γ	Diffusivity	[-]
γ	Intermittency	[-]
δ	Boundary layer thickness	[m]
δ_{ij}	Kronecker delta	[-]
ϵ	Dissipation rate of turbulence kinetic energy	[m^2/s^3]
μ	Dynamic viscosity	[kg/(m s)]
μ_t	Turbulent (or eddy) viscosity	[kg/(m s)]
ν	Kinematic viscosity	[m^2/s]
ρ	Density	[kg/m^3]
τ_{ij}	Reynolds stresses	[Pa]
τ_w	Wall shear stress	[N/m^2]
Φ	Mean part of scalar variable	[-]
ϕ	Scalar variable	[-]
ϕ'	Fluctuating part of scalar variable	[-]
ω	Turbulence frequency	[Hz]

Abbreviations

2D	Two-dimensional
3D	Three-dimensional
CFD	Computational Fluid Dynamics
DFT	Discrete Fourier Transform
DNS	Direct Numerical Simulation
FFT	Fast Fourier Transform
FLOP	Floating-Point Operation
HPC	High-Performance Computing
LES	Large Eddy Simulation
NASA	National Aeronautics and Space Administration
NTNU	Norwegian University of Science and Technology
NVKS	Norsk Vannkraftsenter
RANS	Reynolds-Averaged Navier Stokes
RMS	Root Mean Square
SGS	Subgrid-Scale
SST	Shear-Stress Transport
URANS	Unsteady Reynolds-Averaged Navier-Stokes

List of Tables

List of Figures

Chapter 1

Introduction

1.1 Background

For a long time, people have been using the force of water flowing in streams and rivers to produce mechanical energy. When the electrical power generation was invented, hydropower was one of the first energy sources to be used to generate electricity [42]. Since then, advancements have made hydropower a sophisticated technology, and today it is said to generate around 62 % of the renewable electricity share in the world, making it the major supplier of renewable energy [18]. In Norway, there has been continuous operation and development of hydropower systems for more than 110 years, with the result that more than 95 % of all Norwegian power production coming from hydropower today [15].

In a time where the future is uncertain in regards to climate change and sustainable growth, clean energy for all is one of the great and critical challenges. In response to this, the introduction of intermittent power production from wind and solar is increasing both in Europe and worldwide. This leads to a rapid development in the market demand for flexibility; to keep society on operation in a fully renewable energy system, it is important that energy storage, system services and capacity output is always available.

It is believed that hydropower has great potential to fulfill the role as a flexible player in the future energy system. It is a technology that is already employed and invested in, and it is highly effective and reliable. There are however some technological constraints that need to be lifted. Some electromechanical challenges must be solved, there is a need for better ways to predict fluctuations in the market, and flexible power production might lead to rapid variations in water flow and impact the environment further.

One of the challenges on the mechanical part is that the hydropower turbines should be able to operate well over a wider range than they traditionally have been designed for. This is necessary if they are going to respond quickly to the production from the intermittent energy sources and thus provide flexibility to the system, without having to compromise on their effectiveness. Limits are constantly being pushed with respect to increasing the performance of components, while at the same time reducing the costs of materials and manufacturing. This makes accurate prediction of component behavior more important, since safety and expected lifespan must be kept at acceptable levels.

For components which purpose is to transfer forces to or from fluids, there is a risk of pushing the components into designs where the structure and fluid are mutually changing the behavior of each other, due to different flow phenomena. One such phenomenon is the vortex shedding and the lock-in effect. In light of this, a new design concept for hydrofoils in the Francis turbine have been proposed. The intention of the new design is to reduce the strength and the frequency of the vortex shedding at the trailing edge, and thus mitigate some of the resulting negative effects, e.g. increased fatigue in lock-in. As a part of this work, one seeks to predict the interaction between the hydrofoil and the flow of water by simulations. This is largely a fluid structure interaction (FSI) problem, however, the validity of the pure computational fluid dynamics (CFD) approach selected in a FSI simulation should be thoroughly investigated.

1.2 The objective

The objective of this master thesis was to perform CFD simulations of flow over a reference hydrofoil located in the blade cascade rig at the Waterpower laboratory at the Norwegian University of Science and Technology (NTNU). The hydrofoil geometry is open to the public, available through the *Francis-99* project by Norsk Vannkraftsenter (NVKS). The simulation results have been used to determine the flow field characteristics behind the trailing edge of the hydrofoil and they have been validated with existing data. The existing data comes from the work of Sagmo et al. [33], and consists of both numerical and experimental results from the same hydrofoil as have been used in the numerical simulation of this master thesis. The numerical simulations, including meshing, have been performed in the software ANSYS CFX 19.2.

The flow that has been simulated has a Reynolds number of approximately $2.4 \cdot 10^6$, based on the chord length of the hydrofoil. The numerical simulations have been performed in 3D with the Reynolds-averaged Navier-Stokes (RANS) equations and a two-equation turbulence model, complete with a mesh independence study. Additionally, a study of dependence on the turbulence parameters and on the location of the inlet boundary have been conducted. Furthermore, a laminar to turbulent transition simulation has been performed, and the results from this have been compared with the results from the fully turbulent RANS approach. The comparison is focused on the developing boundary layer and the consequent wake and vortex shedding frequencies of the hydrofoil.

The suitability with respect to time and computational resources have also been assessed, to decide whether a detached-eddy simulation (DES) or a large eddy simulation (LES) of the reference hydrofoil should be performed and used for comparison with the RANS simulations. Also, if time and computational resources allowed for it, the wake structures and spectral analysis of a DES/LES simulation of the reference hydrofoil (in the blade cascade rig) should be compared with that of a modified hydrofoil. The modified hydrofoil has a new design that is intended to mitigate some of the negative effects the vortex shedding phenomenon can give. However, during the course of this master thesis, the availability of computational resources was reduced due to changes in the high-performance computing (HPC) resource regulations at NTNU, compared with what was expected to be available when the tasks were defined. This, in addition to some other factors related to the generation of a suitable mesh for DES/LES simulations and the limited time at hand, resulted in the DES/LES simulations being regarded as unsuitable to take on in this master thesis. Attempts were made, however, to design and generate a DES mesh, and the details related to this work are included in Appendix A.

A literature review of the state of the art CFD techniques and turbulence modeling has been conducted, and as a result of this, a brief review of the history of turbulence modeling and simulation is presented below. The review will in particular focus on formulations of DES and LES. Further, the theory and the numerical methods for the CFD simulations with the RANS approach are presented in Chapter 2 and Chapter 3, respectively. The numerical simulation results are presented and discussed in Chapter 4 and the work of the report is concluded in Chapter 5. Lastly, further work is presented in Chapter 6.

This master thesis is a continuation of the project work conducted by the author in the fall semester 2018. In said project work, CFD simulations were performed on the same hydrofoil with the same models as in this master thesis, but in 2D instead of 3D. The master thesis will therefore show similarities to this work. Especially Chapter 2 has some theory which is taken straight out of the project work, although with some rephrasing and alterations. In particular, this concerns Section 2.1, 2.2, 2.3 and 2.4, with the exceptions of 2.1.1, 2.3.3 and some paragraphs. The methodology presented in Chapter 3 also bears some resemblance to the corresponding chapter in the project work. The reader will be made aware of such sections throughout the report.

1.3 History of turbulence modeling and simulation

Most of the flows occurring in nature, like flow of water in rivers, water currents below the surface of the ocean, motion of cumulus clouds and interstellar gas clouds, are turbulent ([43], p. 40). This is also the case for flows in engineering applications: Boundary layers growing on aircraft wings and wakes of ships, submarines, cars and aircraft, are all examples of turbulent motion. The same goes for the flow that is studied in this master thesis.

Fluid flow is governed by the time-dependent Navier-Stokes equations, which contain all details of the complex turbulent motion. However, these equations cannot be solved analytically. Today, there are many ways for handling turbulence and its effects in flow calculations, using turbulence models or other CFD techniques.

In this section, a brief review of the history of turbulence modeling and simulation is given. As we will see, a great deal of the state of the art CFD techniques and turbulence modeling dates several decades back in time,
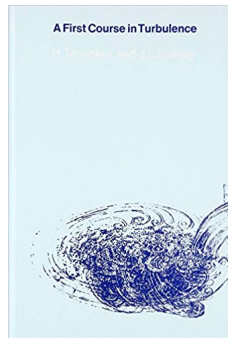
Figure 1.1: Cover of the book of Tennekes and Lumley [41] showing Leonardo da Vinci's sketch of turbulent flow.

relying heavily on the advances in computer technology. Details of the turbulence model used in this master thesis will be presented later on in Chapter 2. Needless to say, this brief review is not complete in its coverage of turbulence modeling, but aims to outline some of the most important elements from its history, with an emphasis on the techniques called LES and DES.

Early history

The existence and importance of turbulence was realized a long time ago. More than 500 years ago, Leonardo da Vinci sketched a variety of turbulent flows and used the term "la turbolenza" to describe it ([8], p. 427). One of his sketches is reproduced on the cover of the book of Tennekes and Lumley [41] from 1972, as shown in Fig. 1.1.

Systematic studies of turbulence were started in the second half of the 19th century. Osborne Reynolds carried out his pioneering work in the 1880s, deriving the Reynolds number for the onset of turbulence from experiments presented in his 1883 paper [30]. He also laid the foundations of the statistical treatment of turbulence in his paper [31] from 1895, which presented the decomposition of the flow into mean and fluctuating parts, leading to the averaged momentum equations. These are now known as the *Reynolds equations*, and the paper from 1895 is today seen as a mighty beacon in the literature of fluid mechanics ([8], p. 30).

A few years earlier, Joseph Boussinesq had proposed to use an artificially increased viscosity (turbulent or eddy viscosity) in the governing equations, as a way to treat the turbulence [2]. During the first decades of the 20th century, the knowledge on turbulence was advanced and simple models for accounting for its effects were proposed by several different scientists and engineers, primarily G.I. Taylor, L. Prandtl and Th. von Kármán [32]. There have been many attempts to review the history of turbulence research, e.g. *A Voyage Through Turbulence* (2011) [8] reviewing the contributions of several of the pioneers, "Turbulence before Marseille 1961" (2012) [11] reviewing the research of the first half of the 20th century, and "A Century of Turbulence" (2001) [23] reviewing the research of the last hundred years from when it was published. The intrigued reader is encouraged to look up these titles.

Before and after the computer

Before the advent of the computer in the 1960s, the turbulence effects were treated by empirical formulas in a crude and global manner, and it was only for simple, mostly one-dimensional, problems [32]. The empirical relations were found through experiments, aided by dimensional analysis. Examples of the empirical formulas and relations are the friction law introduced by Chezy in 1770, and the closely corresponding Darcy-Weissbach formula from the middle of the 19th century, which gives the dependence of a dimensionless friction coefficient on the Reynolds number and the wall roughness. Moody created a diagram in 1944 that shows this dependence in a general way and it became very popular [32].

The possibility of solving more complex problems was opened up by the advances in computer technology, which made it possible to solve the multidimensional differential equations that govern turbulent flow, numerically. Until the 1980s, it was only mean-flow equations, called the Reynolds-averaged Navier-Stokes (RANS) equations, that could be solved (with some exceptions) [32]. With RANS, one accounts for turbulence by a statistical turbulence model which does not resolve the actual turbulent motion, but determines the effect of it on mean quantities. The foundations of this statistical method was laid by Reynolds in 1895 [31].
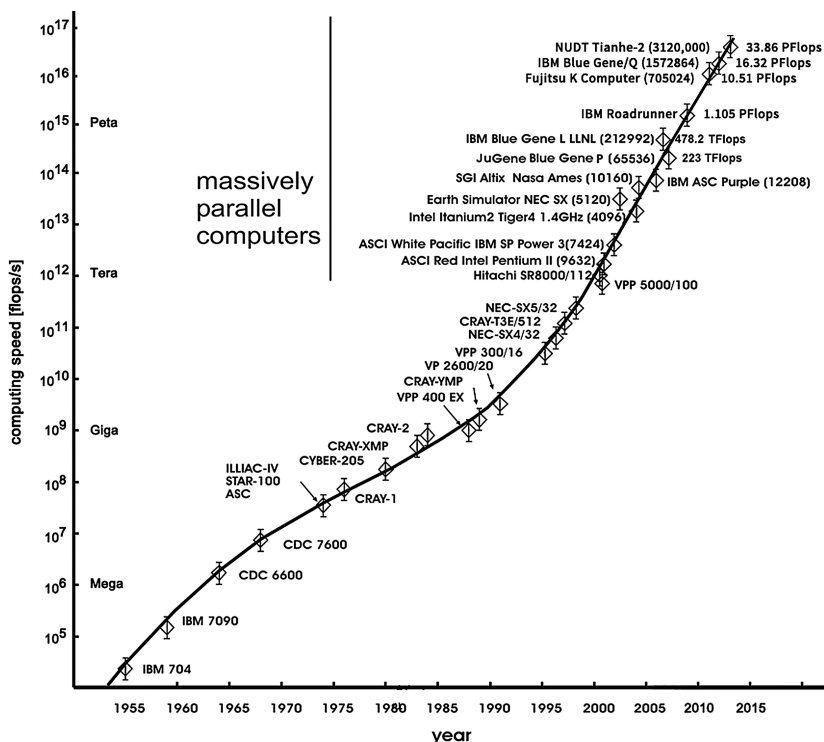
Figure 1.2: Computer speed development over the years. FLOPs are floating-point operations. Reprinted from [32].

As the computers were becoming more powerful, it became possible to solve the original time-dependent Navier-Stokes equations in a direct numerical simulation (DNS). A graph showing the computer speed development over the years is given in Fig. 1.2. The possibility of DNS was opened up primarily in the 1980s, but it had started already in the 1970s [32]. With DNS, one could resolve motions of all scales without the need of a model, at least for low Reynolds numbers and very simple configurations. Another method for more realistic situations, called large eddy simulations (LES), was also introduced and started to be applied in this period. LES resolves the turbulent motion only to the scale of the numerical grid, and leaves the fluctuating motion of the scale that is smaller than the mesh size to be modeled by a subgrid-scale model.

Determining the turbulence effects on mean quantities as RANS does is in many cases a sufficient approach, and it has modest computing requirements compared with DNS and LES [44]. Because of this, the RANS approach has become the backbone in the industrial CFD applications for the last few decades. In this approach, the appearance of some additional terms called turbulent or Reynolds stresses makes the flow governing equations no longer a closed problem, and there is a need for a turbulence model that can determine these stresses. Many different turbulence models have been developed throughout the years, and the most common are the mixing length model, the $k - \epsilon$ model, the $k - \omega$ model, the SST $k - \omega$ model, the Spalart-Allmaras model and the second moment closure model [32]. RANS methods are expected to be the primary workhorse in practical flow calculations for many years to come, and even though more advanced turbulence models than the ones listed above are available, they never became popular, at least in hydraulics.

In contrast to RANS, both DNS and LES have been too computationally expensive for industrial everyday use over the years, despite the increase in computer speed. It is expected that for practical calculations, the future will belong to hybrid methods of RANS/LES, due to the high computational cost of pure LES [32]. With DNS being more computationally heavy than LES, it has an even more pessimistic outlook regarding practical calculations in industry. For the rest of the historical review, LES and a hybrid method of RANS/LES will be explored more thoroughly.

LES and DES

The primary problem with computing turbulence numerically is the enormous range of scales that must be resolved [44]. Turbulence is a three-dimensional, unsteady phenomenon with a large range of scale motions,

and the size of the computational domain should at least be an order of magnitude larger than the scales that characterize the turbulence energy. For accurate simulation, the computational mesh needs to be fine enough to resolve the smallest length scale of dynamically significance, called the Kolmogorov micro-scale. DNS is the most accurate approach, and to be able to capture all the scales, from the smallest to the largest eddies, it must have a very fine mesh. This makes DNS very expensive, and today, it is still only applicable to flows with low Reynolds number over simple geometry.

Because of the prohibitively high computational cost that comes with resolving the small-scale dissipative motion in a DNS at larger Reynolds numbers, there was devised a method that resolves the eddies larger than the mesh element size on an affordable grid, and accounts for the unresolved small scales through a subgrid-scale (SGS) model [32]. This is the LES method, and it lies between RANS and DNS with respect to computing requirements. Since only the large eddies of the turbulent flow are computed directly, while the small scale motions are modeled, LES has a significantly lower computational cost compared with DNS. It is more expensive than the RANS approach, but it is also more accurate, because the large eddies contain most of the turbulent energy and are responsible for most of the momentum transfer and turbulent mixing [34].

While the Navier-Stokes equations are time-averaged in the RANS method, they are spatially filtered, which corresponds to spatial averaging, in LES [32]. The quantities that are solved for are then practically averages over mesh elements. The filtering/averaging process introduces stresses or fluxes which are attributable to the unresolved fluctuations, and they need to be determined by a SGS model. Most versions of LES have been formulated with an eddy-viscosity SGS model. This makes the governing equations formally identical to URANS equations based on an eddy viscosity, but with a much smaller eddy viscosity in the LES case. URANS is the unsteady mode of RANS for unsteady mean flows, such as vortex shedding flows, where the time-averaging is carried out only to remove the turbulent fluctuations and not the unsteadiness of the mean motion.

In LES, the eddy viscosity is related to quantities of the unresolved small-scale motion, which have a length scale that is given by the user-specified mesh size. In RANS on the other hand, the characteristic length scale must be determined by the turbulence model. As a result of this, there is no such thing as a mesh independent LES. A continuous refinement of the mesh will make the SGS viscosity become smaller and smaller until the LES turns into a DNS. Still, there are ways of assessing the mesh resolution quality for LES. One of these is presented in the paper "Index of resolution quality for large eddy simulations" by Celik et al. [5].

LES was proposed already in 1963 by meteorologist Smagorinsky [34] for atmospheric flow prediction, with the aim of simulating large-scale motions dominating the flow in the atmosphere [32]. It was first applied to engineering related flow in 1970 by Deardoff and in 1975 by Schumann [44]. In the beginning, from the 1960s to the middle of the 1980s, the development was slow with simple applications. After this, as the computing power increased, there was a rapid development and increase in the applications of LES. The applications shifted from simple to complex flows, such as heat transfer, aeroacoustic and multi-phase flow. This was not only due to the increased computational speed, but also the realization that RANS methods inherently cannot handle certain types of complex turbulent flow problems.

Today, LES is available in most of the commercial CFD software, and the emphasis in the applications is on complex configurations that have flow characteristics where the RANS approach has failed [44]. The industry interest in applying LES to complex engineering flows has been stimulated by the passing of several decades' development in LES and that massively parallel computers and affordable workstation clusters have become available. Still, LES has not replaced RANS, which continues to be the main computational analysis tool for practical engineering problems. This is mainly because of two reasons: for one, LES remains far too expensive computationally to be performed on a routine basis for practical engineering flow problems, even with the current computing power. Secondly, the maturity level of LES today still requires that the users have significant experience and knowledge to obtain results with the level of solution fidelity that can be expected. This is believed to be the case for the foreseeable future as well, where LES will not become a design tool for persons without extensive years of experience on LES techniques.

As mentioned above, pure LES has too high computational costs for use in practice, and the expenses are dominated by the required resolution of the boundary layers [35]. RANS on the other hand has much lower computational costs, but as mentioned earlier, it also has some shortcomings in the modeling of certain types of complex turbulent flow. These conflicts led to the introduction of the detached-eddy simulation (DES) by Spalart et al. [38] in 1997. DES combines LES and RANS, and was created to address the challenge of high-Reynolds number, massively separated flows, spurred by the belief that each of the methods cannot solve such problems alone [35]. RANS models are unable to predict large separation regions well, but can be adjusted to predict boundary layers and their separation adequately. By letting the boundary layer be treated by RANS and letting regions of massive separation be treated by LES, DES enjoys the advantages of the two methods,

and does so at a considerably lower cost than pure LES could obtain.

DES is essentially a three-dimensional unsteady approach that uses a single turbulence model, which functions as a SGS model in the regions where the grid resolution is high enough for an LES, and as a RANS model in the regions where it is not [39]. Initially, the Spalart-Allmaras eddy-viscosity model was used, but DES now draws on several other models as well for this purpose, like the Menter SST $k - \omega$ model. The switch between RANS and LES mode occurs when the length scale from the RANS model, basically the wall distance, becomes larger than the mesh size [32].

Since DES was first proposed in 1997, a DES community has formed, as well as new branches [35]. Several alternative formulations have been proposed, aimed at better fulfilling the original mission of DES. Some of these can be read about in the review of DES by Spalart from 2009, called "Detached-Eddy Simulation" [35]. It is said to be certain that DES has a future, and that under one name or another, a RANS/LES hybrid that is capable of full RANS function in the boundary layers will be used in many industries. As pure LES will mostly be too expensive, the future is seen to belong to hybrid methods for practical calculations [32].

Chapter 2

Theory

> *Most of the theory in Section 2.1, 2.2, 2.3 and 2.4, with the exceptions of 2.1.1, 2.3.3 and some paragraphs, is reproduced from the author's project work, although with some rephrasing.*

Fluid mechanics and computational fluid dynamics are large and complex fields, and for each problem to be solved, there are many theoretical aspects that should be considered. Here, some of the most essential theory to the study conducted in this master thesis will be presented.

2.1   Boundary layer dynamics

The boundary layer is a very thin region of flow near a surface where viscous forces and rotationality cannot be ignored ([7], s. 555). The boundary layer is laminar for low Reynolds numbers, but as we move downstream in the boundary layer, the Reynolds number will increase linearly with the length of it. This will eventually lead to a transition from laminar to turbulent flow, as shown in Fig. 2.1, where infinitesimal disturbances in the flow begin to grow and the boundary layer cannot remain laminar. This transition process is unsteady and difficult to predict, even with modern CFD codes.

It is favorable to have an accelerating flow, which is called favourable pressure gradient flow, because then the boundary layer is usually thin, hugs closely to the wall and is not likely to separate from it. When the flow is decelerating it is called adverse pressure gradient flow, and the boundary layer is usually thicker, does not hug closely to the wall and is much more likely to separate from it.

If the separated boundary layer reattaches downstream, a separation bubble is formed. Depending on the status of the boundary layer at separation and reattachment, the separation bubbles can be divided into three main types: laminar, transitional and turbulent [13]. For a laminar separation bubble, both separation and reattachment is laminar, while a turbulent separation bubble have turbulent separation and reattachment. For a transitional separation bubble, the separation is laminar and the reattachment is turbulent.
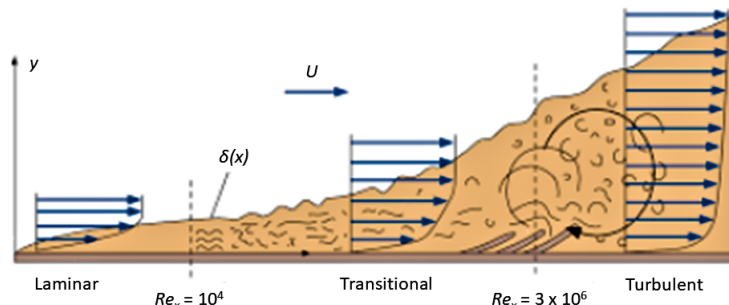
Figure 2.1: Boundary layer undergoing transition from laminar to fully turbulent on a flat plate (not to scale). Reprinted from [7].
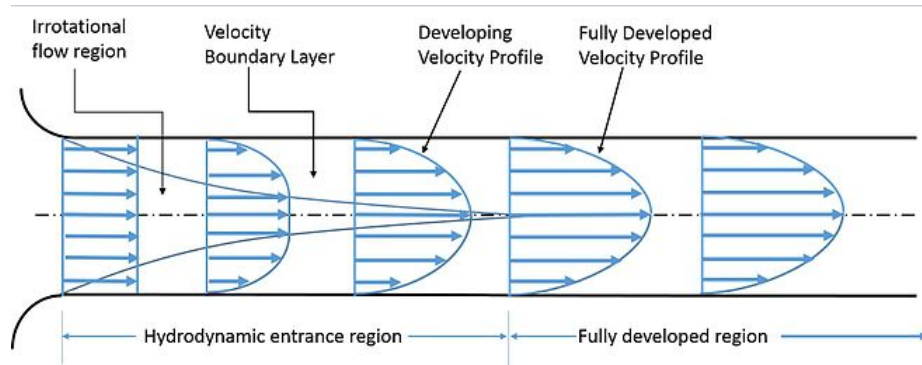
Figure 2.2: The development of the velocity profile for a fluid entering a pipe (here for laminar flow). Reprinted from [7].
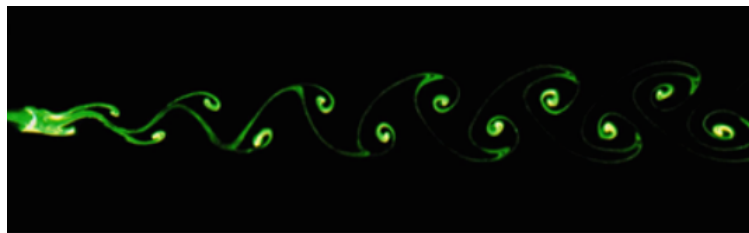
Figure 2.3: Dye visualization of a von Kármán vortex street caused by vortex shedding. Reprinted from [19].

2.1.1 Pipe flow

When fluid enters a circular pipe at a uniform velocity, boundary layers will start to develop at the pipe wall ([7], p. 351). The no-slip condition will make the fluid particles that are in contact with the wall come to a complete stop, and the fluid particles in the adjacent layers will gradually slow down due to friction. From this velocity reduction near the pipe wall follows an increase in velocity at the midsection of the pipe, to keep the mass flow rate through the pipe constant. In this way, a velocity gradient develops along the pipe.

The boundary layer thickness increases in the flow direction until it reaches the centerline and thus fills the whole pipe. This is illustrated in Fig. 2.2. A little further downstream of the point at which the boundary layer meet the centerline, the velocity profile becomes fully developed. The length of the pipe from inlet to where the velocity profile has become fully developed is called the hydrodynamic entry length, and the region of the pipe it covers is called the hydrodynamic entrance region. Beyond the entrance region is the hydrodynamically fully developed region.

Strictly speaking, the flow is said to be fully developed when both the velocity profile and the normalized temperature profile remains unchanged. If the fluid in the pipe is not heated or cooled and the temperature thus remains constant, the hydrodynamically fully developed flow is equivalent to the fully developed flow. In laminar flow, the fully developed velocity profile is parabolic, while in turbulent flow it is much flatter, or fuller, due to eddy motion and more mixing in the radial direction.

2.1.2 Vortex shedding

Vorticity is the rotating motion of an infinitesimally small fluid element, and for any object that is in relative motion to a real fluid, there will be generated vorticity in the boundary layers [16]. At some point along the upper and lower surfaces of the object the boundary layers must separate from it, and beyond these separation points the vorticity will cause the boundary layers to roll up into vortex spirals. This will happen at regular time intervals, where each vortex will be made up of a section of boundary layer. The vortices will originate alternately from the separation points on the upper and lower surfaces at a certain frequency, forming what is called a von Kármán vortex street in the wake. This is visualized in Fig. 2.3.

For each vortex that is shed, a transverse force will be exerted on the object. The direction of this force will change according to the alternately shedding vortices, causing the object to vibrate. Should the shedding frequency be in proximity of the natural frequency of the object, a lock-in effect may occur. The vortex shedding

frequency will then latch onto the natural frequency and stay equal to it over a range of flow velocities, as shown in Sagmo et al. [33], whereas the velocity-frequency relationship is generally linear elsewhere. In the state of lock-in, the vibrations of the object will be amplified due to the resonance effect, and for hydrofoils in hydropower turbines that operates in this range, premature fatigue or cracks might occur [3].

2.1.3 Empirical estimate for the shedding frequency

To estimate the shedding frequency empirically, one might use the traditional Strouhal shedding frequency f_s [40], defined as

$$f_s = St\frac{U_\infty}{D} \tag{2.1}$$

where St is the Strouhal number, U_∞ is the freestream velocity and D is approximated as the blade thickness at the trailing edge in this study, which is 4.8 mm. Details on the position for measuring this thickness is given in Chapter 3.2.4. Given the chord-based Reynolds number of $2.4 \cdot 10^6$, a commonly used value for the Strouhal number is $St = 0.22$ [14]. According to (2.1), the shedding frequency is then estimated to be $f_s = 440$ Hz.

2.2 Computational Fluid Dynamics

Computational fluid dynamics (CFD) is a very powerful technique that spans over a wide range of industrial and non-industrial application areas ([43], p. 1). It utilizes computer-based simulation to analyze systems involving fluid flow, heat transfer and associated phenomena such as chemical reactions. CFD codes are structured around numerical algorithms that are designed for fluid flow problems, and most commercial CFD software include sophisticated user interfaces to specify the problem parameters and to examine the results. CFD codes contain therefore usually three main elements; a pre-processor, a solver and a post-processor.

There are three types of numerical solution techniques for the solver: finite difference, finite element and spectral methods. ANSYS CFX uses the finite volume method, which is a special finite difference formulation that is central to most well-established CFD codes ([43], p. 3). One of the main attractions of the finite volume method is the control volume integration, which expresses the conservation of relevant properties for each finite size cell. This forms a clear relationship between the numerical algorithm and the underlying physical conservation principle.

For the treatment of convection and diffusion, which are the key transport phenomena, and the treatment of the source terms and the rate of change with respect to time, CFD codes contain suitable discretization techniques. Discretization, both in general and in ANSYS CFX, is briefly discussed below. The accuracy of CFD solutions is governed by the number of elements in the mesh, where a larger number of elements generally gives better solution accuracy. However, from a larger number of elements in the mesh follows a higher computational cost. Additional details for the mesh are also discussed below.

In solving fluid problems one must be aware that the results generated by a CFD code are at best as good as the physics embedded in it, and at worst as good as its operator ([43], p. 4). Prior to the CFD simulation, the flow problem must be identified and formulated in terms of the physical and chemical phenomena that need to considered. Successful simulation results require convergence and mesh independence, and the former of these can be assessed by the residuals, which are measures of the overall conservation of flow properties. The solution algorithm is iterative in nature, and when the residuals are very small, the solution is usually converged.

There are many opinions on how to assess convergence in a simulation, and the required level of convergence depends on the purpose of the simulation and the details of the model. The residuals are however considered the most important measure of convergence, because it relates directly to whether the equations have been solved accurately. ANSYS CFX uses normalized residuals to judge convergence, and some guidelines are given in the CFX-Solver Modeling Guide [1] regarding the residual levels. For the root mean square (RMS) residual level, a target value of 1e-04 is considered as a relatively loose convergence that may be sufficient for many engineering applications, a target value of 1e-05 gives a good convergence, and a target value of 1e-06 or lower is very tight and not possible to achieve in many cases. Another useful measure of convergence is quantities of interest that can be monitored during the run.

For the case at hand, which is prediction of the vortex shedding frequency from a blunt trailing edge, several researchers have indicated that there might be difficulties related to this kind of prediction due to the frequency's sensitivity to both tip geometry and the surrounding flow conditions affecting the boundary layers [16]. Modern CFD methods have however proven effective for trailing edges with sharp edges and clearly defined separation points [9].

2.2.1 Discretization

Discretization can be explained as the process of replacing a continuum with a finite set of points. In CFD, the Navier-Stokes equations must be replaced by algebraic approximations that can be solved using a numerical method. For the spatial discretization, ANSYS CFX uses an element-based finite volume method, where the mesh constructs finite volumes that are used to conserve quantities such as mass, momentum and energy [1].

Whenever continuous data is discretized, there will always be a discretization error. The ambition is for this to be small enough to be considered negligible for the simulation purposes at hand. The discretization error in space is usually reduced by refining the mesh, and the error in time by reducing the timestep, but both of these measures come with an increase in computational cost. By performing a mesh independence study one can estimate the discretization error [6]. A mesh independence study is generally a procedure of successive refinement of an initially coarse mesh until certain key results do not change.

2.2.2 Mesh

A good initial mesh design relies heavily on an insight into the expected properties of the flow ([43], p. 5). For this, a background in the fluid dynamics of the problem at hand and experience with meshing of similar problems may be of great help. The guide "Young-Person's Guide to Detached-Eddy Simulation Grids" from NASA [36] have been consulted to design the mesh in this master thesis. No detached-eddy simulation (DES) was performed in this work, however, much in the guidelines are applicable to the mesh design for the RANS simulations as well.

Depending on the turbulence model, there might be requirements to the near wall resolution of the mesh. This is usually done through specifications of the maximum value of the parameter y^+, defined as ([12], p. 298):

$$y^+ = \frac{u_\tau y}{\nu} \tag{2.2}$$

where y is the distance from the wall to the first node in the mesh, ν is the kinematic viscosity and u_τ is the shear velocity given by

$$u_\tau = \sqrt{\frac{|\tau_w|}{\rho}} \tag{2.3}$$

Here, τ_w is the shear stress at the wall and ρ is the density. y^+ is the dimensionless distance from a no-slip wall, and it is an indicator if the mesh is able to resolve the boundary layer appropriately. For ω-based turbulence models, a fine mesh with y^+ around 1 is recommended to obtain highly accurate simulations [1].

Another key parameter in CFD is the Courant number C, which is ([12], p. 146):

$$C = \frac{u\Delta t}{\Delta x} \tag{2.4}$$

where u is velocity, Δt is the timestep size and Δx is the cell length. The Courant number is related to the stability of the simulation, and the limit for it depends on the type of scheme that is used. For explicit schemes, the Courant number must be equal to or smaller than 1, while implicit schemes are unconditionally stable, meaning that there is no limit to the Courant number.

2.3 Turbulence and its modeling

In fluid dynamics, turbulence or turbulent flow can be described as a chaotic and random state of motion in which the velocity and pressure change continuously with time within substantial regions of flow ([43], p. 40). It is a result of excessive kinetic energy overcoming the damping effect of the fluid's viscosity. The dimensionless constant called the Reynolds number $Re = UL/\nu$, where U and L are characteristic velocity and length scales of the mean flow and ν is the kinematic viscosity, is an important quantity when it comes to predicting flow patterns. It describes the ratio of inertial forces to viscous forces. At low Reynolds numbers flows are laminar, but at higher Reynolds numbers they are observed to become turbulent.

Visualizations of turbulent flows reveal flow structures of rotational character, and these structures are called turbulent eddies. They have a wide range of length scales, with the largest turbulent eddies having a length scale comparable with that of the flow boundaries and the smallest having lengths of the order of 0.1 or 0.01 mm ([43], p. 42). The smallest scales of motion in turbulent flow are named the Kolmogorov microscales after the

Russian scientist who carried out pioneering work on turbulence structures in the 1940s. The largest turbulent eddies interact with and extract energy from the mean flow, while the smaller eddies are stretched strongly by somewhat larger eddies and more weakly with the mean flow. Kinetic energy is in this way handed down from large eddies to smaller and smaller eddies. This process is known as the energy cascade, and the kinetic energy associated with the smallest eddy motions is dissipated and converted into thermal internal energy.

Reynolds decomposition

Turbulence appears as random fluctuations of the flow variables about a mean value. These flow variables can for example be velocity components, pressure, temperature and density. To separate the mean and fluctuating parts of a quantity, one can use a mathematical technique called Reynolds decomposition. In a statistically steady flow, the Reynolds decomposition dictates that every variable can be written as the sum of a time-averaged value and a fluctuation about that value, here exemplified by some variable ϕ:

$$\phi(x_i, t) = \Phi(x_i) + \phi'(x_i, t) \tag{2.5}$$

where Φ is the time-averaged (or mean) part of ϕ and ϕ' is the fluctuating part. The former is identified as

$$\Phi(x_i) = \lim_{T \to \infty} \frac{1}{T} \int_0^T \phi(x_i, t) dt \tag{2.6}$$

where t is time. The averaging interval T must be large compared to the typical time scale of the fluctuations. A large enough T results in a Φ that is independent of the time at which the averaging started. However, if the flow is unsteady, we cannot use time-averaging as in (2.6). Instead, ensemble averaging is used to express Φ in (2.5):

$$\Phi(x_i, t) = \lim_{N \to \infty} \sum_{n=1}^{N} \phi(x_i, t) \tag{2.7}$$

where N is the number of ensemble members, which must be sufficiently large to eliminate the fluctuation effects. Tensor notation is used, where x_i (i=1,2,3) or (x, y, z) are the Cartesian coordinates. Here, the Einstein summation convention is adopted to achieve notational brevity. This convention implies summation over the range of an index whenever that index appears twice in any term.

The result of applying the Reynolds decomposition to the flow variables velocity $\mathbf{u}$ (and hence u, v and w) and pressure p is

$$\mathbf{u} = \mathbf{U} + \mathbf{u'} \qquad u = U + u' \qquad v = V + v' \qquad w = W + w' \qquad p = P + p'$$

Conservation principles

The motion of viscous fluid substances is described by mass conservation (the continuity equation) and the conservation equation for momentum, where the latter is also referred to as the Navier-Stokes equations. In a Cartesian coordinate system where the velocity vector $\mathbf{u}$ has x-component u, y-component v and z-component w, the instantaneous continuity and Navier-Stokes equations are as presented in (2.8) and (2.9a-c), respectively ([43], p. 24):

$$\text{div} \, \mathbf{u} = 0 \tag{2.8}$$

$$\frac{\partial u}{\partial t} + \text{div}(u\mathbf{u}) = -\frac{1}{\rho}\frac{\partial p}{\partial x} + \nu \, \text{div}(\text{grad}(u)) \tag{2.9a}$$

$$\frac{\partial v}{\partial t} + \text{div}(v\mathbf{u}) = -\frac{1}{\rho}\frac{\partial p}{\partial y} + \nu \, \text{div}(\text{grad}(v)) \tag{2.9b}$$

$$\frac{\partial w}{\partial t} + \text{div}(w\mathbf{u}) = -\frac{1}{\rho}\frac{\partial p}{\partial z} + \nu \, \text{div}(\text{grad}(w)) \tag{2.9c}$$

The equations are here expressed for a Newtonian fluid with no body forces, and where t stands for time, ρ stands for density, p stands for pressure and ν stands for kinematic viscosity.

The generic conservation equation of a scalar ϕ, also known as the transport equation for ϕ, is

$$\frac{\partial(\rho\phi)}{\partial t} + \text{div}(\rho\phi\mathbf{u}) = \text{div}(\Gamma \, \text{grad} \, \phi) + S_\phi \tag{2.10}$$

where Γ is the diffusivity for the quantity ϕ and S_ϕ is the source term ([43], 24).

Even though turbulent flows can be exactly represented by three-dimensional time-dependent Navier-Stokes equations, and that existing computer algorithms and programs are capable of solving them, the storage capacity of the computers is too small. The enormous range of scales to be resolved, with the smallest spatial scales being less than millimeters and the smallest time scales being milliseconds, makes it virtually impossible to predict the flow in detail ([20], p. 547). To make computer simulations of turbulent flows feasible, approximate methods have therefore been developed, and in the following text, one such method is presented.

2.3.1 Reynolds-averaged Navier-Stokes (RANS) equations

For engineering purposes, details of the fluctuations in turbulent flow are usually not necessary to resolve ([43], p. 66). Information about the time-averaged properties is almost always enough to satisfy CFD users. Because of this, most of the turbulent flow computations have been, and for the foreseeable future will continue to be, carried out using the Reynolds-averaged Navier-Stokes (RANS) equations. These are as follows ([43], p. 65):

$$\frac{\partial \rho}{\partial t} + \mathrm{div}(\rho \mathbf{U}) = 0 \tag{2.11}$$

$$\frac{\partial(\rho U)}{\partial t} + \mathrm{div}(\rho U \mathbf{U}) = -\frac{\partial P}{\partial x} + \mathrm{div}(\mu\,\mathrm{grad}\,U) + \left[-\frac{\partial \overline{(\rho u'^2)}}{\partial x} - \frac{\partial \overline{(\rho u'v')}}{\partial y} - \frac{\partial \overline{(\rho u'w')}}{\partial z} \right] \tag{2.12a}$$

$$\frac{\partial(\rho V)}{\partial t} + \mathrm{div}(\rho V \mathbf{U}) = -\frac{\partial P}{\partial y} + \mathrm{div}(\mu\,\mathrm{grad}\,V) + \left[-\frac{\partial \overline{(\rho u'v')}}{\partial x} - \frac{\partial \overline{(\rho v'^2)}}{\partial y} - \frac{\partial \overline{(\rho v'w')}}{\partial z} \right] \tag{2.12b}$$

$$\frac{\partial(\rho W)}{\partial t} + \mathrm{div}(\rho W \mathbf{U}) = -\frac{\partial P}{\partial z} + \mathrm{div}(\mu\,\mathrm{grad}\,W) + \left[-\frac{\partial \overline{(\rho u'w')}}{\partial x} - \frac{\partial \overline{(\rho v'w')}}{\partial y} - \frac{\partial \overline{(\rho w'^2)}}{\partial z} \right] \tag{2.12c}$$

Equation (2.11) and (2.12a-c) are the averaged continuity and momentum equations, respectively, for flows without body forces. The density ρ and the viscosity μ are considered as constants.

The RANS equations are the result of using the Reynolds decomposition in the continuity equation (2.8) and the Navier-Stokes equations (2.9a-c), and then taking the time average ([43], p. 63). From (2.6) it follows that the mean value of a fluctuation is zero, i.e. $\overline{\phi'} = 0$. As a result of this, averaging a linear term in the conservation equations simply gives $\bar{\phi} = \overline{\Phi + \phi'} = \overline{\Phi} + \overline{\phi'} = \Phi$. Averaging a quadratic nonlinear term on the other hand gives two terms:

$$\overline{u_i \phi} = \overline{(U_i + u'_i)(\Phi + \phi')} = U_i \Phi + \overline{u'_i \phi'} \tag{2.13}$$

The last term is a covariance and it is zero only if the two quantities are uncorrelated, which they seldom are in turbulent flows. A consequence of the averaging is therefore that some of the terms in the Navier-Stokes equations disappear, whereas some new ones appear.

When deriving the time-averaged transport equation for an arbitrary scalar quantity ϕ, like temperature, similar extra terms arise. The scalar transport equation is as follows ([43], p. 65):

$$\frac{\partial(\rho \Phi)}{\partial t} + \mathrm{div}(\rho \Phi \mathbf{U}) = \mathrm{div}(\Gamma_\Phi\,\mathrm{grad}\,\Phi) + \left[-\frac{\partial \overline{(\rho u'\phi')}}{\partial x} - \frac{\partial \overline{(\rho v'\phi')}}{\partial y} - \frac{\partial \overline{(\rho w'\phi')}}{\partial z} \right] + S_\Phi \tag{2.14}$$

Thus, the RANS equations contain terms such as $\rho\overline{u'_i u'_j}$, known as the *turbulent stresses* or *Reynolds stresses*, and the time-averaged transport equations contain terms such as $\rho\overline{u'_i \phi'}$, known as the *turbulent scalar flux*. One cannot represent these terms uniquely by using the mean quantities, and hence a closure problem arises, where the conservation equations contain more variables than there are equations. To take care of this closure problem, *turbulence modeling* is used.

2.3.2 Turbulence models

Turbulence models have been developed to model the Reynolds stresses and the turbulent scalar flux terms so that the system of mean flow equations (2.11), (2.12a-c) and (2.14) can be closed. To be useful in a general-purpose CFD code, the turbulence model must be simple, accurate, economical to run and have a wide applicability ([43], p. 66). The most common RANS turbulence models are, as mentioned in the history review in Section 1.3, the mixing length model, the $k - \epsilon$ model, the $k - \omega$ model, the SST $k - \omega$ model, the Spalart-Allmaras model and the second moment closure model [32]. They form the basis of standard turbulence calculation procedures in commercial CFD codes, and are classified based on the number of additional transport equations that need to be solved along with the RANS flow equations.

For the $k - \epsilon$ model, there are two transport equations that need to be solved; one for the turbulence kinetic energy $k = \frac{1}{2}(\overline{u'^2} + \overline{v'^2} + \overline{w'^2})$, and one for the dissipation rate of turbulence energy ϵ. Similarly, for the $k - \omega$ model, there is one transport equation for k and one for the turbulence frequency $\omega = \epsilon/k$ ([43], p. 90). The simulations in this study has been performed with the Menter SST $k - \omega$ turbulence model, which is a combination of these two models. The Menter SST $k - \omega$ model and the $\gamma - Re_\theta$ transition model, which has also been used, are presented below.

Menter SST $k - \omega$ model

Since the $k - \epsilon$ model has an unsatisfactory near-wall performance for boundary layers with adverse pressure gradients, Menter [25] suggested a hybrid model of the $k - \epsilon$ model and the $k - \omega$ model, called the shear-stress transport-model [25], or the Menter SST $k - \omega$ model ([43], p. 91). This model uses the standard $k - \epsilon$ model in the fully turbulent region far from the wall, and a transformation of the $k - \epsilon$ model into a $k - \omega$ model in the near-wall region. The Reynolds stress computation and the k-equation are the same as in Wilcox's original $k - \omega$ model, which means that the Reynolds stresses are computed with the Boussinesq expression ([43], p. 95):

$$\tau_{ij} = -\rho\overline{u_i'u_j'} = 2\mu_t S_{ij} - \frac{2}{3}\rho k\delta_{ij} = \mu_t\left(\frac{\partial U_i}{\partial x_j} + \frac{\partial U_j}{\partial x_i}\right) - \frac{2}{3}\rho k\delta_{ij} \tag{2.15}$$

Here, δ_{ij} is the Kronecker delta ($\delta_{ij} = 1$ if $i = j$ and $\delta_{ij} = 0$ if $i \neq j$), and μ_t is the turbulent or eddy viscosity. Further, the transport equation for k is as follows (where $\mathbf{U}$ has the three components U, V and W):

$$\frac{\partial(\rho k)}{\partial t} + \text{div}(\rho k\mathbf{U}) = \text{div}\left[\left(\mu + \frac{\mu_t}{\sigma_k}\right)\text{grad}(k)\right] + P_k - \beta^*\rho k\omega \tag{2.16}$$

where

$$P_k = \left(2\mu_t S_{ij}S_{ij} - \frac{2}{3}\rho k\frac{\partial U_i}{\partial x_j}\delta_{ij}\right) \tag{2.17}$$

and S_{ij} is the mean rate of strain

$$S_{ij} = \frac{1}{2}\left(\frac{\partial U_i}{\partial x_j} + \frac{\partial U_j}{\partial x_i}\right) \tag{2.18}$$

The ϵ-equation on the other hand, is transformed into an ω-equation by substituting $\epsilon = k\omega$, which gives ([43], p. 91)

$$\frac{\partial(\rho\omega)}{\partial t} + \text{div}(\rho\omega\mathbf{U}) = \text{div}\left[\left(\mu + \frac{\mu_t}{\sigma_{\omega,1}}\right)\text{grad}(\omega)\right] + \gamma_2\left(2\rho S_{ij}S_{ij} - \frac{2}{3}\rho\omega\frac{\partial U_i}{\partial x_j}\delta_{ij}\right) - \beta_2\rho\omega^2 + 2\frac{\rho}{\sigma_{\omega,2}\omega}\frac{\partial k}{\partial x_k}\frac{\partial\omega}{\partial x_k} \tag{2.19}$$

Since the original version of the model was suggested in 1992, there has been added some improvements to the model ([43], p. 91). Among these are revised model constants, where $\sigma_k = 1.0$, $\sigma_{\omega,1} = 2.0$, $\sigma_{\omega,2} = 1.17$, $\gamma_2 = 0.44$, $\beta_2 = 0.083$ and $\beta^* = 0.09$. Another improvement is the introduction of blending functions that are used to smooth the transition between the $k - \epsilon$ model and the $k - \omega$ model. Also, the eddy viscosity has been limited to improve the model's performance in flows with adverse gradients and wake regions, and the turbulent kinetic energy production has been limited to prevent the build-up of turbulence in stagnation regions ([43], p. 92).

For external aerodynamics, the Spalart-Allmaras, $k - \omega$ and SST $k - \omega$ models are all suitable turbulence models. However, tests suggest that the SST $k - \omega$ model gives superior performance for zero pressure gradient and adverse pressure gradient boundary layers ([43], p. 92). The SST $k - \omega$ model can also be used in combination with the $\gamma - Re_\theta$ transition model to improve the modeling of the laminar to turbulent transition. This has been done for some of the simulations in the study at hand.

$\gamma - Re_\theta$ transition model

The $\gamma - Re_\theta$ transition model was introduced by Menter, Langtry, Likki, Suzen, Huang and Völker [26] in 2004, and it aims at predicting the transition from laminar to turbulent boundary layer flow in general-purpose CFD methods. It was the first correlation-based approach to transition modeling that was designed specifically for modern CFD codes [24], and is based strictly on local variables. Before this model was introduced, there were no correlation-based methods for transition prediction that were compatible with modern unstructured, parallel CFD codes.

The $\gamma - Re_\theta$ transition model is based on two transport equations, one for intermittency and one for the transition onset criteria in terms of momentum thickness Reynolds number. These transport equations make no attempt to model the physics of the transition process like the turbulence models do. Instead, the physics of the transition process is contained entirely in the experimental correlations provided to the model. The correlations are typically based on freestream values such as the turbulence intensity or pressure gradient outside the boundary layer [26].

The two transport equations which the $\gamma - Re_\theta$ transition model consists of is written as [26]:

$$\frac{\partial(\rho\gamma)}{\partial t} + \frac{\partial(\rho U_j \gamma)}{\partial x_j} = P_{\gamma 1} - E_{\gamma 1} + P_{\gamma 2} - E_{\gamma 2} + \frac{\partial}{\partial x_j}\left[\left(\mu + \frac{\mu_t}{\sigma_f}\right)\frac{\partial\gamma}{\partial x_j}\right] \tag{2.20}$$

$$\frac{\partial(\rho\tilde{Re}_{\theta t})}{\partial t} + \frac{\partial(\rho U_j \tilde{Re}_{\theta t})}{\partial x_j} = P_{\theta t} + \frac{\partial}{\partial x_j}\left[\sigma_{\theta t}\left(\mu + \mu_t\right)\frac{\partial\tilde{Re}_{\theta t}}{\partial x_j}\right] \tag{2.21}$$

where (2.20) is the transport equation for the intermittency γ and (2.21) is the transport equation for the transition momentum thickness Reynolds number $\tilde{Re}_{\theta t}$. The constants are $\sigma_f = 1.0$ and $\sigma_{\theta t} = 10.0$. The definitions of the transition sources $P_{\gamma 1}$ and $E_{\gamma 1}$ and the destruction/relaminarization sources $P_{\gamma 2}$ and $E_{\gamma 2}$ in the intermittency equation, and the source term $P_{\theta t}$ in the equation for the transition momentum thickness Reynolds number, can be found in the paper "A Correlation-Based Transition Model Using Local Variables - Part I: Model Formulation" by Menter et al. [26], where the transition model was first introduced.

In the first years after the model was introduced, it did not manage to gain wide acceptance in the CFD community. This was because of two critical correlations that were deemed proprietary and had remained unpublished by the original authors, even though the model had been refined in later publications. Most CFD practitioners did not have the resources or expertise to develop such correlations, and thus, efforts were made by independent research groups to synthesize the two missing correlations. A group consisting of Malan, Suluksna and Juntasaro at the Suranaree University of Technology in Thailand proposed forms for these correlations in the paper "Calibrating the $\gamma - Re_\theta$ Transition Model for Commercial CFD" [24] in 2009, and they are believed to capture the essential behavior of the model. Malan et al. [24] successfully implemented the $\gamma - Re_\theta$ transition model in STAR-CCM+, which is another commercial CFD code, after a process of calibration using experimental data. In addition to proposing expressions tuned for STAR-CCM+ for the missing correlations, the research group also included sufficient information in their paper to guide others to perform similar calibration in other CFD codes.

In light of this, the formulation of the $\gamma - Re_\theta$ transition model in ANSYS CFX was investigated in this master thesis. Apart from the two correlations that were missing in the publications by the original authors, all the other details in ANSYS CFX's formulation of the model, including the model constants, are identical to what has been used by Malan et al. [24]. ANSYS CFX and Malan et al. [24] have used a refined formulation of the model, based on the papers [21] [22] [26] [27] by the original authors of the model. In fact, it turns out that the original authors of the $\gamma - Re_\theta$ transition model were employed by ANSYS CFX while they were working on it [17], which was an interesting finding to bear in mind when investigating how ANSYS CFX deals with the two missing correlations.

To close the $\gamma - Re_\theta$ transition model, there are three empirical correlations that must be expressed: $Re_{\theta t}$, $Re_{\theta c}$ and F_{length}. There have been proposed two correlations for $Re_{\theta t}$, one in the paper where the model was first introduced [26] and another one in the Dr.-Ing. thesis of Langtry [21]. The latter is used by both ANSYS CFX and Malan et al. [24]. The other two correlations, $Re_{\theta c}$ and F_{length}, are the originally missing correlations that initiated the work of Malan et al. [24]. They represent the momentum thickness Reynolds number where the intermittency starts to increase and the function to control transition length, respectively.

ANSYS CFX recommends the user to use the newest formulation by Menter and Langtry, as presented in their paper [22], in which they write about $Re_{\theta c}$ and F_{length}: "At present these empirical correlations are proprietary and are not given in the paper." Expressions for these empirical correlations are however given

in the documentation of ANSYS CFX so that the model is closed in the software. These expressions differ from what Malan et al. [24] found for $Re_{\theta c}$ and F_{length} to be used in STAR-CCM+. It is not clear from the documentation of ANSYS CFX whether they have used a similar calibration process as suggested by Malan et al. [24] or another method to find the two missing correlations , but since the original authors of the model proposal were employed by ANSYS CFX, it is expected that the expressions that are used make the model work as it was designed to.

2.3.3   Turbulence parameters in CFD software

The turbulence levels in a CFD-simulated flow is defined by turbulence parameters. These must be specified, either automatically with default values or manually, at an inlet boundary and for initialization of the domain ([43], p. 78). In ANSYS CFX, the turbulence parameters are turbulence intensity I, turbulence kinetic energy k, turbulence eddy dissipation ϵ, turbulence length scale L and viscosity ratio μ_t/μ [1]. From a general turbulence model point of view, an absolute minimum is to specify the boundary and initial conditions of k and ϵ, either directly or by specifying the turbulence intensity with the length scale or the viscosity ratio. Turbulence intensity I is defined as:

$$I = \frac{\mathbf{u}'}{\mathbf{U}} \tag{2.22}$$

where $\mathbf{U}$ represents the mean velocity and $\mathbf{u}'$ represents the velocity fluctuation. The turbulence kinetic energy is related to the turbulence intensity as follows:

$$k = \frac{3}{2}(\mathbf{U}I)^2 \tag{2.23}$$

In ANSYS CFX, the turbulence eddy dissipation ϵ is approximated at an inlet boundary using

$$\epsilon = \frac{k^{3/2}}{0.3D_h} \tag{2.24}$$

where D_h is the hydraulic diameter of the inlet. For initialization, the turbulence eddy dissipation can be specified manually as a function of the eddy length scale:

$$\epsilon = \frac{k^{3/2}}{L} \tag{2.25}$$

where L is the eddy length scale. The equations (2.22), (2.23) and (2.25) show that by specifying the turbulence intensity and the length scale, the values of k and ϵ can be calculated.

Specification of the eddy viscosity ratio μ_t/μ is an alternative way to enable the calculation of ϵ:

$$\epsilon = \frac{C_\mu k^2}{\nu(\mu_t/\mu)} \tag{2.26}$$

where C_μ is a non-dimensional constant and ν is the kinematic viscosity.

In the Solver Modelig Guide of ANSYS CFX, the user is advised to use the *Medium* option for the turbulence intensity in cases where the user has no idea of the turbulence levels [1]. This option corresponds to an intensity of 5%, and is a reasonable value for fully developed pipe flow. The allowable range of turbulence intensity is from 0.1 % to 10 %, which corresponds to very low and very high levels of turbulence, respectively.

When it comes to specifying an appropriate length scale, a fraction of the inlet hydraulic diameter is usually a good approximation for internal flows. The Solver Modelig Guide of ANSYS CFX and the book *Turbulent flows* by Stephen B. Pope([28], p. 242) is in agreement on this, both suggesting 1/3 of the hydraulic diameter, or 1/6 of the radius. Hence, the length scale for fully developed pipe flow in the case at hand is approximated as

$$L = \frac{1}{6}r = \frac{1}{6}150\text{mm} = 25\text{mm} \tag{2.27}$$

where r is the radius of the pipe at the inlet.

2.4 Fast Fourier Transform

To obtain the frequency of the vortex shedding in the flow, one can start by sampling a parameter that is affected by it over time. This might for example be the cross flow velocity at a point over which the vortices will travel, i.e. downstream of, and preferably close to, the trailing edge. The resulting oscillating data can be transformed to a representation in the frequency domain by using a technique called fast Fourier transform. This is presented below.

To transform a signal from its original domain, which is often time or space, to a representation in the frequency domain, one can use a Fourier analysis [29]. There are four different forms of Fourier transformation, and they are called the Fourier transform (FT), the Fourier Series (FS), the discrete-time Fourier transform (DTFT) and the discrete Fourier transform (DFT). These are applicable to different classes of signal, according to whether they are discrete or continuous and periodic or aperiodic. In this master thesis, the signal that is to be transformed is discrete and periodic, and hence the DFT is used. The DFT transforms a discrete, periodic time domain sequence into a discrete, periodic frequency domain representation.

The fast Fourier transform (FFT) is an algorithm that computes the DFT in a computationally efficient way [29]. Compared with a straightforward programming implementation of the DFT, it requires fewer multiplications, which is an advantage that increases with the length of the sample sequences involved. In digital signal processing, the FFT is one of the most commonly used operations, as it is applicable to filtering and spectrum analysis.

Chapter 3

Numerical Method

Considering the fact that much of the work performed in this master thesis bears resemblance to the work performed in the project work, with the main difference being that the simulations are conducted in 3D instead of 2D, there will also be similarities in the text describing the methodology.

The CFD simulations were performed in ANSYS CFX. Within this CFD software

- the geometry was uploaded and used to extract the fluid domain in the modeling application called SpaceClaim,

- the mesh was generated with the meshing tool ANSYS Meshing,

- the physical models for the simulations were selected in the preprocessor CFX-Pre,

- the simulations were run in the CFX-Solver,

- the results of the CFD simulations were visualized and analyzed quantitatively in the postprocessor called CFX-Post.

Most of the simulation results were also exported from ANSYS CFX and analyzed in Microsoft Office Excel and MATLAB. Before collecting the results, the iterative convergence was checked and a mesh independence study was conducted to estimate uncertainty due to discretization. Additionally, an investigation of the inflation layer thickness in the mesh, a study of dependence on location of inlet boundary and on turbulence parameters were conducted. In this chapter, the details of the work described above is presented.

3.1 Geometry and flow domain

The hydrofoil subjected to simulations in this master thesis was designed by Carl W. Bergan and Bjørn W. Solemslie at the Waterpower Laboratory at NTNU. Its geometry was inspired by one of the shapes (no. 4) tested in Heskestad and Olberts' [16] investigation of the influence of the trailing edge geometry on the hydraulic turbine blade vibration resulting from vortex excitation in 1960. The hydrofoil is installed in a blade cascade rig at the Waterpower laboratory, and a full overview of this can be viewed in Appendix B. The geometry of the hydrofoil is presented in Fig. 3.1. It is an open geometry, available to the public through the *Francis-99* project by NVKS.
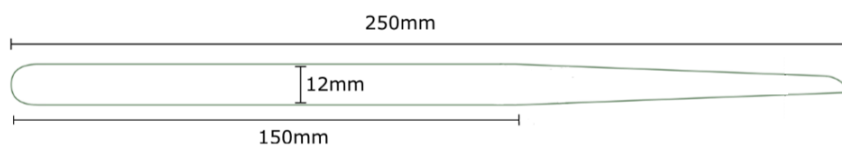

Figure 3.1: Hydrofoil geometry. The thickness of the trailing edge is illustrated in Fig. 3.6.
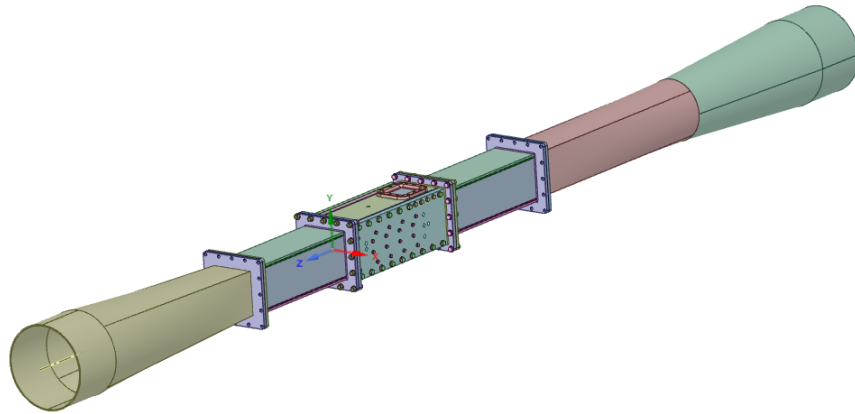
Figure 3.2: The geometry model of the blade cascade rig.
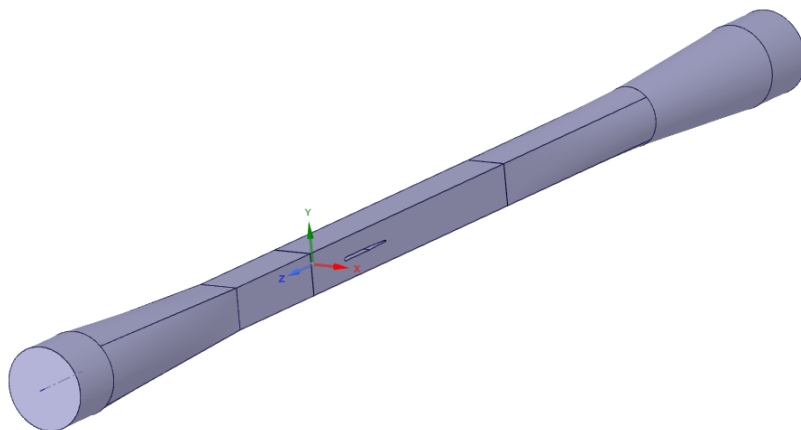

Figure 3.3: Flow domain after extracting it from the geometry model. The coordinate system showing x-, y- and z-directions according to this model will be used throughout the report.

Table 3.1: Basic settings for the simulations.

Parameter	Setting
Analysis type	Transient
Heat transfer	None
Fluid	Water
Reference pressure	1 atm
Timestep	1e-04 s

The flow domain used for the numerical simulations is based on a geometry model of the blade cascade rig, illustrated in Fig. 3.2. The flow domain was created in ANSYS SpaceClaim by extracting the fluid domain from the geometry model, and is shown in Fig. 3.3. It is divided into three different sections to allow for different types of mesh in different regions of the flow, where the middle section containing the hydrofoil is one of them, and the rest of the parts in the upstream and downstream end make out the two other sections. Also the geometries for the three bodies of influence for the mesh, i.e. regions for sizing control in the wake, were defined in ANSYS SpaceClaim. These are not visible in Fig. 3.3, but are located downstream of the trailing edge and will be presented in Section 3.3.

The original flow domain extracted from the geometry model had curved corners where the foil connects with the vertical walls. These were particularly challenging for the meshing program to work with, and hence they were replaced with straight corners. The flow domain in Fig. 3.3 has these straight corners where the foil meets the wall. According to Erik Os Tengs, this was also done for the flow domain used in the numerical simulations by Sagmo et al. [33], which results will be used as a basis for comparison. This modification of the flow domain is so small that it is not expected to have much effect on the simulated flow along the foil centerline in the middle of the pipe.

3.2 Numerical Setup

Most of the numerical setup in CFX-Pre are summarized in Table 3.1 and 3.2, which present the basic settings and the solver control settings, respectively. Some of the settings need more explanation than the others, and they are described in more detail below, as well as the rest of the numerical setup that is not given in the tables.

In Table 3.2, there are two settings listed for the turbulence numerics. The reason for this is that *First order* was used for the simulations with the SST $k-\omega$ model alone, while *High resolution* was used for the simulations with the SST $k-\omega$ model in combination with the $\gamma - Re_\theta$ transition model to improve the accuracy of the numerical model.

3.2.1 Timestep

The timestep was chosen based on the expected shedding frequency. From previous experiments, this was approximately 500 Hz, which corresponds to a period of $\frac{1}{500\text{Hz}} = 0.002$ s for the vortex shedding. To resolve the oscillations appropriately, it is necessary to have a timestep smaller than this. Taking this into account, a timestep of 1e-04 s was chosen. This should give about 20 timesteps per oscillation, which is regarded as an adequate resolution for the problem at hand.

The Courant number in the region of interest for this study was investigated for the given timestep and mesh (which will be presented in Section 3.3). The spatial average of the Courant number in a spherical volume with center at $z = 9.4D$ downstream of the trailing edge along the centerline, and with a radius of $10.4D$, was 0.7338 for a timestep of 1e-04 s. The root-mean-square (RMS) Courant number for the whole flow domain was approximately 5.30.

Table 3.2: Solver control settings for the simulations.

Parameter	Setting
Advection scheme	High resolution
Transient scheme	Second Order Backward Euler
Turbulent numerics	First order / High resolution
Coefficient loop minimum	2
Coefficient loop maximum	5
Residual target	1e-04

3.2.2 Turbulence models and wall functions

The Menter SST k-ω turbulence model was used for all the simulations, both with and without the $\gamma - Re_\theta$ transition model. In combination with this turbulence model, the only possible wall function setting in CFX-Pre is the one called *Automatic*. That is the default wall function for all models based on the ω-equation in ANSYS CFX, and it switches automatically from wall functions to a low-Re near wall formulation as the mesh is refined [1].

The default settings in ANSYS CFX for the $\gamma - Re_\theta$ transition model were investigated to check if the model constants were set correctly. ANSYS CFX-Solver Theory Guide was consulted for this, in addition to the paper "Transition Modeling for General CFD Applications in Aeronautics" by Langtry and Menter [22]. After examination, it was concluded that the default coefficients values in ANSYS CFX made the model match what is presented in the paper by Langtry and Menter. Hence, the default settings were applied for the simulation.

3.2.3 Boundary conditions and initial conditions

The inlet boundary condition was a mass flow rate of 216.6 kg/s in combination with medium turbulence intensity, corresponding to 5 %. The mass flow rate at the inlet was chosen to give a velocity of 9.6 m/s across the test section, based on a water density of 997 kg/m^3. The velocity 9.6 m/s will be used as the reference velocity W_{ref} for the normalization of the velocity profiles throughout the report. The walls and the hydrofoil surface were set as smooth walls with no-slip condition. Lastly, the outlet boundary condition was set to 0 Pa in relative pressure.

It can be noted that due to the no-slip condition on the walls, the actual average velocity across the test section were a little bit higher than 9.6 m/s. It was more in the range of 9.8 m/s. The mass flow rate at the inlet was calculated based on continuity with

$$W = \frac{Q}{A} \tag{3.1}$$

where W is the velocity (m/s), Q is the mass flow rate (kg/m^3) and A is the cross-sectional area (m^2). This does not take into account the effect of the no-slip condition on the walls, which makes the flow perceive a smaller A than with full slip. With a smaller A, W will be higher if Q is kept constant, which was the case in this scenario.

For the initialization of the transient simulation, the case was first run as a steady state simulation until convergence. This is a measure to make the transient simulation reach convergence quicker. For the steady state simulation, the same boundary conditions as specified above were applied, and the domain was initialized with the velocities $U = 0$ m/s, $V = 0$ m/s and $W = -3.06$ m/s (coordinate system is given in Fig. 3.3), a relative static pressure of 0 Pa and 5 % turbulence intensity. The transient simulation was then initialized with the results from the last iteration of the steady state simulation.

3.2.4 Output control and monitor points

The key variables for the objective of the study are the vortex shedding frequency and the velocity profile in the wake of the hydrofoil. The shedding frequency was obtained by using a fast Fourier transform on the time-signal of the velocity V in y-direction, measured at a distance 25 mm downstream of the trailing edge along the hydrofoil centerline. This is the first of the three monitor points in the wake from the trailing edge, as
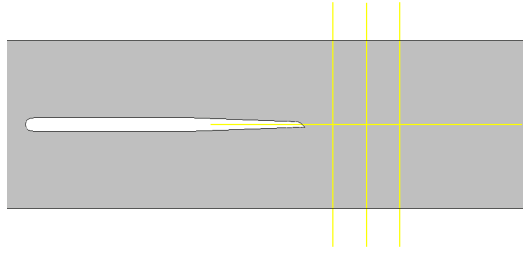
Figure 3.4: The three points in the wake at which the velocity V was monitored during the simulation. Positions downstream of the trailing edge: $z = 25$ mm, $z = 55$ mm and $z = 85$ mm, all along the hydrofoil centerline.
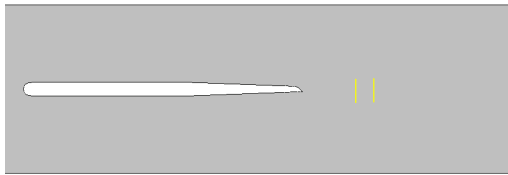
Figure 3.5: The two vertical lines for measuring the time-averaged streamwise velocity profile in the wake at $z = 9.9D$ and $z = 13.3D$ downstream of the trailing edge. D is the trailing edge thickness, $D = 4.8$ mm.

presented in Fig. 3.4. The shedding frequency and amplitude will be presented later in the report in frequency amplitude spectra, and these are obtained by performing a P.D. Welch power spectrum analysis in MATLAB. The MATLAB script is given in Appendix C.

The velocity profiles for the time-averaged streamwise velocity W are obtained at two vertical lines, $z = 9.9D$ and $z = 13.3D$ downstream of the trailing edge, as illustrated in Fig. 3.5. D is the trailing edge thickness of 4.8 mm, measured at the point where the curved surface starts, see Fig. 3.6. Nearly all of the velocity profiles presented in this report are obtained at either one of these two, except some of the velocity profiles in the dependence studies, as will be presented in Section 3.6 and 3.7.

3.2.5 Hardware

The main part of the simulations that were to be performed in this master thesis needed a great deal of computational power. For this purpose, a high-performance computing (HPC) resource at NTNU called the Idun cluster was used. To run a simulation in ANSYS CFX on Idun, a job script was sent to Idun, containing all the commands and instructions needed to perform the simulation. An example of such a job script used in this master thesis is found in Appendix D.
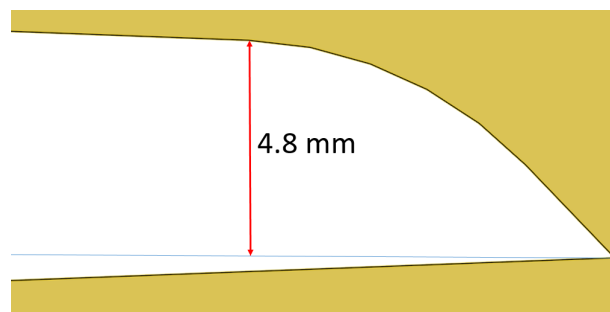
Figure 3.6: Trailing edge geometry. The thickness D of the trailing edge is measured at the point where the curvature starts on the upper surface, $D = 4.8$ mm.
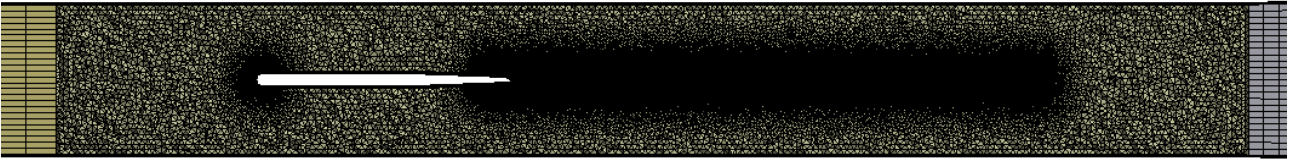
Figure 3.7: Mesh in the test section along the centerline of the volume, showing whole mesh elements.

Figure 3.8: Mesh at the trailing edge, showing whole mesh elements.

3.3   Mesh

The mesh was created in ANSYS Meshing and consists of 37 720 629 nodes. Three meshing methods are used: *Tetrahedrons*, *Sweep* and *MultiZone*. The mesh in the test section containing the hydrofoil is created with the meshing method *Tetrahedrons* in combination with the Patch Conforming Algorithm, constructing a mesh with tetrahedral elements in this part of the domain. The test section mesh is shown in Fig. 3.7, and the details of the mesh around the trailin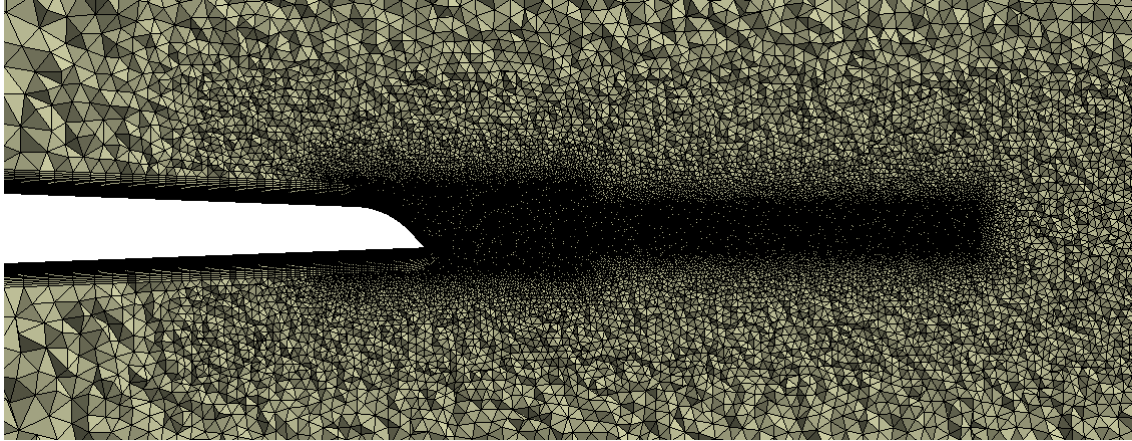g edge of the foil is shown in Fig. 3.8. Three bodies of influence cover the trailing edge and the wake to ensure high resolution of the mesh in the area where separation is expected to happen and where the vortices will travel. These can be seen in Fig. 3.7 and Fig. 3.8. In the former, only the largest of the three bodies of influence is visible, and it can be identified as the refined mesh stretching downstream of the trailing edge. The other two bodies of influence are smaller and located at the trailing edge, and are only visible in Fig. 3.8. The mesh presented in these figures is referred to as the *fine mesh* in the mesh independence study later on in the report.

In Fig. 3.8, one can observe that the second body of influence is narrower than the first body of influence, when it ideally should have been wider. This was done to expand the high resolution further downstream, without adding too many extra nodes to the mesh. The obvious disadvantage of this solution is the nature of the vortices, which will have information traveling in y-direction at a greater rate than undisturbed flow would have, and in an expanding fashion as they move downstream. If some part of a vortex is covered by a coarser mesh than the rest, the effect of the coarseness, i.e. larger levels of error, will propagate into the finer mesh, and possibly reduce the quality of the calculations there. Fig. 3.9 shows the instantaneous velocity field in the wake plotted with the mesh lines, and hence how the von Kármán vortex street is moving outside of the second body of influence.

However, with the given time and computational power, this solution appeared to be one of the most economical ways to increase the mesh resolution further downstream of the trailing edge. The growth rate is ensuring a gradual transition from the finer part of the mesh to the coarser. It is believed that even though the solution is not optimal, it is making a positive contribution to the quality of the mesh.

Another detail of the mesh close to the hydrofoil is the lower resolution along the upper and lower side of the foil compared with the higher resolution near the leading and trailing edge. This is another way to save nodes in the mesh, but it is not as questionable as the one discussed above. The paper "Young-Person's Guide to Detached-Eddy Simulation Grids", written by Phillipe R. Spalart and published by NASA [36], presents guidelines for mesh design, not only for detached-eddy simulations, but also for RANS simulations. In this
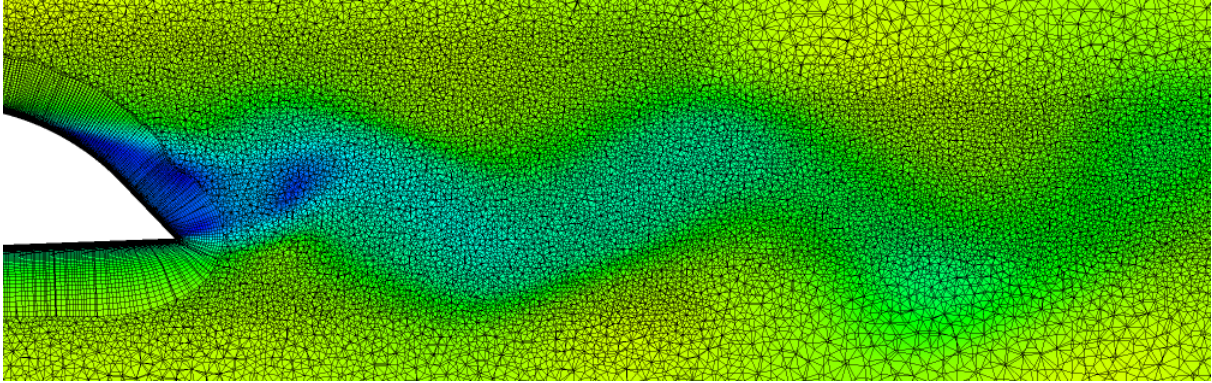
Figure 3.9: Mesh at the trailing edge with the instantaneous velocity plotted in the background, not showing whole mesh elements.
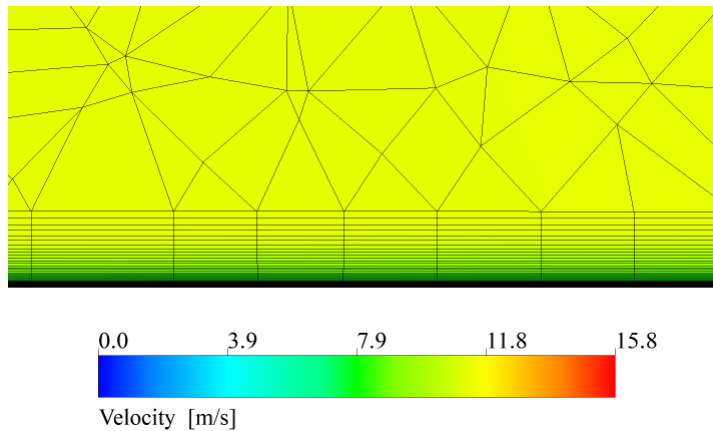
Figure 3.10: Inflation layers on the hydrofoil, not showing whole mesh elements.

paper it is stated that for simulations of flow over a foil, the spacing parallel to the surface is not constrained in wall units (Δx^+ is unlimited), except at surface singularities such as the trailing edge. Spalart writes that in these areas, there is little reason why the spacing should differ from the mesh further out in the flow. This has to do with how the flow behaves in these regions; apart from the boundary layer development along the foil surface, there is little change happening in the flow. Hence, as long as the boundary layer is captured by the inflation layers in the direction normal to the surface, there is no other requirements for high resolution of the mesh in this particular region, and this can be be seen implemented for the mesh at hand in Fig. 3.7.

The inflation layers on the hydrofoil are specified by a first layer height of 1e-06 m, a growth rate of 1.1 and a maximum number of layers being 59. This corresponds to a total thickness of 2.8 mm, which was decided through the investigation conducted in Section 3.3.1. The inflation layers on the hydrofoil surface are shown in Fig. 3.10, presented with the velocity contour plot in the background. With the given settings, the boundary layer on the hydrofoil should be covered by and resolved within the inflation layers. When the simulation is to be run with the $\gamma - Re_\theta$ transition model, it is recommended to apply meshes with $y^+ < 1$ [27]. Therefore, the settings were chosen to satisfy this, giving a maximal y^+ value of 0.9472 at the leading edge and ≤ 0.5 at the trailing edge. When the y^+ on the hydrofoil is this low, the mesh is able to resolve the boundary layer appropriately without the need for wall functions. For the surfaces in the rest of the domain, i.e. the pipe walls, there is in this study no need to have the same high resolution in the inflation layers. However, the same inflation layers settings were applied to the walls as to the foil surface, due to appearance of meshing challenges otherwise.

For the rest of the domain, i.e. upstream and downstream of the already discussed test section, the meshing methods *Sweep* and *MultiZone* were applied, respectively. When selecting the *Sweep* method, a swept mesh is forced on "sweepable" bodies, and if this is not possible, the mesher will fail. The requirements for a sweepable body is that there is no completely contained internal void, a source and target pair connected by edges or closed

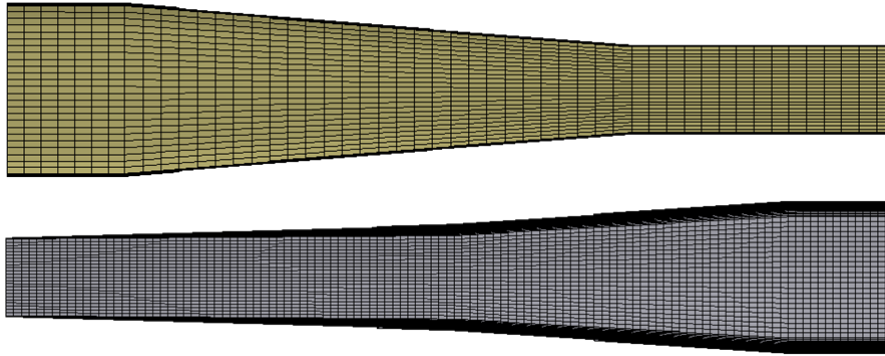**Figure 3.11:** Mesh in the upstream and downstream end, created with the *Sweep* and *MultiZone* method. This is the mesh referred to as the fine mesh in the mesh independence study later on in the report.

surfaces can be found and that any sizing control is not in conflict with the sweeping. If a body is sweepable, it can be meshed very efficiently with hexahedral and wedge elements. Both the upstream and downstream end was attempted meshed with *Sweep*, but the mesher failed when *Sweep* was applied to the downstream end. This was probably due to some of the sizing controls in the domain, and the *MultiZone* method was tried for this part instead. The *MultiZone* method automatically generates a pure hexahedral mesh where possible and then fills the rest with unstructured mesh. With the *MultiZone* method in the downstream end, the mesh was successfully generated. The two discussed mesh sections are presented in Fig. 3.11.

The upstream and downstream parts of the mesh are not regarded as of great importance for the case at hand, as opposed to the test section containing the hydrofoil. Therefore, the mesh is coarser and the elements are elongated in the flow direction. The latter characteristic is a measure to decrease the number of nodes without compromising on the ability to solve the flow adequately. This follows from the assumption that the velocity gradient in the cross flow direction is much greater than the gradient in the streamwise direction, and hence it is more important to have a fine mesh in the cross flow direction than in the streamwise.

3.3.1 Inflation layer thickness and growth rate test

After assessing the results from the 2D simulations in the project work, some doubt arose whether the inflation layers were thick enough to cover the boundary layer development. Hence, it was suggested for further work to investigate if the inflation layers limit the development of the boundary layer. In this master thesis, it was therefore of interest to conduct a small study of this, before designing the meshes.

The test was performed in 2D on a mesh corresponding to the 3D coarse mesh, as will be introduced in the mesh independence study in Section 3.5.1. Specifically, the 2D coarse mesh from the project work was used in this case. The objective was to check whether the simulation results changed if the inflation layers were expanded in the direction normal to the surface, i.e. if their thickness were increased, and to do so very efficiently with respect to time and computational power.

Originally, the inflation layers in the project work had an inflation layer total thickness of 1.4 mm, and a growth rate of 1.2. To investigate the effects of a change in this thickness, the time-averaged streamwise velocity profile at $z = 9.9D$ downstream of the trailing edge was sampled after iterative convergence was reached. First, the growth rate was changed from 1.2 to 1.1 to make the mesh suitable for the $\gamma - Re_\theta$ transition model. Then, the thickness was doubled to 2.8 mm, and the velocity profile was sampled.

The three velocity profiles are presented in Fig. 3.12 (growth rate is denoted as GR). As can be observed, there is undoubtedly a change in the velocity profile as the inflation layers are refined and thickened. When compared to experimental results in the project work, the original case of thickness 1.4 mm and growth rate 1.2 showed an underprediction of the velocity deficit. In this test, the underprediction relatively to the experimental results was reduced as the thickness and growth rate was altered. The change in the thickness showed the strongest effect in the velocity profile. This strongly suggests that the boundary layer development is limited by the inflation layers if they have a thickness of 1.4 mm.

Ideally, the inflation layer thickness would be increased until one could no longer find a change in the velocity profile. However, the meshing of very thick boundary layers can often be challenging for the mesher, and in combination with the restrictions of time, this was not prioritized. It was decided to use inflation layer settings
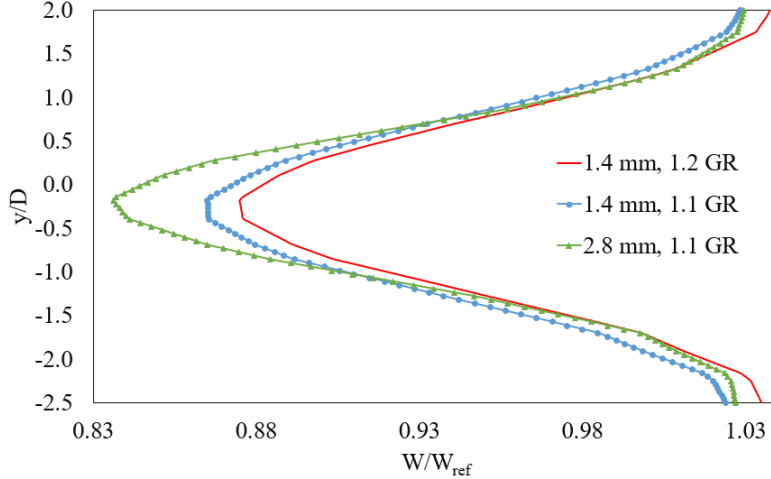
24

Figure 3.12: Inflation layer thickness and growth rate test.

corresponding to the 2.8 mm thickness and the 1.1 growth rate for the rest of the meshes in this master thesis.

3.4 Iterative convergence

Before performing a mesh independence study, the iterative convergence was checked. Three meshes were created for the mesh independence study, referred to as the coarse, medium and fine mesh. Details on these will be presented in Section 3.5.1. The iterative convergence was checked by assessing whether the residuals achieved convergence according to the residual target of 1e-04, and assessing the convergence of some important parameters. These parameters were velocities at several points in the domain, but most importantly the velocity V at the positions $z = 25$ mm, $z = 55$ mm and $z = 85$ mm downstream of the trailing edge. Oscillations of the velocity V in these positions are a good indication of vortex shedding.

Ideally, one should wait until the simulated time has reached the time it will take for the flow to move from inlet to outlet and back again, before concluding with iterative convergence and starting the sampling. This is to ensure that possible effects appearing in the flow as it passes through the flow domain will have the time it takes to develop and propagate from one end of the flow to the other. This requires much more computational power and time than to just wait for the residuals and some key parameters to find apparent convergence at a much earlier point in time. Due to the limited resources and little suspicion of change to happen after a very long simulated time, this was not prioritized in the simulations of this master thesis.

There was observed an agreement between the plots of the residuals and the important parameters regarding which timestep the solution settled with repetitive and, what appeared to be, identical oscillations. This was seemingly after timestep 500 for the three meshes, with some variation. The residuals were all within the residual target. To be conservative, it was decided to wait until timestep 1000 before doing any samplings for all simulations.

Additionally, the iteration errors were assessed for the three meshes. This was done by checking what difference exists in the time-averaged streamwise velocity profile when retrieved with a number of iterations in-between. Specifically, the time average was first sampled over roughly 75 shedding periods after iterative convergence was considered achieved, and then over 50 more. By comparing the two time-averaged velocity profiles from this procedure, i.e. time average after 75 periods and after 125 periods, one should not find much difference if the iteration error is small. This assessment was performed on all three meshes with the SST $k - \omega$ model, and also with the the $\gamma - Re_\theta$ transition model on the fine mesh.

The results from the iteration error check on the fine mesh, both with and without the $\gamma - Re_\theta$ transition model, are plotted in Fig. 3.13. The velocities are normalized with respect to the reference velocity $W_{ref} = 9.6$ m/s, and the height is normalized by the trailing edge thickness, with $y = 0$ being at the hydrofoil centerline. As can be observed in Fig. 3.13, there seems to be little difference between the velocity profiles sampled over 75 and 125 shedding periods for each case. This implies that the iteration error is very small. This was the case for the coarse and the medium mesh as well, even though they are not included in the plot.
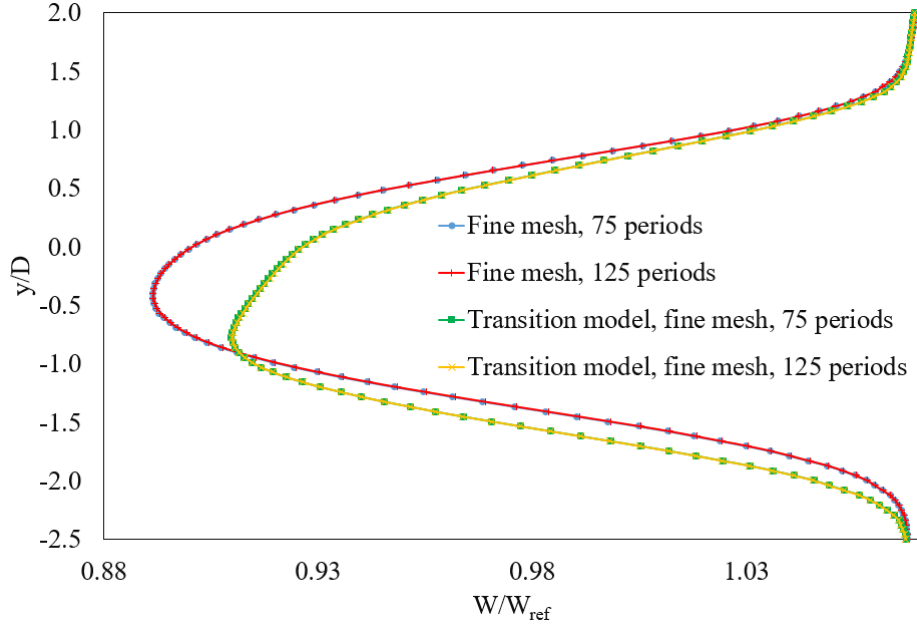
Figure 3.13: Time-averaged streamwise velocity profiles at position $z = 9.9D$ downstream of the trailing edge, along the hydrofoil centerline. Simulation performed on the fine mesh with the SST $k - \omega$ model alone and in combination with the transition model to check the error related to iteration convergence.

3.5   Mesh independence study

To estimate the discretization error, a mesh independence study was performed according to the guidelines in the article "Procedure for Estimation and Reporting of Uncertainty Due to Discretization in CFD Applications" by Celik et al. [6]. In this section, the application of the procedure to the case at hand is described, including the findings resulting from it.

3.5.1   Three meshes

As described in the article by Celik et al. [6], three significantly different meshes are to be selected, and simulations are to be run on each of them. Two new meshes needed to be created for this. Based on the mesh that already was created, referred to as the fine mesh from here on in the mesh independence study, a medium mesh and a coarse mesh were developed. This was done by adjusting the cell sizing specifications so that they differ from each other by a grid refinement factor of 1.5, i.e. so that a given cell in the coarse mesh is 1.5 times larger than the corresponding cell in the medium mesh, and a cell in the medium mesh is 1.5 times larger than the corresponding cell in the fine mesh. The resulting numbers of nodes from this procedure are presented in Table 3.3. The settings for the inflation layers were kept constant during this process, and is hence identical for the three meshes. Ideally, these would be changed with the refinement factor as well, but this is very difficult to implement practically in the mesh. The meshes will be referred to as 1, 2 and 3 for the fine, medium and coarse mesh, respectively.

When designing the meshes for the mesh independence study, there are several factors that must be taken into consideration. According to Celik et al. [6], experience has shown that it is desirable that the grid refinement factor r is greater than 1.3. Simultaneously, there are other practical restrictions to the meshes; in one end, the coarsest mesh cannot be too coarse without losing the ability to simulate the vortex shedding phenomenon, and in the other end, the finest mesh cannot be too fine without running out of computational power and time. For this mesh independence study, the restrictions were successfully balanced and met, and a grid refinement factor above the recommended minimum value for the meshes was obtained; $r = 1.5$.

Table 3.3: Three meshes of different resolution for the mesh independence study.

Mesh	Number of nodes
1. Fine	37 720 629
2. Medium	16 349 920
3. Coarse	7 787 930

Table 3.4: Simulation and calculation results from the procedure by Celik et al. [6], applied to the velocity profiles and the vortex shedding frequencies.

Calculations for discretization error estimation		
	Shedding frequency	Velocity profile (spatially averaged values)
N_1	37 720 629	37 720 629
N_2	16 349 920	16 349 920
N_3	7 787 930	7 787 930
r_{21}	1.5	1.5
r_{32}	1.5	1.5
ϕ_1	474.76 Hz	9.48 m/s
ϕ_2	469.53 Hz	9.44 m/s
ϕ_3	449.55 Hz	9.39 m/s
p_m	3.31	3.18
ϕ_{ext}^{21}	476.61 Hz	9.49 m/s
e_a^{21}	1.102 %	0.468 %
e_{ext}^{21}	0.389 %	0.178 %
GCI_{fine}^{21}	0.488 %	0.223 %

3.5.2 Discretization error estimation

To estimate the discretization error, the values of variables that are considered critical to the conclusion of the simulation study should be analyzed for the three meshes. This will be the vortex shedding frequency and the velocity profile in the wake for the case at hand.

The vortex shedding frequency was obtained by doing a fast Fourier transform of the velocity V in the wake for simulations on all three meshes. The velocity data was sampled over time intervals corresponding to approximately 100 shedding periods, after iterative convergence was reached. In the procedure by Celik et al. [6], the three shedding frequencies from the fine, medium and coarse mesh each represent a simulation result variable: ϕ_1, ϕ_2 and ϕ_3. They are listed in Table 3.4.

The velocity profiles were obtained by time-averaging the streamwise velocity W at the position $z = 9.9D$ downstream of the trailing edge in simulations performed on all three meshes. The averaging was performed over an interval of approximately 100 shedding periods for the fine mesh and 50 shedding periods for the medium and coarse mesh, after iterative convergence was considered achieved. The coarse and medium mesh velocity profiles were only sampled over 50 shedding periods as a measure to reduce the computational cost related to the mesh independence study - the iterative convergence suggests that there should be little difference between the result after 50 and 100 shedding periods. The sampling produced a vector of velocity W values for each simulation, filling the purpose of the variable ϕ in the procedure by Celik et al. [6]. The spatially averaged values of these three vectors are also listed in Table 3.4.

The calculation results from the procedure by Celik et al. [6] are presented in Table 3.4, where the ones related to the velocity profiles are spatially averaged. The meshes are referred to in subscript as 1, 2 and 3 for the fine, medium and coarse mesh, respectively. In the table, N denotes the number of nodes in the mesh, r is
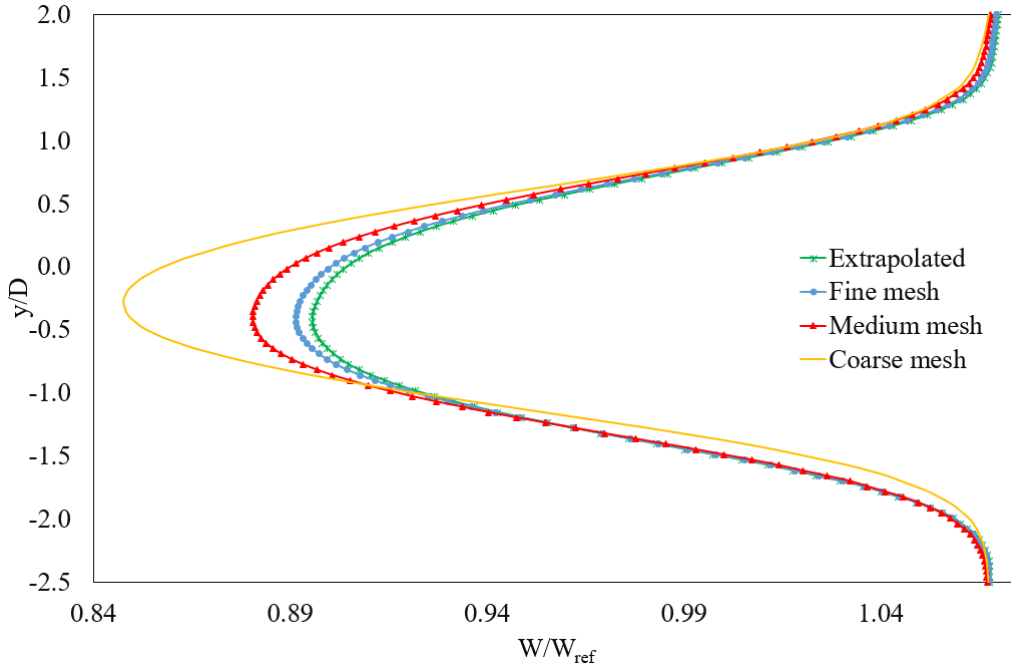
Figure 3.14: Time-averaged streamwise velocity profiles at $z = 9.9D$ downstream of the trailing edge, from simulations on the three different meshes and from extrapolation.

the refinement factor, ϕ is the simulation result and p_m is the apparent order of the method. Further, ϕ_{ext} is the extrapolated value, e_a is the approximate relative error, e_{ext} is the extrapolated relative error and GCI is the grid convergence index.

The apparent order p_m of the method was calculated using the expressions in the article by Celik et al. [6]. Based on the shedding frequency results, the apparent order of accuracy was 3.31, and based on the velocity profile results, the local order of accuracy ranges from 0.048 to 11 with a global average $p_{m,ave}$ of 3.18. ANSYS CFX uses second order accurate discretization approximations as much as possible, which means that the estimated values for p_m in this study is a bit higher than the formal one is. One can however argue that they are still within a reasonable range. The apparent order p_m is a very sensitive variable, and factors such as round-off errors and iterative convergence are possible causes for the difference between p_m and the formal order of the method. Additionally, both the shedding frequency and the velocity profile are highly dependent on the location of the separation point on the foil surface. Having the inflation layer settings constant for all the tree meshes means that the mesh is not refined in the direction normal to the foil surface at the most critical area for the separation point. This is likely to be an important contributor to the difference in the apparent order of the method and the formal one as well.

The global average of the apparent order $p_{m,ave}$ is used to calculate the extrapolated velocity profile ϕ_{ext}^{21} and the grid convergence index (GCI) values for the fine mesh. The extrapolated velocity profile is plotted together with the three simulated velocity profiles from the coarse, medium and fine mesh in Fig. 3.14. The velocities are normalized with respect to the reference velocity $W_{ref} = 9.6$ m/s. The height is normalized by the trailing edge thickness D, with $y = 0$ set at the hydrofoil centerline. As can be observed in Fig. 3.14, the medium mesh simulation differs unquestionably more from the coarse mesh solution than from the fine mesh solution. This might indicate that the results are converging.

In the procedure, the variables ϵ_{32} and ϵ_{21} are defined as $\epsilon_{32} = \phi_3 - \phi_2$ and $\epsilon_{21} = \phi_2 - \phi_1$, and negative values of $\epsilon_{32}/\epsilon_{21}$ are hence an indication of oscillatory convergence. According to this, oscillatory convergence is indicated at 26.9 % of the 108 points from the velocity profiles. The GCI values are plotted as error bars on the velocity profile from the fine mesh simulation in Fig. 3.15, which is the mesh that will be used for the main part of the results in this report. The solutions from the three meshes differ the most from each other where the velocity deficit is the largest, as observed in Fig. 3.14. This is captured well by the error bars in Fig. 3.15, which indicate that the discretization uncertainty is highest where the velocity deficit is the largest. The maximum discretization uncertainty is 0.59 %, which corresponds to ± 0.05 m/s.
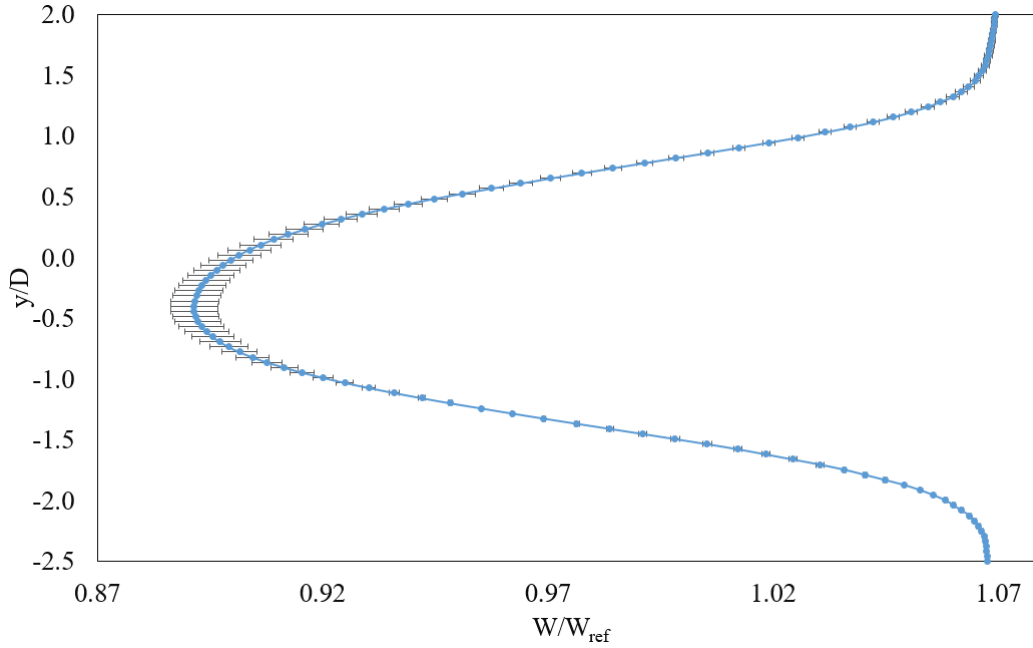
28

Figure 3.15: Time-averaged streamwise velocity profile at $z = 9.9D$ downstream of the trailing edge from fine mesh simulation, plotted with uncertainty error bars.

Figure 3.16: Location of the sampling lines (in yellow) for the velocity profiles in the inlet location dependence study. The locations are $z = 0.630$ m, $z = 1.381$ m, $z = 1.943$ m and $z = 1.99952$ m ($9.9D$ m downstream of trailing edge) downstream of the original inlet location along the centerline.

In the article by Celik et al. [6] it is also stated that uncertainty in inlet flow boundary conditions can be a significant contributor to the overall uncertainty. Therefore, it is recommended that the degree of sensitivity of the presented solution to small perturbations in the inlet conditions is studied and reported. In the following sections, the solution's dependence on the location of the inlet boundary and on the inlet turbulence parameters settings is investigated. Details of the approach are presented in Section 3.6 and 3.7, and the findings are presented in Chapter 4.

3.6   Study of dependence on location of inlet boundary

An investigation of the inlet boundary's location has been performed, and it will in this context be referred to as the inlet location dependence study. The objective is to check whether the simulation results change notably if the inlet boundary is moved upstream, i.e. if the pipe upstream of the test section is extended. In this study, the simulation results after extending the pipe with 1 m, 3 m and 7 m was compared to the original case of 0 m extension. The time-averaged streamwise velocity profiles at four locations along the centerline in the flow domain was used for comparison of the simulation results. The location of the sampling lines for this are presented in Fig. 3.16. The time-averaging of the velocity profiles was done over a time interval corresponding to approximately 25 vortex shedding periods, after iterative convergence was considered reached. The simulations were conducted with the SST $k - \omega$ model.

Due to the limited resources at hand, i.e. computational power and time, it was decided to use the coarse mesh settings to make this particular study more economical. Details on this mesh can be found in Section 3.5. For each time the geometry is changed, i.e. the pipe is extended in this case, the mesh must be regenerated. This opens up for possible differences appearing in the mesh for the different pipe lengths. Fig. 3.17 illustrates the mesh at the inlet boundary for the four geometries used in the inlet location dependence study. The upstream

contracter, which has the inlet boundary as one of its ends, is a particularly tricky geometry to mesh, changing gradually from a circular inlet to a rectangular outlet along its length as shown in Fig. 3.18. Hence, despite identical mesh settings, the meshing program performed differently for the four cases. It appears that the quality of the inflation layers varies a great deal, with the 3 meters mesh in Fig. 3.17c being the most extreme case. Attempts were made to reduce the differences between the meshes without great success. The differences are not regarded as critical to the study, but should however be taken into consideration when analyzing the results, which are presented in Chapter 4.

(a) 0 meter (original).

(b) 1 meter.

(c) 3 meters.

(d) 7 meters.
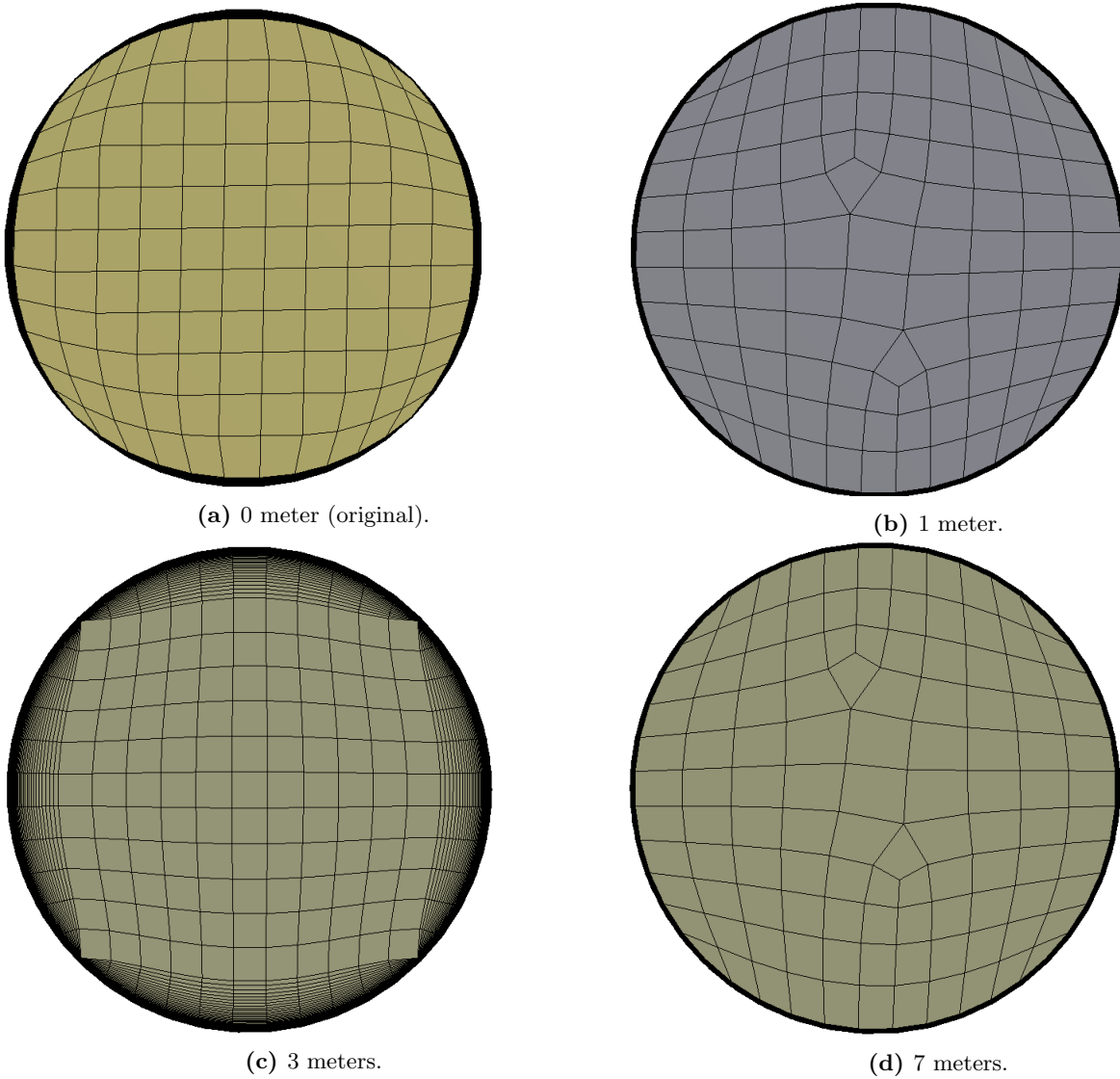
Figure 3.17: Coarse mesh at the inlet boundary for the four different geometries used in the inlet location dependence study.

It can also be emphasized that this is the coarse mesh, which originally was designed to simulate the flow around the hydrofoil in the test section as economically as possible. In this master thesis, the objective is to determine the flow characteristics behind the trailing edge of the hydrofoil, which have led to a prioritization of the mesh quality in the rectangular test section. Poorer quality can be allowed in less critical parts of the mesh, like the upstream contracter in this case, in order to obtain a high quality in more important parts to a reasonable prize. More computational power and time would have allowed for a better mesh quality in the upstream contracter.

Figure 3.18: Upstream contracter (and the first 0.445 m of the rectangular pipe section) with the coarse mesh.

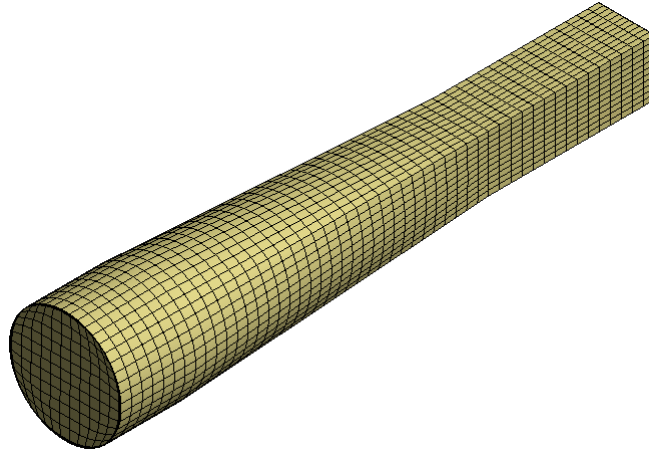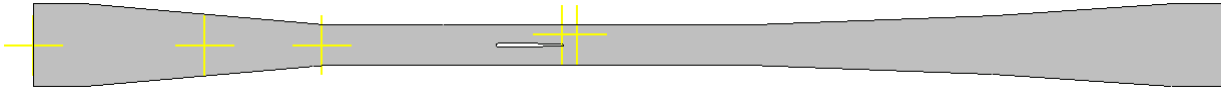**Figure 3.19:** Location for the sampling points used in the turbulence parameters dependence study: $z = 0$ m (inlet), $z = 0.63$ m, $z = 1.06$ m, $z = 1.943$ m, and $z = 1.99952$ m ($9.9D$ downstream of the trailing edge).

3.7   Study of dependence on turbulence parameters

It is of interest to check how sensitive the simulation results are to the turbulence levels specification in the boundary and initial conditions. To do this, a turbulence parameters dependence study has been conducted, where three different inlet turbulence intensities has been tested: $I = 1\%$, $I = 5\%$ and $I = 10\%$. The turbulence length scale was specified and held constant throughout the test with a value of 0.025 m, as calculated in Section 2.3.3. The simulations were conducted with the SST $k - \omega$ model.

To assess the effects of the different turbulence intensities, the time average of the turbulence kinetic energy k and of the turbulence eddy dissipation ϵ was measured at five points along the centerline in the domain. These points are illustrated in Fig. 3.19. Details on the relation between k, ϵ and the turbulence intensity can be found in Section 2.3.3. Additionally, the time-averaged streamwise velocity profiles at three sampling lines along the centerline in the domain were checked for the different turbulence level settings. The location of the sampling lines are illustrated in Fig. 3.20. The sampling of both k, ϵ and the velocity profiles were done over a time interval corresponding to approximately 25 vortex shedding periods, after iterative convergence was reached.

The turbulence parameters dependence study was conducted in a 2D version of the case to save computational power and time. The mesh settings correspond to the settings for the fine mesh in 3D, and the results from the study in 2D is expected to have validity for the simulations in 3D as well. The results from the turbulence parameters dependence study are presented in Chapter 4.
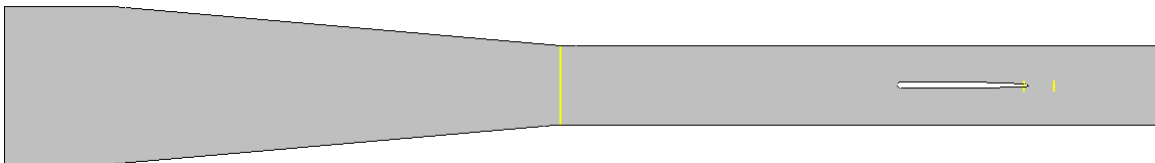

Figure 3.20: Location for the sampling lines used in the turbulence parameters dependence study: $z = 1.06$ m, $z = 1.943$ m, and $z = 1.99952$ m (corresponding to $9.9D$ downstream of the trailing edge) downstream of the inlet.

Chapter 4

Results and Discussion

In this chapter, the results from the location of inlet boundary dependence study, the turbulence parameters dependence study and the main simulations with SST $k - \omega$ turbulence model with and without the $\gamma - Re_\theta$ transition model, will be presented and discussed.

4.1 Study of dependence on location of inlet boundary

The results from the inlet location dependence study are presented in Fig. 4.1, Fig. 4.2, Fig. 4.3 and Fig. 4.4. They consist of time-averaged streamwise velocity profiles from different positions in the flow domain, as described in Section 3.6, for four different lengths of the pipe in the upstream end. The original case is denoted *0 meter*, and is identical to the geometry presented in Section 3.1. The names of the three other cases, *1 meter*, *3 meter* and *7 meter*, refer to the respective lengths of the extension of the pipe in the upstream direction. The time-averaging was done over an interval corresponding to approximately 25 shedding periods, after iterative convergence was considered reached. For the determination of the flow field characteristics behind the trailing edge, which is the objective of this master thesis, it is the velocity profiles in vicinity of the trailing edge, i.e. the velocity profile right upstream of the trailing edge and at $z = 9.9D$ downstream of the trailing edge, that is of greatest interest.

The velocity profiles show that the extension of the pipe upstream of the inlet boundary has an effect on the flow further downstream. In Fig. 4.1 one can observe that the longer the extension, the more developed is the velocity profile at the first sampling line. Yet, further downstream at the second sampling line, the effect of this is reduced, and right upstream of the trailing edge one can barely see a difference anymore. Then, for the last sampling line at $z = 9.9D$ behind the trailing edge, the differences appear increased again.

In all four figures, the 7 meter trendline shows a higher velocity in the middle of the pipe. This is a reasonable result, seeing that with a longer pipe upstream of the sampling lines, the pipe flow will be closer to fully developed than with a shorter pipe. This effect can be observed for the rest of the pipe extensions as well, where the velocity in the middle of the pipe depends on the pipe length. The closer the pipe flow is to being fully developed, the higher velocity can be expected in the middle of the pipe.

For the three first sampling lines, there is a regular trend which can be traced back to the length of the extensions and the development of the pipe flow, accordingly. At the fourth sampling line, however, some irregularity with respect to the extension lengths is present in the velocity deficits. There, the freestream velocity corresponds well to the trend with higher velocity for a longer extension, with the 7 meters case having the highest and the 0 meter case having the lowest freestream velocity. Apart from this, one can observe that the 7 meters case has a smaller velocity deficit than the 3 meters case, and that the 0 meter case has a smaller velocity deficit than the 1 meter case, which is in poor correspondence to the extension lengths. It is possible that this irregularity is related to poor and varying mesh quality, as mentioned in Section 3.6. Nonetheless, it is obvious from the figures that the velocity profiles are affected by the extension of the pipe upstream of the inlet boundary.
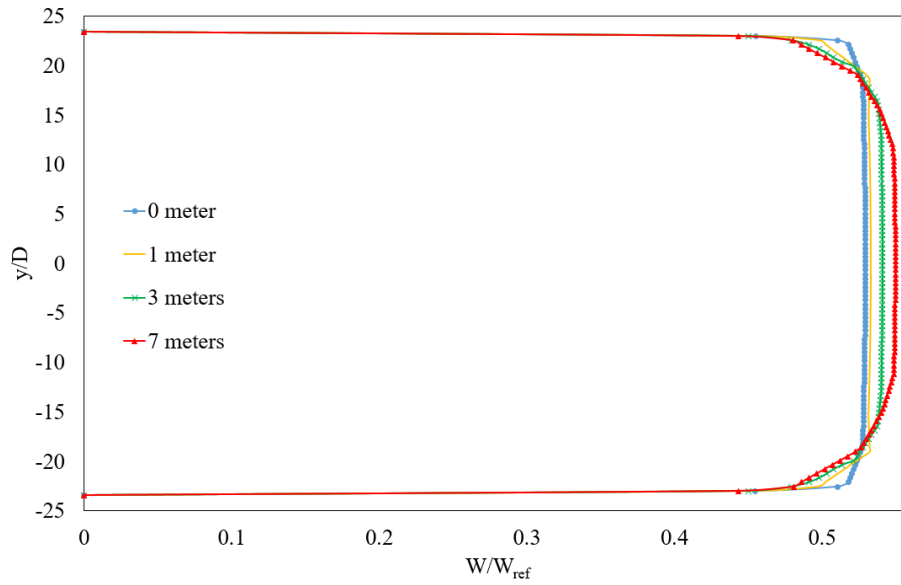
Figure 4.1: Time-averaged streamwise velocity profile at first sampling line, located in the middle of the upstream contracter.

Figure 4.2: Time-averaged streamwise velocity profile at second sampling line, located upstream of the foil in the rectangular section.
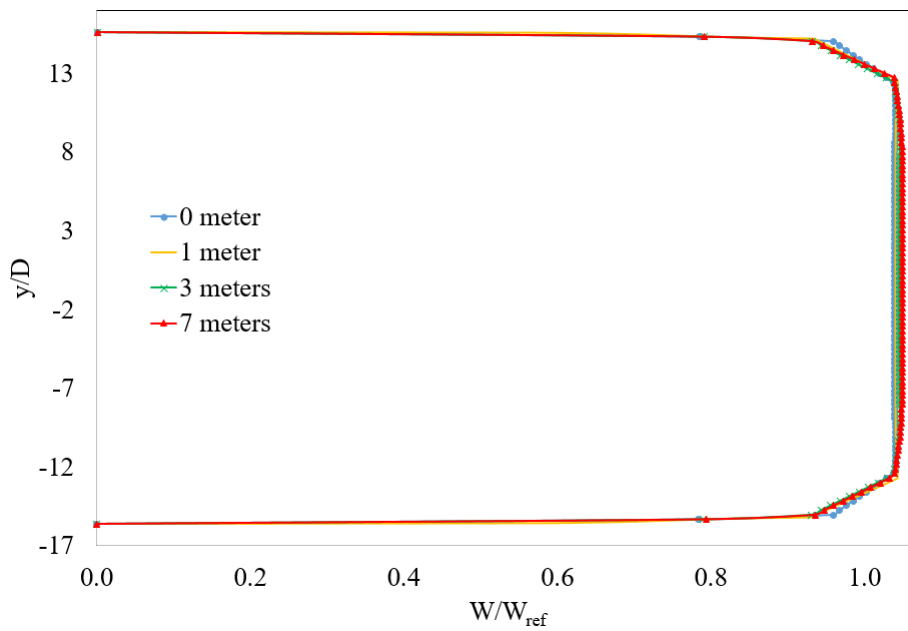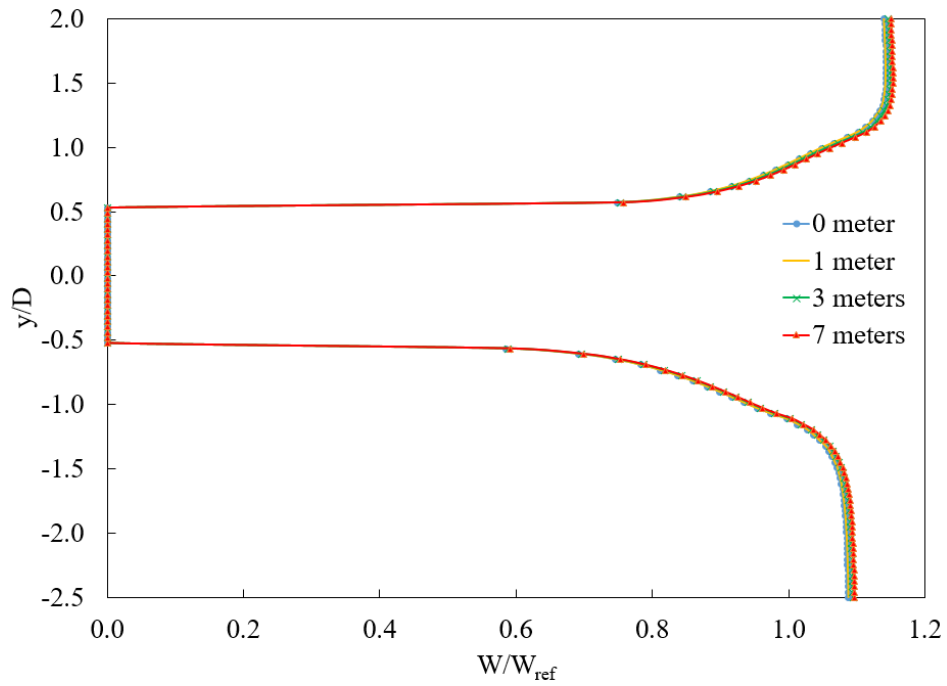
Figure 4.3: Time-averaged streamwise velocity profile at third sampling line, located right upstream of the trailing edge.
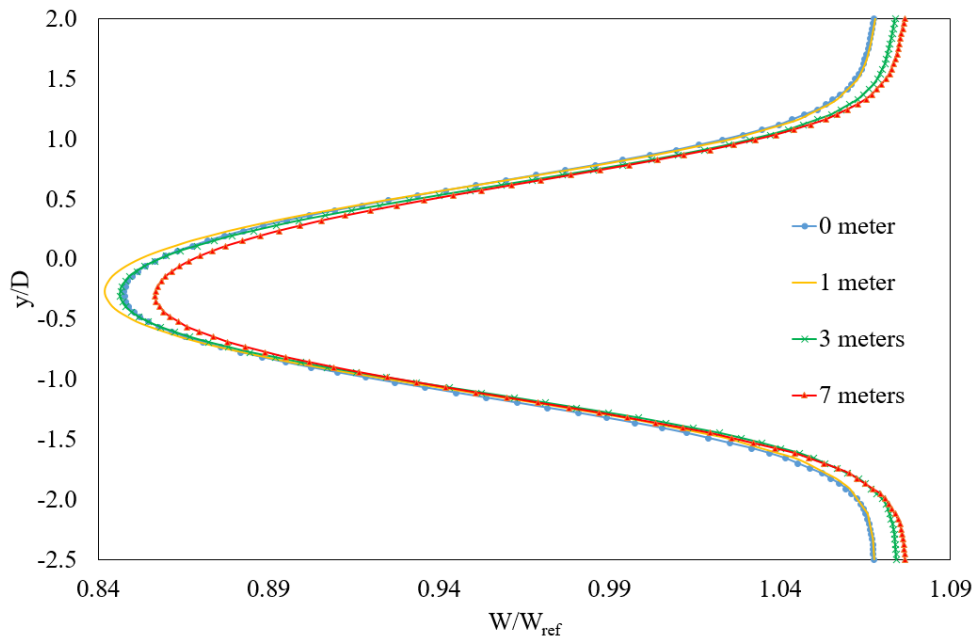

Figure 4.4: Time-averaged streamwise velocity profile at fourth sampling line, located at $z = 9.9D$ downstream of the trailing edge.
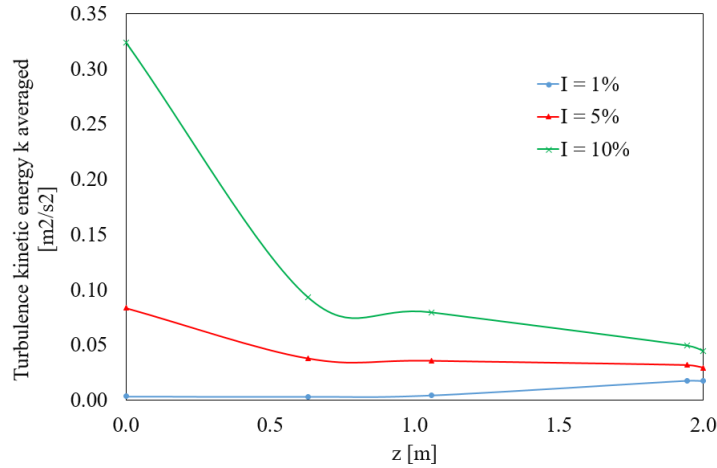
Figure 4.5: Time-averaged turbulence kinetic energy k sampled at five points for three different inlet turbulence intensities.
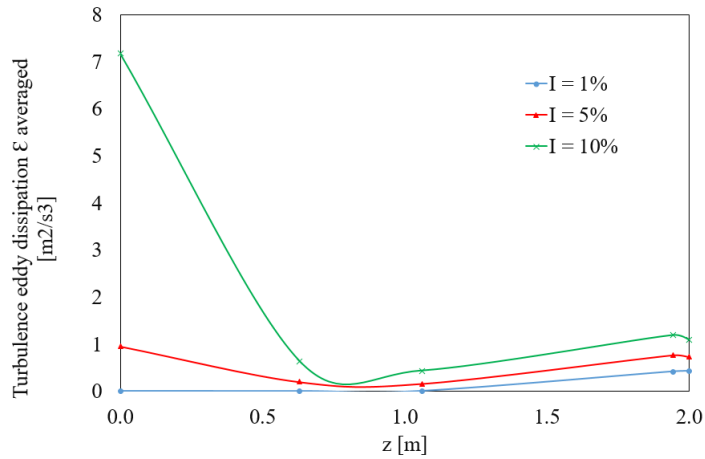

Figure 4.6: Time-averaged turbulence eddy dissipation ϵ sampled at five points for three different turbulence intensities.

4.2   Study of dependence on turbulence parameters

The results from the turbulence parameters dependence study are presented in Fig. 4.5, Fig. 4.6, Fig. 4.7, Fig. 4.8 and Fig. 4.9. Fig. 4.5 and Fig. 4.6 show the time-averaged turbulence kinetic energy k and turbulence eddy dissipation ϵ at five points in the flow domain, as described in Section 3.7. They are plotted against the distance z from the inlet, and for three different turbulence intensities as inlet condition. The time-averaging was done over an interval corresponding to approximately 25 shedding periods, after iterative convergence was considered reached. The simulations were conducted with the SST $k - \omega$ model.

Two-equation turbulence models like the SST $k - \omega$ model can estimate very large and nonphysical decay rates of turbulence quantities when commonly used inflow values are specified. This topic is treated in the paper "Effective Inflow Conditions for Turbulence Models in Aerodynamic Calculations" by Spalart and Rumsey [37]. They show, starting from the model equations, how the chosen freestream values, i.e. the inflow values, of turbulence quantities have a strong influence on the turbulence decay rate in the flow domain. According to the paper, the higher the freestream turbulence intensity I, the more rapid the decay. This is in good agreement with the trends in Fig. 4.5 and Fig. 4.6. It is clear from those figures that the case with the highest inlet turbulence intensity $I = 10$ % has the steepest turbulence decay.

By the relation between the turbulence kinetic energy k, velocity W and turbulence intensity I

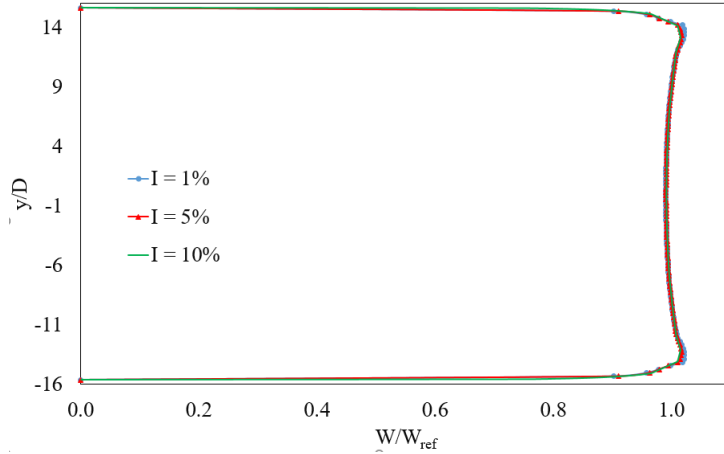$$k = \frac{3}{2}(WI)^2 \tag{4.1}$$

35

Figure 4.7: Time-averaged streamwise velocity profile at first sampling line, located at $z = 1.06$ m, for three different inlet turbulence intensities.
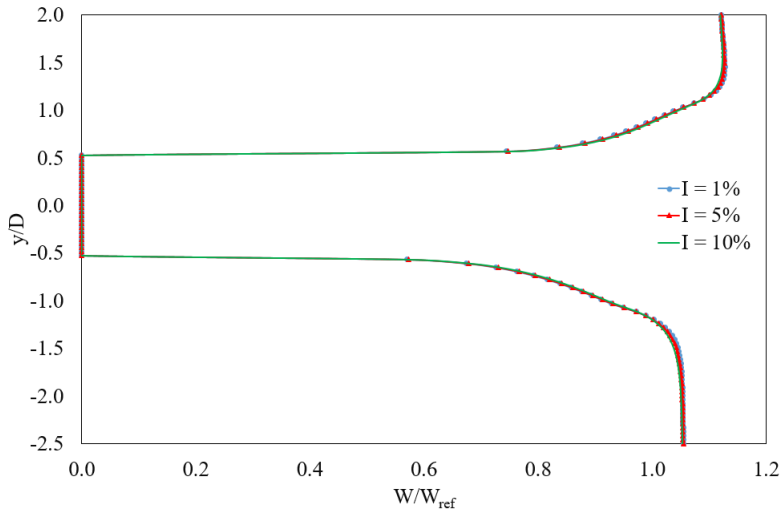

Figure 4.8: Time-averaged streamwise velocity profile at second sampling line, located right upstream of the trailing edge at $z = 1.943$ m, for three different inlet turbulence intensities.

one can identify a decay for the two other cases as well. Taking into consideration that W is increasing with z due to the decrease in the cross-sectional area from inlet to the test section, k should increase as well. This applies especially from $z = 0$ m to $z = 1.06$ m, where the flow moves through the contracter. The fact that k does not increase is an indication of a decrease in I. The net change in k is small for the cases with $I = 1$ % and $I = 5$ % as inflow conditions, so there must be a decrease in I that counteracts on the increase in W. This effect seems to be more dominant the higher the inlet turbulence intensity is, as shown by Spalart and Rumsey [37].

This varying degree of decay leads to a converging trend in both Fig. 4.5 and Fig. 4.6 as we move downstream from the inlet ($z = 0$). Despite a large difference at the inlet, both k and ϵ changes so that it is reduced. Further downstream, both parameters end up at a turbulence level that seems to have relatively little dependence on the inlet condition. More specifically, within 1 m from the inlet the different turbulence levels is evened out to be quite similar. This happens upstream of the test section, and is maintained as the flow passes the foil, according to the two figures.

Fig. 4.7, Fig. 4.8 and Fig. 4.9 show what effect the different inflow turbulence intensities has on the time-averaged streamwise velocity profiles. They are sampled at three different positions over a time interval corresponding to approximately 25 shedding periods, as described in Section 3.7. One can observe little difference in these plots based on the difference in turbulence intensity at the inlet. The largest difference seems to be at $z = 9.9D$ downstream of the trailing edge, where the trendline for 10 % inflow turbulence intensity has a larger
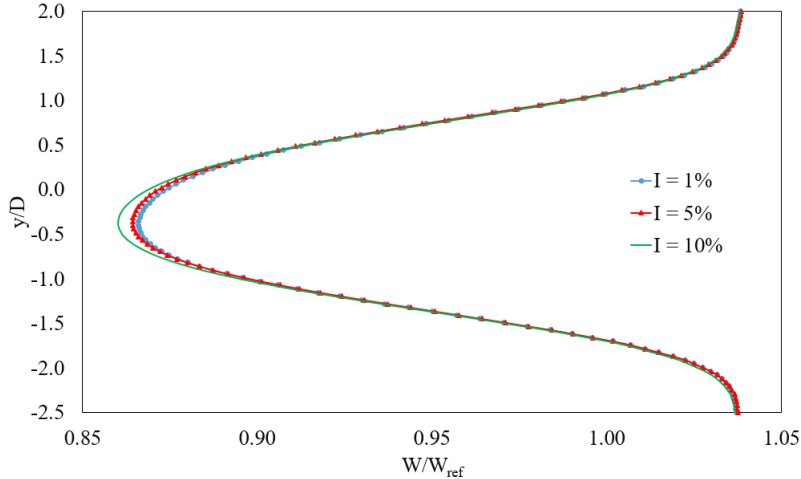
36

Figure 4.9: Time-averaged streamwise velocity profile at third sampling line, located $9.9D$ downstream of the trailing edge at $z = 1.99952$ m, for three different inlet turbulence intensities.

velocity deficit than the others. Nevertheless, this study suggests that due to the turbulence decay, there is a modest dependence on the turbulence quantities specified at the inlet for the flow in the test section, when the simulations are conducted with the SST $k - \omega$ model.

4.3 Simulation results

In this section, the amplitude frequency spectra for the vortex shedding, as well as the time-averaged streamwise velocity profiles at two positions in the wake, will be presented. Additionally, some other details from the simulation results, like the turbulence kinetic energy and separation bubbles, will be included.

Two types of simulations have been conducted: one with the SST $k - \omega$ turbulence model and one with the same turbulence model in combination with the $\gamma - Re_\theta$ transition model. The simulation results of this master thesis will be compared with experimental data obtained by Sagmo et al. [33], in addition to some of the numerical results presented in the same paper.

The instantaneous velocity fields for the two types of simulations are presented in Fig. 4.10 and Fig. 4.11. As can be observed, the differences are small. However, by studying the details of the von Karman vortex streets closely, it is possible to distinguish them from one another. In Fig. 4.11, a slight tendency of the wake breaking down into smaller vortices can be observed, and it seems to happen especially in the lower half of the wake. This behaviour is not as easily observed in the velocity field from the simulation with the SST $k - \omega$ model alone in Fig. 4.10. Apart from this, the simulations perform very similarly, judging by the instantaneous velocity fields.

It was observed during the course of this study that the computational costs are significantly higher for the simulation conducted with the $\gamma - Re_\theta$ transition model than for fully turbulent calculations. This is a consequence of solving two additional transport equations, and that the interaction between the momentum, turbulence and transition equations requires more iterations to obtain satisfactory convergence [24]. Another factor is that for the turbulent numerics in the solver, the *High resolution* option should be used with the transition model, which demands more in regards of computational power than the *First order* option that is considered sufficient with the SST $k - \omega$ model alone. Also, the same mesh was used for the simulations with and without the transition model in this case, but in general, the transition model have stricter requirements than the SST $k - \omega$ model to the mesh resolution, regarding both the wall-normal and streamwise spacing [24].

The motivation for using the $\gamma - Re_\theta$ transition model is its capability of resolving the boundary layer more realistically. One of the effects from applying the model to the case at hand is the appearance of transitional separation bubbles on the upper and lower surfaces near the leading edge of the hydrofoil. An illustration of the separation bubble on the upper surface is presented in Fig. 4.12. By consulting the contour plot of the turbulence kinetic energy in the same area in Fig. 4.13, the transition from laminar to turbulent boundary layer can easily be identified. This is a good demonstration of the workings of the transition model.
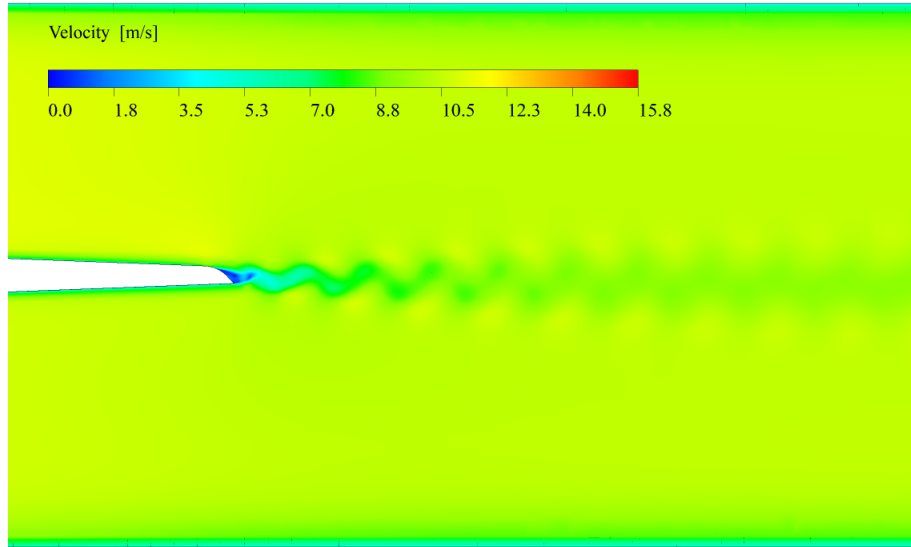
Figure 4.10: Instantaneous velocity field in trailing edge wake from numerical simulation with the SST $k - \omega$ model.
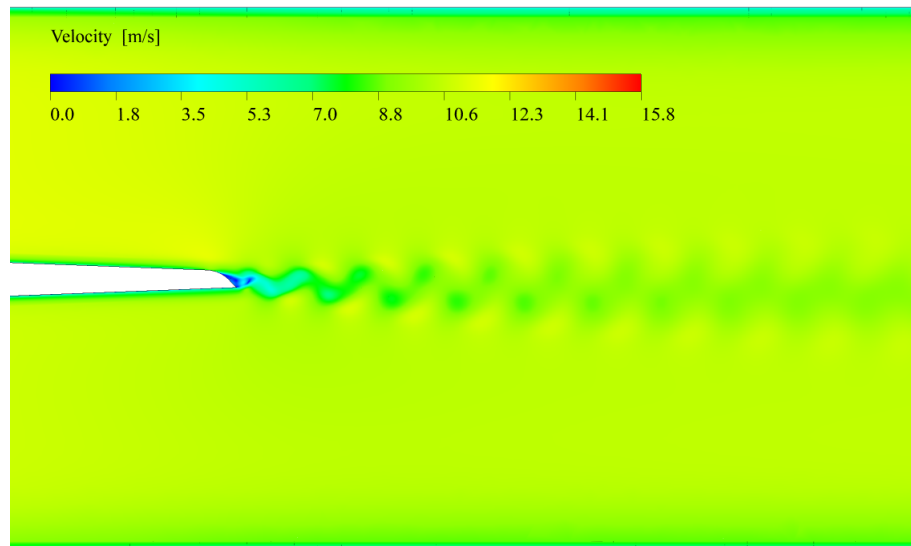
Figure 4.11: Instantaneous velocity field in trailing edge wake from numerical simulation with the SST $k - \omega$ model in combination with the $\gamma - Re_\theta$ transition model.

For comparison, Fig. 4.14 shows the boundary layer near the leading edge for the simulation with only the SST $k - \omega$ model active, where no separation bubble appears. In that case, no transition from laminar to turbulent boundary layer is simulated either; the boundary layer is simulated as turbulent everywhere. This is visualized by the turbulence kinetic energy in Fig. 4.15. The effects of the different boundary layer predictions will be investigated further on in the report, by looking at the estimated shedding frequency and the time-averaged streamwise velocity profiles in the wake for the simulations with and without the transition model.

Figure 4.12: Separation bubble on the upper surface near the leading edge of the hydrofoil, present in the numerical simulation with the SST $k - \omega$ model in combination with the $\gamma - Re_\theta$ transition model.

Figure 4.13: Turbulence kinetic energy on the upper surface near the leading edge of the hydrofoil, from the numerical simulation with the SST $k - \omega$ model in combination with the $\gamma - Re_\theta$ transition model.
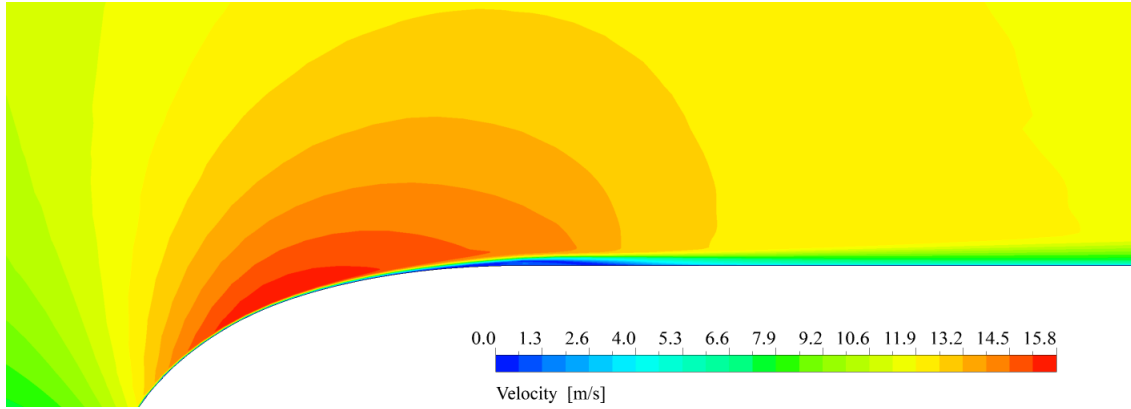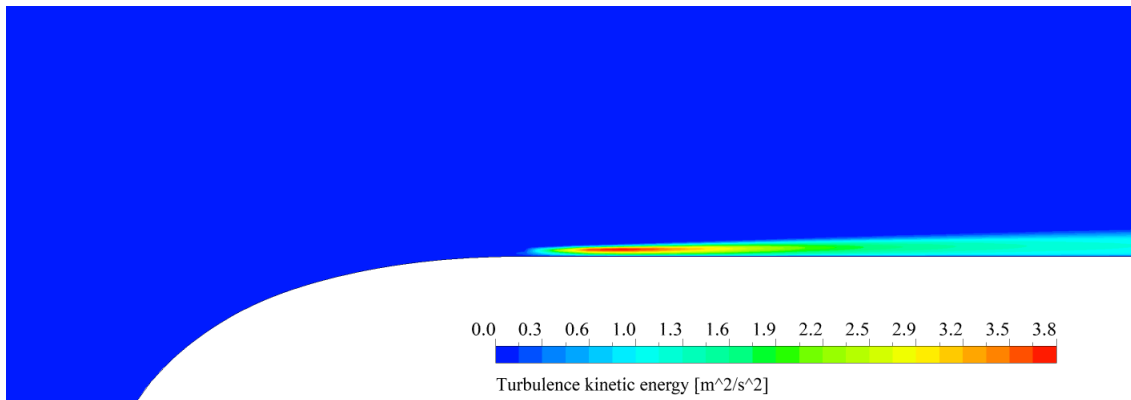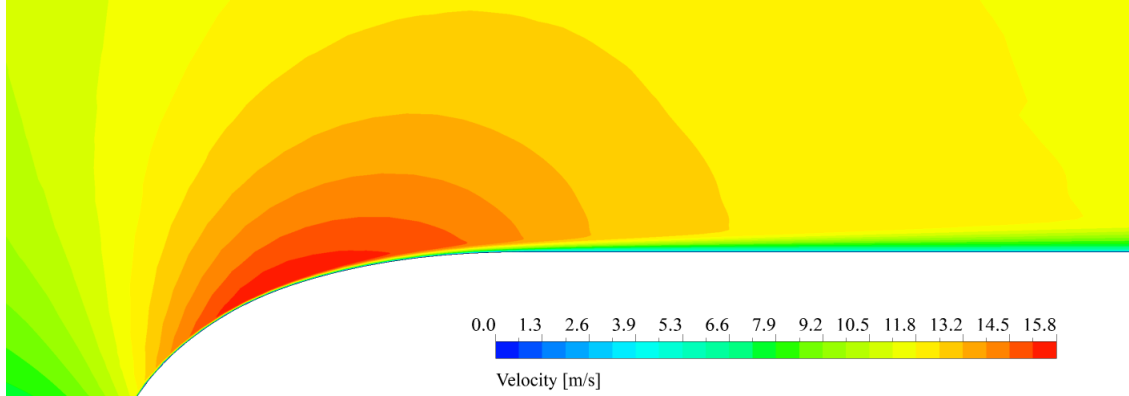
Figure 4.14: No separation bubble present on the upper surface near the leading edge of the hydrofoil in the numerical simulation with the SST $k - \omega$ model alone.
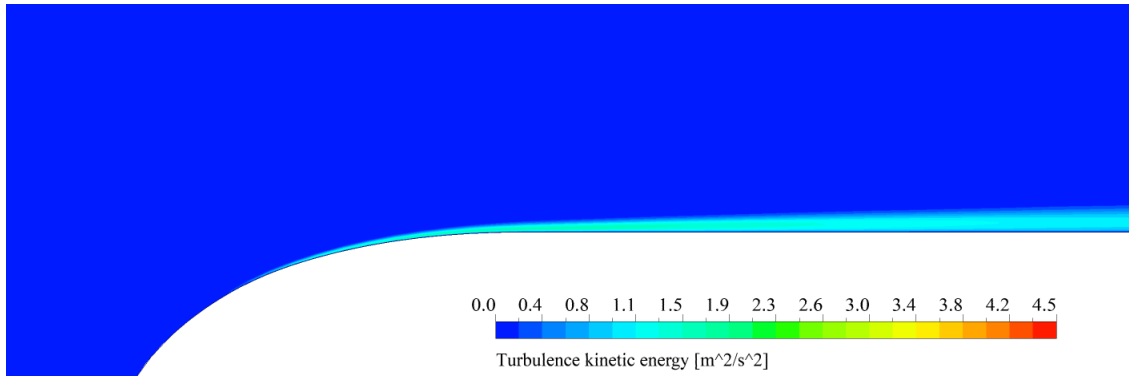

Figure 4.15: Turbulence kinetic energy on the upper surface near the leading edge of the hydrofoil from the numerical simulation with the SST $k - \omega$ model alone.

4.3.1 Amplitude frequency spectra

To find the vortex shedding frequency, the velocity V in a point $z = 25$ mm downstream of the trailing edge was sampled over time, and the resulting data was transformed to a representation in the frequency domain using FFT. This was done in MATLAB through a P.D. Welch power spectrum analysis, as presented in Appendix C. The velocity data are sampled over time intervals corresponding to approximately 100 shedding periods in the simulations. The results are amplitude frequency spectra for the vortex shedding as presented in Fig. 4.16 and Fig. 4.17.

Fig. 4.16 shows the amplitude frequency spectrum from the simulation with the SST $k - \omega$ model. The estimated frequency of the vortex shedding is according to this 474.76 Hz, with an amplitude of 2.04 m/s. The amplitude frequency spectrum from the simulation with the SST $k - \omega$ model in combination with the $\gamma - Re_\theta$ transition model is presented in Fig. 4.17, and shows an estimated shedding frequency of 489.76 Hz with an amplitude of 2.61 m/s. One can also observe a second and third harmonic shedding frequency in both amplitude frequency spectra. These are at approximately 955 Hz and 1430 Hz in Fig. 4.16 and 980 Hz and 1470 Hz in Fig. 4.17, respectively.

In the spectrum from the transition model simulation, the shedding frequency is estimated to be 3.2 % higher than for the pure SST $k - \omega$ model simulation, while the amplitude is simulated to be 27.9 % higher. The numerically obtained shedding frequencies are, from the simulations with and without the transition model, 11.3 % and 7.9 % higher than the estimated Strouhal shedding frequency of 440 Hz, respectively.

The experiment conducted by Sagmo et al. [33] gave a shedding frequency of 551 Hz with a standard deviation of 35 Hz. This shedding frequency is approximately 12.5 %, or 61 Hz, higher than the shedding frequency obtained from the transition model simulation in this master thesis. For the simulation with the SST $k - \omega$ model alone, the experimentally obtained shedding frequency is approximately 16.1 %, or 76 Hz, higher
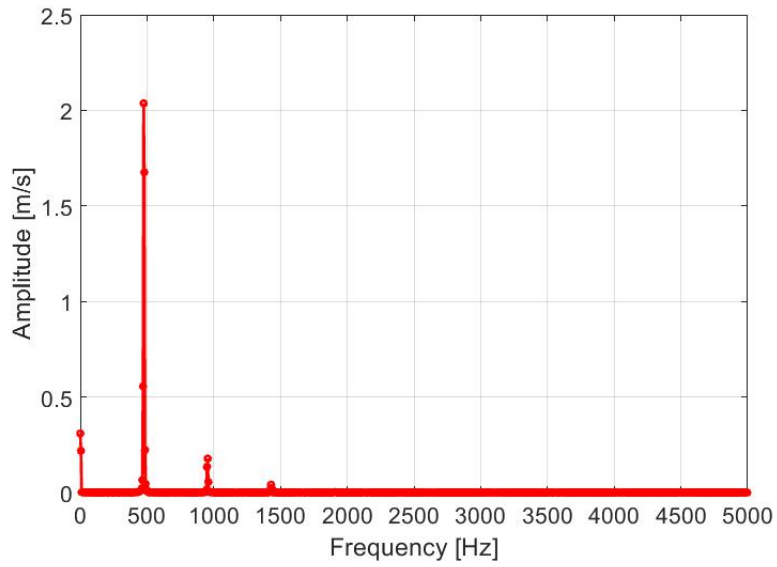
Figure 4.16: Amplitude frequency spectrum from simulation with the SST $k - \omega$ model. Estimated shedding frequency = 474.76 Hz, amplitude = 2.04 m/s.
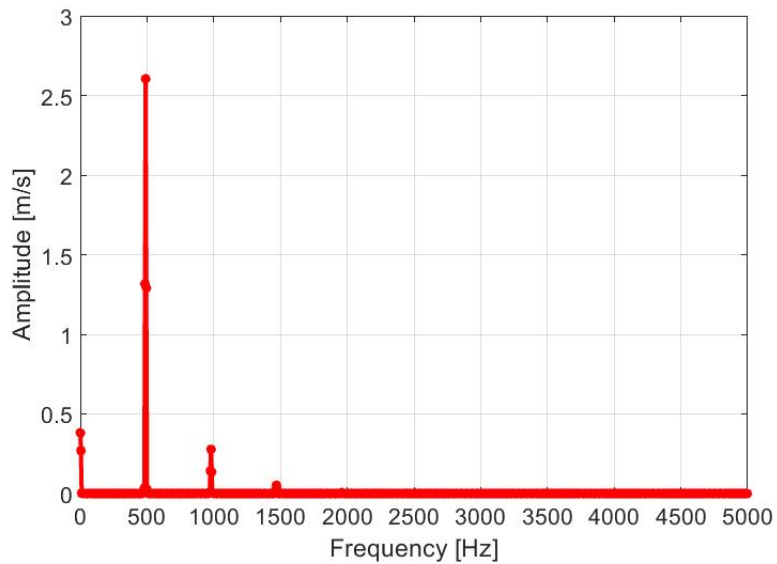

Figure 4.17: Amplitude frequency spectrum from simulation with the SST $k - \omega$ model and the $\gamma - Re_\theta$ transition model. Estimated shedding frequency = 489.76 Hz, amplitude = 2.61 m/s.

Table 4.1: Shedding frequencies and the corresponding amplitudes.

Origin	Method	Frequency	Amplitude
Master thesis	SST $k - \omega$ model	474.76 Hz	2.04 m/s
	SST $k - \omega$ model with transition model	489.76 Hz	2.61 m/s
	Strouhal shedding frequency	440 Hz	-
Work of Sagmo et al. [33]	Experiment	551 Hz	-
	SST $k - \omega$ model	~ 475 Hz	-

than the simulated shedding frequency.

Also numerical simulations were conducted in the work of Sagmo et al. [33], and some of the results from their simulation with the SST $k-\omega$ model will be used for comparison. All of the shedding frequencies subjected to discussion are presented in Table 4.1, including the estimated Strouhal shedding frequency from Section 2.1.3.

It is evident that the shedding frequencies from the simulations in this master thesis are underpredicted compared with the measured shedding frequency from the experiment. This was also the case for the numerical simulation that is presented in the paper by Sagmo et al. [33]. The shedding frequency from the pure SST $k-\omega$ model simulation in this master thesis and the numerically obtained shedding frequency from the SST $k-\omega$ model simulation in the work of Sagmo et al. [33] are however in very good agreement with each other. These results are obtained on very different meshes, which suggests that the estimated shedding frequency of about 475 Hz is a fairly accurate result for the SST $k-\omega$ model on this geometry and with these flow conditions. The general underprediction might then indicate a weakness in the SST $k-\omega$ model for the estimation of the vortex shedding frequency in this type of flow.

Even though the shedding frequency results from this study and the work of Sagmo et al. [33] are corresponding, the mesh independence study did not suggest perfect mesh independence. In the mesh independence study there was an apparent relation between the mesh resolution and the shedding frequency, in the sense of obtaining a higher shedding frequency with a finer mesh. With more time and computational resources, this would be interesting to investigate further. It is still possible that some of the underprediction in the simulated shedding frequencies is related to the mesh quality.

There have been obtained results indicating that a delayed separation point leads to increased shedding frequencies in previous studies for similar trailing edge geometries [16] [33]. According to this, the underprediction in the numerically estimated shedding frequencies suggests that the boundary layer separation points are estimated to lie too far upstream on the surface of the hydrofoil. It may not be unreasonable to expect this to be the case for the separation point on the upper surface of the hydrofoil where the geometry is curved, which makes the position of the separation point harder to estimate than on the lower, straight surface.

It is also evident that, however underpredicted, the shedding frequency obtained with the transition model is a closer estimation to the experimentally obtained shedding frequency than the shedding frequency from the pure SST $k-\omega$ model simulation. Since the shedding frequency is dependent on the location of the separation point, which in turn is dependent on the simulation of the boundary layer, it is not surprising that the transition model has a result that is closer to the experiment. The transition model is expected to estimate the development of the boundary layer more realistically than the SST $k-\omega$ model does alone, and judging by the shedding frequencies, it does.

4.3.2 Velocity profiles in the wake

The time-averaged streamwise velocity profiles at two vertical lines in the wake, $z = 9.9D$ and $z = 13.3D$ downstream of the trailing edge, are presented in Fig. 4.18 and Fig. 4.19. In each figure, the numerically obtained velocity profiles from the two simulations using the SST $k-\omega$ model with and without the $\gamma - Re_\theta$ transition model are plotted, in addition to the experimentally obtained velocity profile by Sagmo et al. [33]. The numerically simulated velocity profiles are referred to in the legends as *Transition model* and *SST $k-\omega$ model*, respectively.

The velocity profiles from the numerical simulations are time-averaged over an interval corresponding to approximately 100 shedding periods. The numerically obtained velocities are normalized with respect to the

Figure 4.18: Time-averaged streamwise velocity profiles from experiment by Sagmo et al. [33] and numerical simulations of this master thesis at position $z = 9.9D$ downstream of the trailing edge.
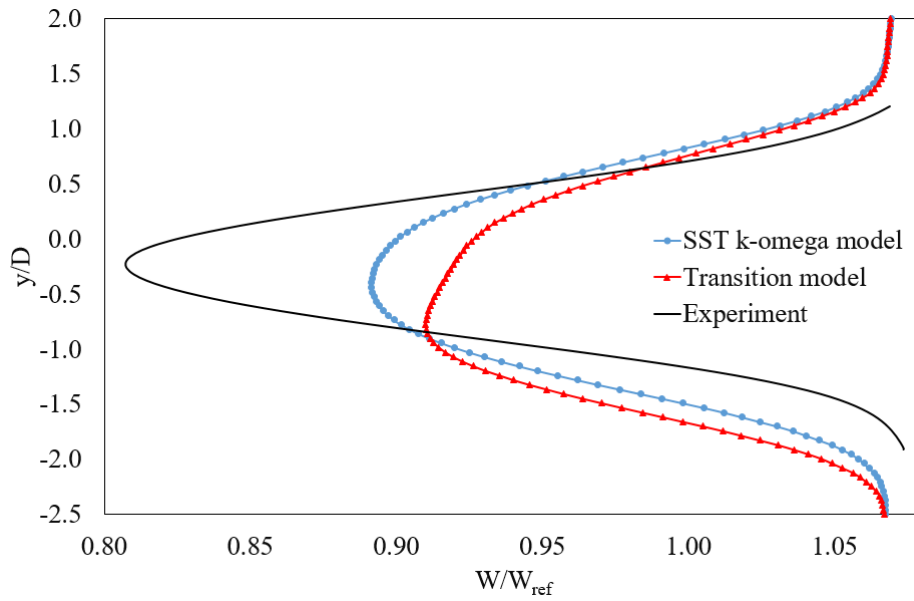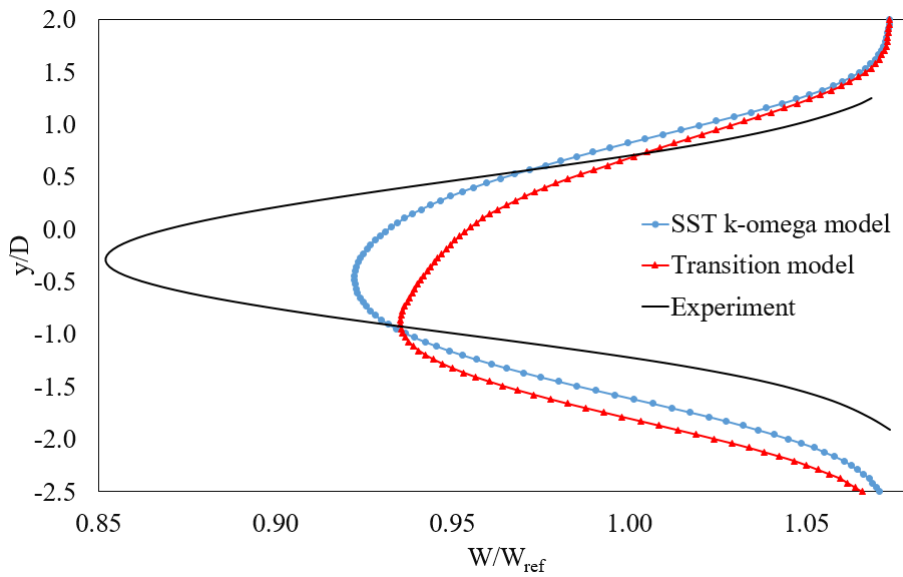

Figure 4.19: Time-averaged streamwise velocity profiles from experiment by Sagmo et al. [33] and numerical simulations of this master thesis at position $z = 13.3D$ downstream of the trailing edge.

reference velocity $W_{ref} = 9.6$ m/s. The experimentally obtained velocities are normalized with respect to the measured mean channel velocity in the experiment, which was 9.637 m/s. The height is normalized by the trailing edge thickness D, with $y = 0$ set at the hydrofoil centerline.

As observed for the shedding frequency, the SST $k - \omega$ model simulation in this master thesis performs very similarly to the SST $k - \omega$ model simulation in the paper by Sagmo et al. [33], judging by the velocity profiles. It is evident that the numerical simulations predict a smaller velocity deficit than what was obtained in the experiment. This underestimation of the velocity deficit suggests a weakness in the SST $k - \omega$ model for this type of flow.

Another trend that is present for both the simulations of this master thesis and the simulations and experiment in the paper paper by Sagmo et al. [33], is that the wake center is consistently shifted slightly below the centerline of the hydrofoil. This is believed to be an effect of the asymmetric geometry, where the upper separation point is allowed to travel closer to the centerline of the hydrofoil because of the curvature.

The width of the wakes can give an indication of the relative positions of the separation points on the foil, where a wider wake should imply separation points located further upstream on the foil surface than for a more narrow wake. Based on this theory, the separation points in the experiment are expected to be located closer to the trailing edge than the separation points in the numerical simulations are, due to a more narrow wake in Fig. 4.18 and Fig. 4.19. This is in good agreement with the discussion of the underpredicted shedding frequencies from the numerical simulations, where the reason for the underprediction was suggested to be that the estimated separation points were located too far upstream on the surface, with respect to the trailing edge.

It is also interesting to note that while the transition model simulation estimated the shedding frequency that was the closest to the experimentally obtained shedding frequency, the estimated velocity profile from the transition model simulation is the one that differ the most from the experiment. The velocity deficit is smaller for the transition model, and there is also a characteristic asymmetry in the velocity profile that persists for both $z = 9.9D$ and $z = 13.3D$. This demonstrates that how similarly the turbulence model estimates the velocity profile in the wake compared with the experiment, is not necessarily a good indication of how well it predicts the shedding frequency.

Chapter 5

Conclusion

CFD simulations have been conducted on a hydrofoil with a blunt, asymmetrical trailing edge, with the SST $k - \omega$ turbulence model alone and in combination with a laminar to turbulent transition model. The emphasis has been on the developing boundary layer and consequent wake and shedding frequencies of the hydrofoil. The dependence on location of the inlet boundary and on turbulence parameters was also investigated and quantified for simulations with the SST $k - \omega$ model. The simulation results have been compared with experimentally and numerically obtained data produced by Sagmo et al. [33] on the same hydrofoil, with the following outcomes:

1) The simulation performed with the SST $k - \omega$ model alone in this study recreates the results obtained by Sagmo et al. [33] with the same model well.

2) The $\gamma - Re_\theta$ transition model estimates a shedding frequency that is closer to the experimentally obtained shedding frequency than the SST $k - \omega$ model does alone.

3) There is a general underprediciton of both the shedding frequency and the velocity deficit in the wake by the numerical simulations.

4) The numerical simulations predict a wider wake than what was obtained in the experiment.

The overpredicted width of the wakes and the underpredicted shedding frequencies indicate that the separation points of the boundary layer are estimated to lie too far upstream on the hydrofoil surface. This shows the difficulties in the modelling of the separation points and the consequent wake and shedding frequencies for the SST $k - \omega$ model.

The results of this study contribute to shedding light upon numerical simulation of flow over the geometry at hand, and facilitate further studies on the vortex shedding phenomenon. The geometry of the hydrofoil is open to the public (available through the project *Francis-99* by NVKS), which means that anyone can perform simulations on the same geometry, and that the results of this work may serve as a basis for direct comparison.

Chapter 6

Further work

The most interesting and valuable further work would be to accomplish simulations with either the DES or LES method. To do this, one should find a meshing method with higher node efficiency to reduce the size of the mesh. This would give lower demands for computational power for the mesh generation and the actual simulation, which proved to be the critical factor for the success of DES/LES in this study. Alternatively, getting access to more computationally powerful resources would also enable this type of simulation.

For the RANS simulations, there are several aspects that can be investigated further. The thickness of the inflation layers and the general resolution of the mesh could be increased to explore the mesh independence, or rather *dependence*, more thoroughly, especially with respect to the shedding frequency, which was seen to be better estimated for higher resolutions. It would be interesting to do a turbulence parameters dependence study for simulations conducted with the $\gamma - Re_\theta$ transition model as well, in order to quantify what effect the turbulence intensity at the inlet would have in that case. The transition model simulation results are expected to be more sensitive to the inflow turbulence than the SST $k - \omega$ model simulation results, due to the transition model's dependence on the turbulence intensity for the prediction of the transition [24].

Another thing that could be altered is the target value of the residual level. This study's target value of 1e-04 is considered as a relatively loose convergence, so for further work the value could be changed to 1e-05, which is regarded as a good convergence.

References

[1]   ANSYS Inc 2018. *ANSYS CFX 19.2 Documentation.*

[2]   J. Boussinesq. *Essai sur la théorie des eaux courantes.* Impr. nationale, 1877.

[3]   H. Brekke. *Proceedings of the 17th IAHR Symposium, Beijing, China.* pp. 15-19. 1994.

[4]   I. B. Celik, Z. N. Cehreli, and I. Yavuz. "Index of resolution quality for large eddy simulations". In: vol. 127. 5. 2005, pp. 949–958.

[5]   I. B. Celik, Z. N. Cehreli, and I. Yavuz. "Index of resolution quality for large eddy simulations.(Author Abstract)". In: *Journal of Fluids Engineering* 127.5 (2005). ISSN: 0098-2202.

[6]   I. B. Celik et al. "Procedure for Estimation and Reporting of Uncertainty Due to Discretization in CFD Applications". eng. In: *Journal of Fluids Engineering (Transactions of the ASME)* 130.7 (2008), 078001 (4)–078001 (4).

[7]   Y. A. Çengel and J. M. Cimbala. *Fluid mechanics: fundamentals and applications.* eng. 3rd ed. in SI units. Boston: McGraw-Hill, 2014. ISBN: 9781259011221.

[8]   P. A. Davidson. *A Voyage Through Turbulence.* eng. Cambridge University Press, 2011. ISBN: 1-283-31660-9.

[9]   T. Do, L. Chen, and J. Tu. "Numerical study of turbulent trailing-edge flows with base cavity effects using URANS". eng. In: *Journal of Fluids and Structures* 26.7 (2010), pp. 1155–1173. ISSN: 0889-9746.

[10]   P. A. Durbin and B. A. Pettersson Reif. *Statistical Theory and Modeling for Turbulent Flows.* eng. Chichester, UK: John Wiley & Sons, Ltd, 2010. ISBN: 9780470689318.

[11]   M. Eckert. "Turbulence before Marseille 1961". In: *Journal of Turbulence* 13.N44 (2012). DOI: 10.1080/14685248.2012.725476.

[12]   J. H. Ferziger. *Computational methods for fluid dynamics.* eng. 3rd, rev. ed. Berlin: Springer, 2002. ISBN: 3540420746.

[13]   C. P. Häggmark, C. Hildings, and D. S. Henningson. "A numerical and experimental study of a transitional separation bubble". eng. In: *Aerospace Science and Technology* 5.5 (2001), pp. 317–328. ISSN: 1270-9638.

[14]   D. Hartog and J. Pieter. *Mechanical vibrations.* Courier Corporation, 1985.

[15]   W. Henley. *2019 Hydropower Status Report.* International Hydropower Association. 2019. URL: https://www.hydropower.org/sites/default/files/publications-docs/2019_hydropower_status_report_0.pdf.

[16]   G. Heskestad and D. R. Olberts. "Influence of Trailing-Edge Geometry on Hydraulic-Turbine-Blade Vibration Resulting From Vortex Excitation". In: *Journal of Engineering for Power* 82 (1960), pp. 103–109.

[17]   ANSYS Inc. *Ask the Turbulence Expert: Dr. Florian Menter.* Accessed on May 22, 2019. URL: https://www.ansys.com/products/fluids/turbulence-modeling/ask-the-expert.

[18]   *International Hydropower Association - Country profile - Norway.* Accessed on May 28, 2019. URL: https://www.hydropower.org/country-profiles/norway.

[19]   J. Klapp and A. Medina. *Experimental and computational fluid mechanics.* eng. Environmental science and engineering (Springer (Firm)). Cham, Germany: Springer, 2014. ISBN: 3-319-00116-7.

[20]   P. K. Kundu and I. M. Cohen. *Fluid mechanics.* 4th ed. Amsterdam: Elsevier Academic Press, 2007.

[21] R. B. Langtry. "A Correlation-based Transition Model Using Local Variables for Unstructured Parallelized CFD Codes". PhD thesis. Institute of Thermal Turbomachinery and Machinery Laboratory, University of Stuttgart, 2006.

[22] R. B. Langtry and F. R. Menter. "Transition Modeling for General CFD Applications in Aeronautics". eng. In: *AIAA Paper 2005-522* (2005). Reno, Nevada.

[23] J. L. Lumley and A. M. Yaglom. "A Century of Turbulence". In: *Flow, Turbulence and Combustion* 66.3 (May 2001), pp. 241–286. ISSN: 1573-1987. DOI: 10.1023/A:1012437421667.

[24] P. Malan, K. Suluksna, and E. Juntasaro. "Calibrating the gamma-Re_theta transition model for commercial CFD". In: *47th AIAA Aerospace Sciences Meeting Including The New Horizons Forum and Aerospace Exposition*. 2009, p. 1142.

[25] F. R. Menter. "Two-equation eddy-viscosity turbulence models for engineering applications". In: *AIAA Journal*. Vol. 32. 8. 1994, pp. 1598–1605.

[26] F. R. Menter et al. "A Correlation-Based Transition Model Using Local Variables Part I: Model Formulation". eng. In: *Journal of Turbomachinery (Transactions of the ASME)* 128.3 (2004), pp. 413–422. DOI: 10.1115/1.2184352.

[27] F. Menter, R. Langtry, and S. Völker. "Transition Modelling for General Purpose CFD Codes". eng. In: *Flow, Turbulence and Combustion* 77.1 (2006), pp. 277–303. ISSN: 1386-6184.

[28] S. B. Pope. *Turbulent flows*. eng. Cambridge: Cambridge University Press, 2000. ISBN: 0521591252.

[29] D. Reay. "Fast Fourier Transform". eng. In: *Digital Signal Processing and Applications with the OMAP-L138 eXperimenter*. Hoboken, NJ, USA: John Wiley & Sons, Inc., 2012, pp. 212–278. ISBN: 9780470936863.

[30] O. Reynolds. "An experimental investigation of the circumstances which determine whether the motion of water shall be direct or sinuous and the law of resistance in parallel channels". In: *Philosophical Transactions of the Royal Society of London. A* 174 (1883), pp. 935–982.

[31] O. Reynolds. "On the dynamical theory of incompressible viscous fluids and the determination of the criterion". In: *Philosophical Transactions of the Royal Society of London. A* 186 (1895), pp. 123–164.

[32] W. Rodi. "Turbulence Modeling and Simulation in Hydraulics: A Historical Review". eng. In: *Journal of Hydraulic Engineering* 143.5 (2017). ISSN: 0733-9429.

[33] K. F. Sagmo et al. "PIV measurements and CFD simulations of a hydrofoil at lock-in". In: *29th IAHR on Hydraulic Machinery and Systems*. 2018.

[34] J. Smagorinsky. "General Circulation Experiments with the Primitive Equations". In: *Monthly Weather Review* 91.3 (1963), pp. 99–164.

[35] P. R. Spalart. "Detached-Eddy Simulation". In: *Annual Review of Fluid Mechanics* 41.1 (2009), pp. 181–202.

[36] P. R. Spalart. *Young-Person's Guide to Detached-Eddy Simulation Grids - NASA/CR-2001-211032*. eng. Tech. rep. 2001.

[37] P. R. Spalart and C. L. Rumsey. "Effective Inflow Conditions for Turbulence Models in Aerodynamic Calculations". eng. In: *AIAA Journal* 45.10 (2007), pp. 2544–2553. ISSN: 0001-1452.

[38] P. R. Spalart et al. "Comments on the Feasibility of LES for Wings, and on a Hybrid RANS/LES Approach". In: Jan. 1997.

[39] M. Strelets. "Detached eddy simulation of massively separated flows". In: *AIAA J* (Jan. 2001), pp. 1–18.

[40] V. Strouhal. In: *Annalen der Physik* 241 (1878), pp. 216–251.

[41] H. Tennekes and J. L. Lumley. *A First Course in Turbulence*. 1st ed. MIT Press, 1972.

[42] *U.S. Energy Information Administration*. Accessed on May 28, 2019. URL: https://www.eia.gov/energyexplained/index.php?page=hydropower_home.

[43] H. K. Versteeg and W. Malalasekera. *An Introduction to Computational Fluid Dynamics*. 2nd ed. Pearson Education Limited, 2007.

[44] Z. Yang. "Large-eddy simulation: Past, present and the future". eng. In: *Chinese Journal of Aeronautics* 28.1 (2015), pp. 11–24. ISSN: 1000-9361.

Appendix A - DES mesh

Even though no simulations were conducted with either of the two CFD techniques LES or DES, the ambition of accomplishing successful simulations with one of the two were present from the beginning of the work with this master thesis. The purpose of this text is to present the work as far as it got to assist any further work on DES simulations for the given geometry and flow.

After assessing the amount of computational resources available for this project, it was decided to aim at simulations with the least demanding technique (of the two mentioned above) regarding computational power, namely DES. DES is a hybrid formulation that switches between RANS and LES based on the mesh resolution provided [38]. In regions of the mesh where the element size is below a certain limit, the DES-limiter is activated and switches the model from RANS to LES mode. LES has much stricter requirements to mesh resolution than RANS, since with LES the larger-scale motions are computed explicitly, and only the effects of the smaller-scale motions are modelled [28]. This is performed through a filtering operation, where the required grid spacing is proportional to the specified filter width.

The idea for the case at hand was to have a mesh of fine enough resolution for LES to be applied in the wake of the hydrofoil, and let RANS take care of the rest of the domain, including the boundary layers. Since we already know how RANS simulates this flow, it was clear that to make the DES simulation worthwhile, there must be a minimum size of the LES region. This minimum size was considered to be an extended version of the first inner body of influence we know from the mesh used in the pure RANS simulations in this master thesis. See this idea presented in Fig. 1, with said body of influence marked by a red rectangle, and stapled lines indicating how it should be extended. The extension length is based on where the closest velocity profile to the trailing edge is sampled, which is at $z = 9.9D$ downstream of the trailing edge. An LES region of this minimum size would have both the point for the sampling of the shedding frequency and one of the sampling lines for the time-averaged streamwise velocity profile covered.
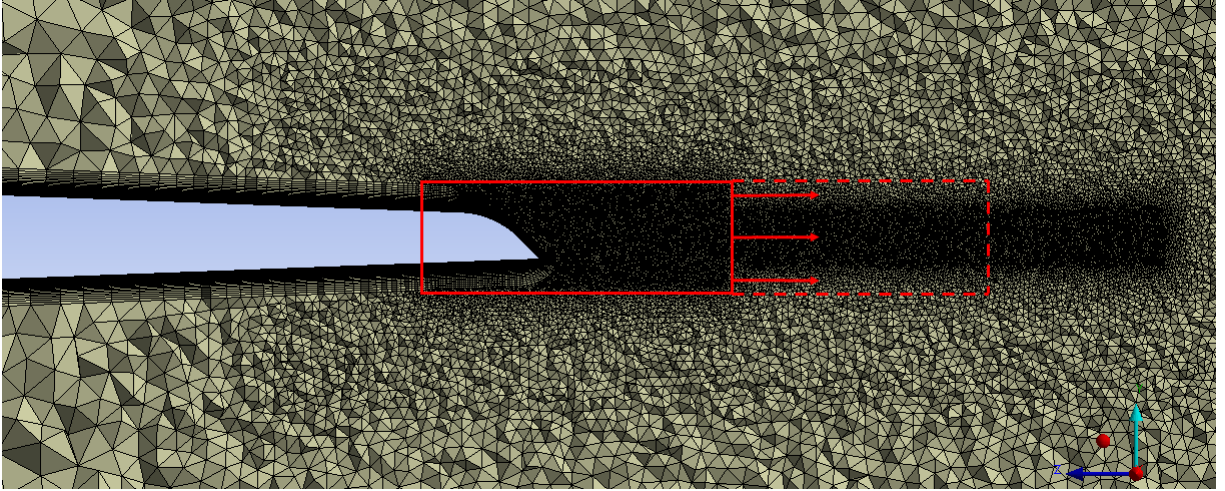

Figure 1: Extension of inner body of influence, marking the LES region needed to make the DES simulation worthwhile. Here illustrated on a RANS mesh.

It can be hard to predict a sufficiently small element size for the LES region, and as stated in the very useful paper "Young-Person's Guide to Detached-Eddy Simulation Grids" by Spalart [36], there is no unique way to choose the target grid spacing Δ for LES. To keep the computational costs as low as possible, it is important not to use smaller elements than strictly necessary for the method to work as desired. As a starting point, the element size in the LES region of the mesh was suggested to be in the range $\frac{1}{100}D \leq \Delta \leq \frac{3}{100}D$, which corresponds to $4.8 \cdot 10^{-5}$m $\leq \Delta \leq 1.44 \cdot 10^{-4}$m with D denoting the trailing edge thickness of 4.8 mm. With this target spacing follows a timestep, calculated as

$$\Delta t = \frac{\Delta}{U_{bulk}} \tag{1}$$

where U_{bulk} is the bulk velocity of the flow. This gives a timestep in the the range $5 \cdot 10^{-6} \leq \Delta t \leq 1.5 \cdot 10^{-5}$.

The Kolmogorov microscale of length, i.e. the length scale of the smallest eddies, was also calculated for the flow at hand. The target spacing of the LES region should be larger than this, or else the CFD technique would tend to DNS [4]. This is why there exists no such thing as a mesh independent LES in theory - it would essentially be a DNS, and the philosophy of LES would lose its meaning. The Kolmogorov microscale of length is calculated as ([10], p. 18):

$$\eta \sim l_0 Re_t^{-3/4} \tag{2}$$

where l_0 is the length scale of the larger eddies, which in this case is estimated to be in the scale of the trailing edge thickness D, and the turbulent Reynolds number Re_t is calculated based on the trailing edge thickness as Re_D. This gives

$$Re_t = Re_D = \frac{UD}{\nu} = \frac{9.6\text{m/s} \cdot 4.8 \cdot 10^{-3}\text{m}}{9.902 \cdot 10^{-7}\text{m}^2/\text{s}} = 46536.05 \tag{3}$$

where U is the velocity scale estimated to be in the scale of the bulk velocity and ν is the kinematic viscosity, which is $9.902 \cdot 10^{-7}$ m^2/s at 20.5°C. This gives a Kolmogorov microscale of length of $1.515 \cdot 10^{-3}$ m. A target grid spacing in the LES region that is in the scale $10 \cdot \eta$ is regarded as reasonable, while the scale $100 \cdot \eta$ is expected to be too high.

The Kolmogorov time-scale of the small eddies can be found from the time-scale of the large eddies and the turbulent Reynolds number ([10], p. 18):

$$t_\eta \sim t_0 Re_t^{-1/2} \tag{4}$$

where t_0 is the time-scale of the larger eddies approximated as D/U, i.e. the length scale of the larger eddies divided by the velocity scale, and Re_t is estimated as Re_D. From this, the time-scale of the small eddies is $2.318 \cdot 10^{-6}$ s.

The least expensive way to obtain the desired target spacing Δ is to have cubic mesh elements, since in DES we have $\Delta = \max(\Delta x, \Delta y, \Delta z)$ [36]. Another argument for cubic mesh elements is that physically, the premise of LES is to filter out only eddies that are small enough to be products of the energy cascade, and therefore to be statistically isotropic. This means that from both a numerical and a physical point of view, finer spacing in one or even two directions is wasted. To obtain cubic elements, the meshing method that have been used for the RANS simulations in this master thesis must be changed to a method that creates a hexahedral mesh.

An ideal DES study contains results from simulations on two meshes: one mesh with a target grid spacing Δ and a second mesh with a target grid spacing $\Delta/2$ [36]. This is a way of assessing the quality of the mesh, and it was a part of the original plan to conduct this in the master thesis. The results from the two DES simulations were also to be compared with the experimental results. However, such large meshes require much computational power to be generated, and this turned out to be the bottle neck for this piece of work.

ANSYS Meshing was attempted used for design and generation of the mesh, and more powerful resources than an ordinary stationary computer with 32 GB RAM and 4 cores turned out to be absolutely necessary for the generation. The available HPC resource at this point was the Idun cluster at NTNU. According to ANSYS Support provided by EDRMedeso, ANSYS Meshing is not suitable to run on clusters, since it will use all the local cores available. For this purpose they recommended Fluent Meshing instead, which they claimed to be a faster mesher with great performance increases in runs on cluster. This would however lead to restricted options for obtaining the desired hexahedral mesh; if ANSYS CFX was to be used to run simulations on the Fluent mesh, one must apparently use a tetrahedral mesh. To be able to run simulations on a Fluent mesh with hexahedral elements, one must use the Fluent solver.

With no experience with Fluent Meshing or the Fluent solver, it was considered too time-consuming to take on this new CFD software in the work at this point. Additionally, the HPC resource regulations at NTNU were changed so that the availability of HPC resources to the work of this master thesis was reduced compared to what was expected when the tasks were defined, which strongly contributed to putting DES simulations out of the question.

Sadly, this is where the DES adventure of this master thesis ends. Had there been more time and computational power available, Fluent meshing or other meshing programs would be investigated for the purpose of generating a hexahedral mesh that is capable of running the DES simulations as desired. With a generated mesh at hand, a subgrid model would have to be chosen. Then, a first simulation on the mesh would have to be performed to check if the grid sizing activated the RANS and LES modes as desired. If it did not, the mesh would have to be changed and generated again, until the RANS and LES regions were as designed for.

Appendix B - Memo

Memo of the 3D model of the blade cascade rig.

MEMO

To	All participants		
cc			
From	Bjørn Winther Solemslie, Carl Werdelin Bergan		
Place	Waterpower Lab, NTNU	Date:	30.09.2016
Subject:	WP 1.1 : 3D model of the cascade rig		

1. Introduction

Manufacturing of the cascade rig designed in connection to WP 1.1 – blade cascade is at this time close to finish. The finished design is presented here and the 3D-files are available on SharePoint under WP1.1. The file names reflect those of the CREO-Parametric files, while other formats only contain a single file. The internal part names within the other format files correspond to the file names listed in this document.

2. Overview

An overview of the cascade test rig can be seen in Figure 1 where the different parts of the test rig are noted. These parts will be further explained in the following sections. The file name of the main 3D-model, seen in Figure 1, is *cascade_rig.asm*.

Table 1 Main files of the 3D model

Main part name	File name
Upstream contracter	Upstream_contracter.asm
Straight 150x150 pipe	longstretch.asm
Test section with hydrofoil	Test_section.asm
Downstream diffuser	Downstream_diffuser.asm

Flow direction

Downstream
diffuser

Straight
150x150 pipe

Test section
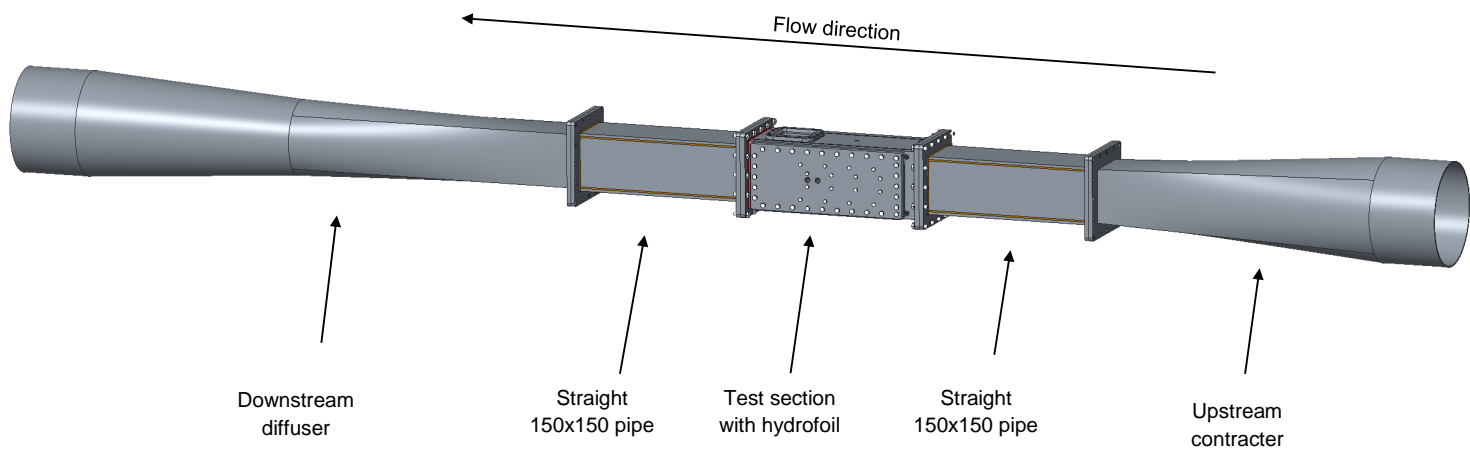with hydrofoil

Straight
150x150 pipe

Upstream
contracter

Figure 1 Overview of the cascade test rig

2.1. Upstream contracter

The upstream contracter changes the cross section of the pipe from a circular Ø300mm pipe to a square 150x150mm section. The change happens over a length of 860mm, corresponding to a taper angle of approximately 5°. The part is made up of multiple wall sections machined at the Waterpower Laboratory. The wall thickness of the contracter is 4mm and is manufactored from stainless steel.
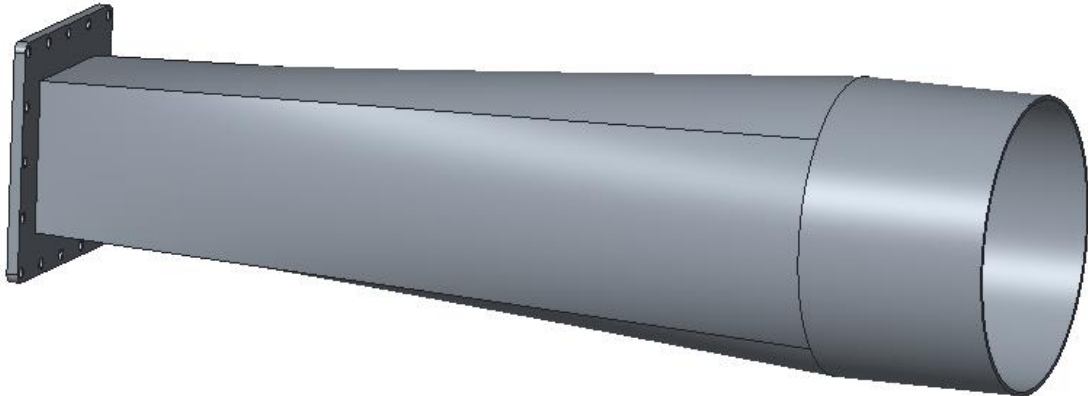

Figure 2 Upstream contracter

The flange on this contracter, and all other flanges within the test rig have a custom design in order to reduce the disturbance in the flow caused by the pipe to pipe transition. The flanges are set up as a male/female and the connection principle is shown in Figure 3. The figure shows a cross section in the centre of the pipe with the male/female connection, O-ring slot and bolt connection.
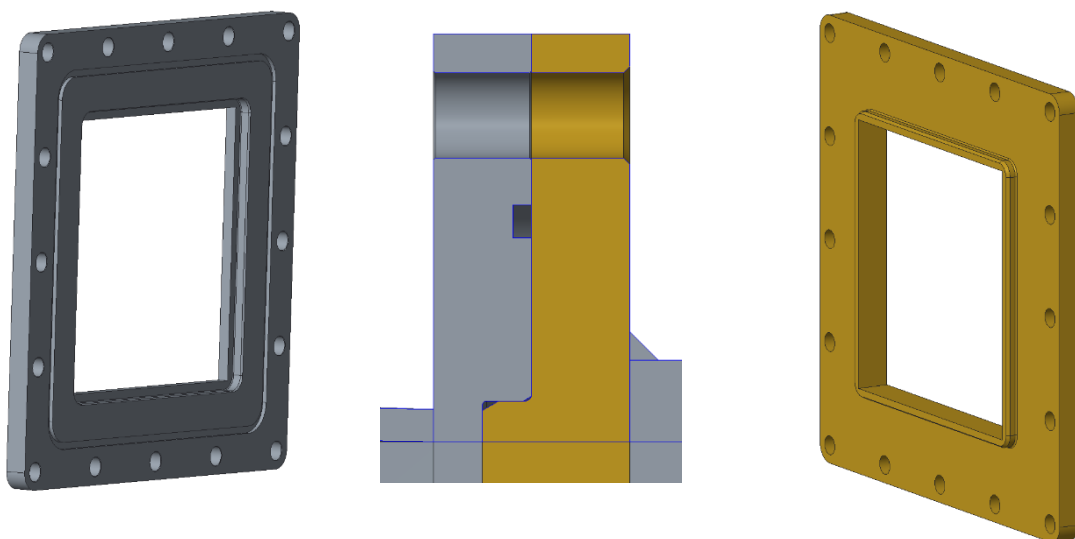

Figure 3 Flange connection principle
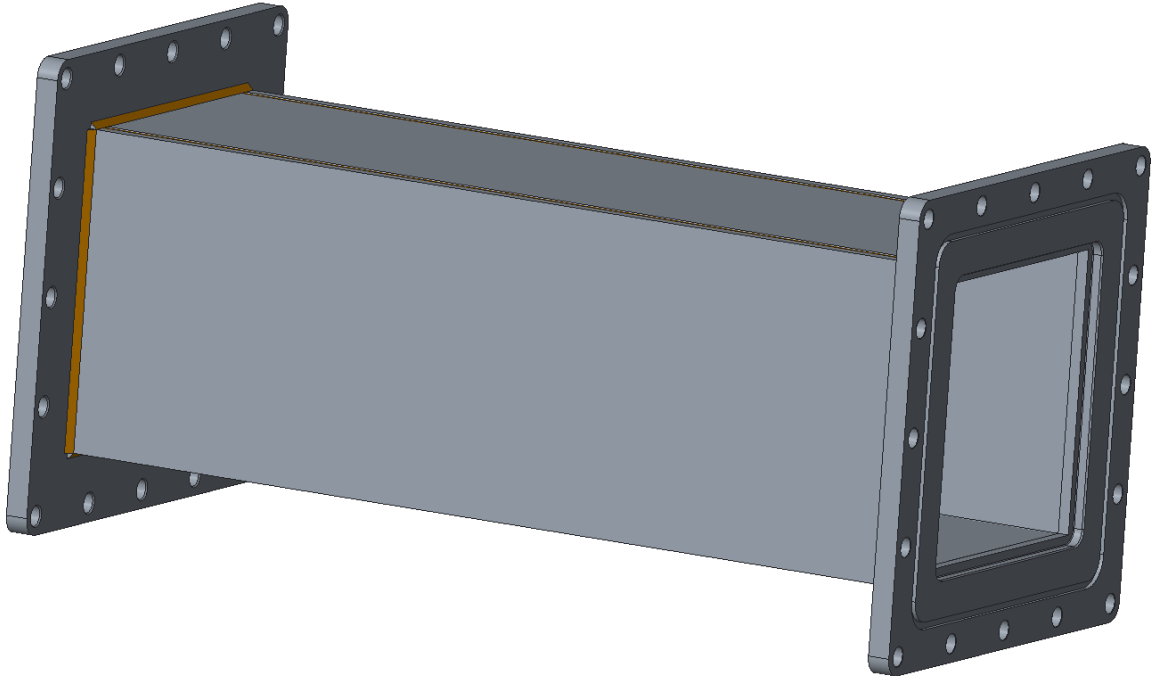
2.2.   Straight 150x150 pipe

Figure 4 Straight 150x150 pipe

The straight 150x150 pipe are installed to prevent the contracter affecting the flow within the test section. They are made up of four 10mm stainless steel plates that are welded together as shown in Figure 5 and the welding of the flange to both the 150x150 pipe and the contracter/diffuser can be seen in Figure 6.
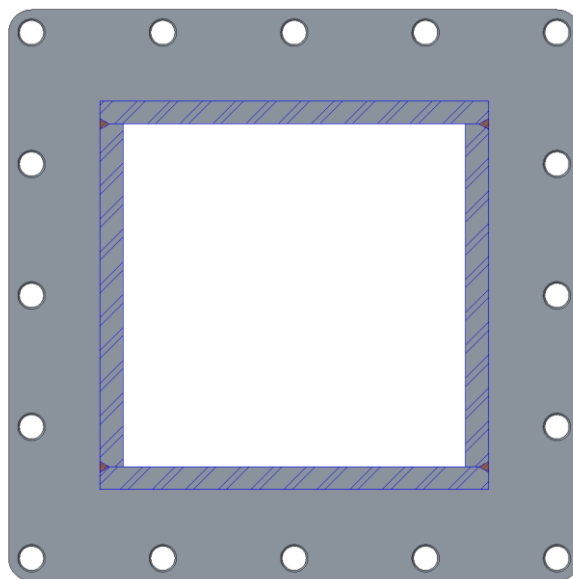

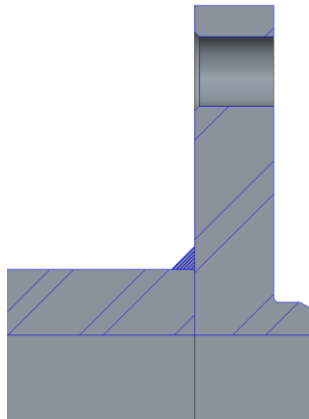*Figure 5 Welding of the walls of the straight 150x150 pipe*

Figure 6 Welding of the flanges on straight 150x150 pipe and contracter/diffuser
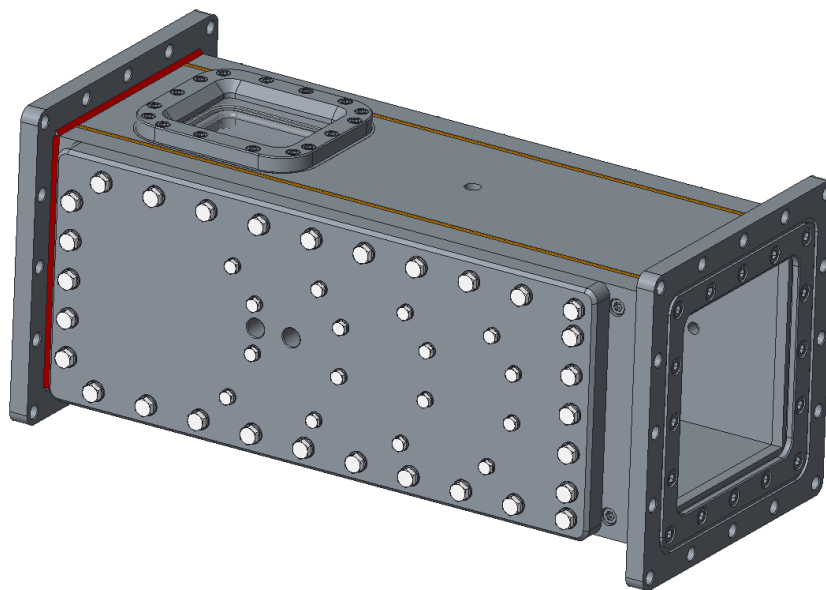
2.3. Test section with hydrofoil

Figure 7 Test section with hydrofoil

Top wall with plexiglas window for visual study

Back wall with socket and bolt holes for hydrofoil and pressure taps

Hydrofoil with instrumentation

Front wall and outer lid with bolt holes for hydrofoil and cable

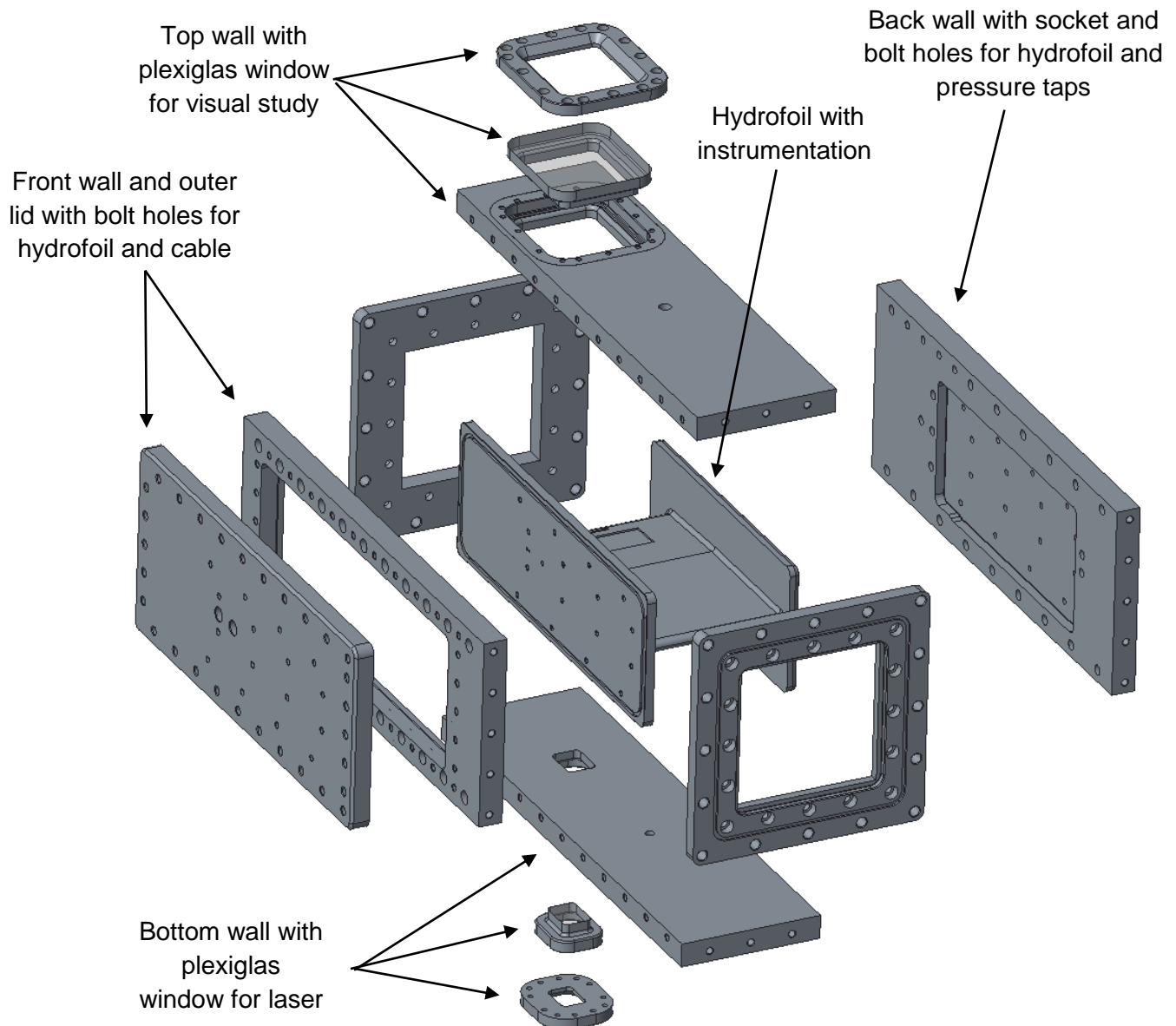Bottom wall with plexiglas window for laser

Figure 8. The walls are 25mm thick stainless steel. The thickness is chosen both to ensure that the test section is sufficiently stiff compared to the hydrofoil and to prevent deformation when the system is pressurized. The system will be pressurized by a secondary booster pump in order to prevent cavitation in the flow during measurements. The walls of the test section, along with the flanges, are mechanical joined by bolts. Welds, as seen in yellow and red in Figure 7, are used purely for sealing.
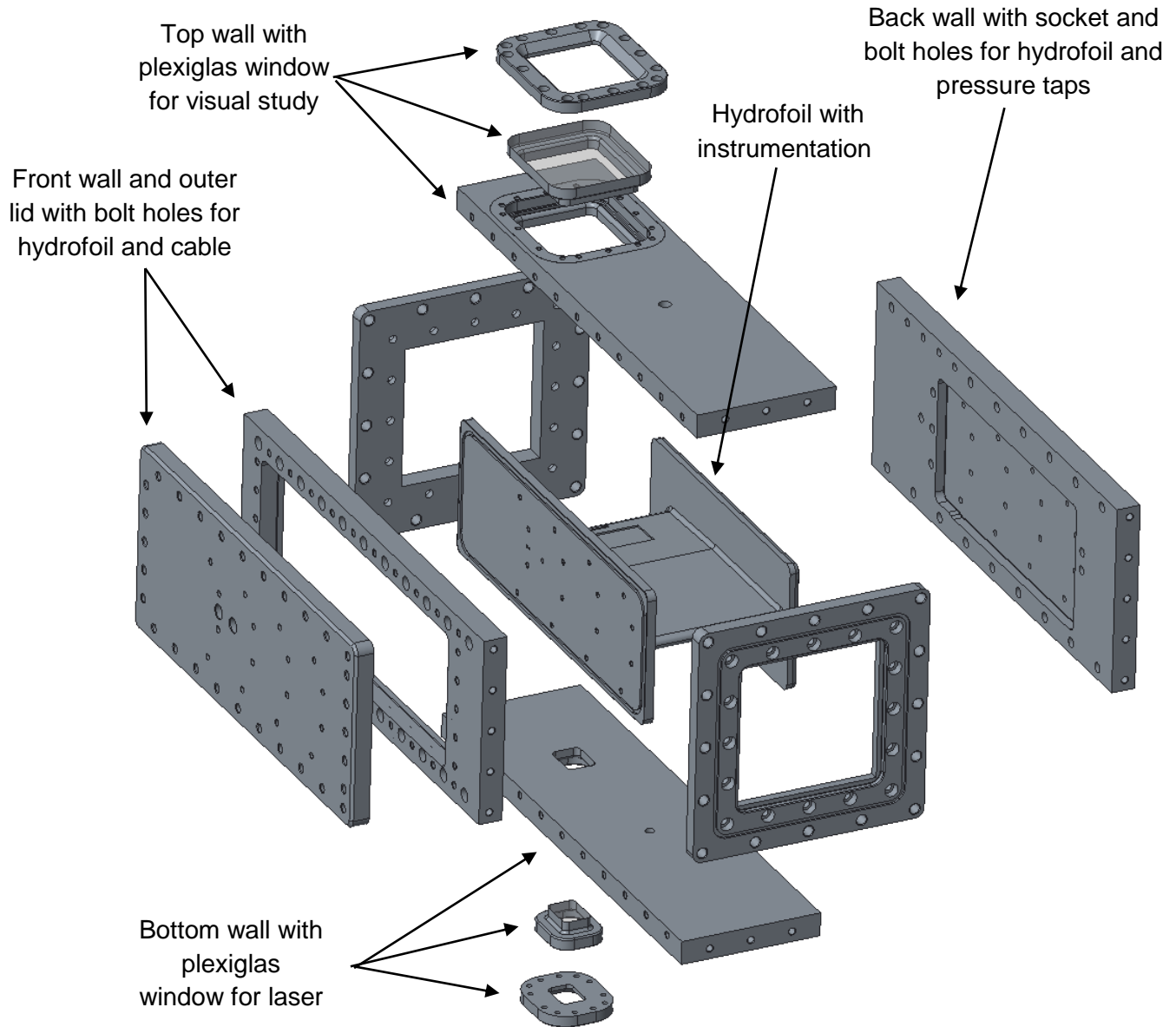
Top wall with
plexiglas window
for visual study

Back wall with socket and
bolt holes for hydrofoil and
pressure taps

Hydrofoil with
instrumentation

Front wall and outer
lid with bolt holes for
hydrofoil and cable

Bottom wall with
plexiglas
window for laser

Figure 8 Exploded view of main parts of the test section

Table 2 Files of the test section 3D-model

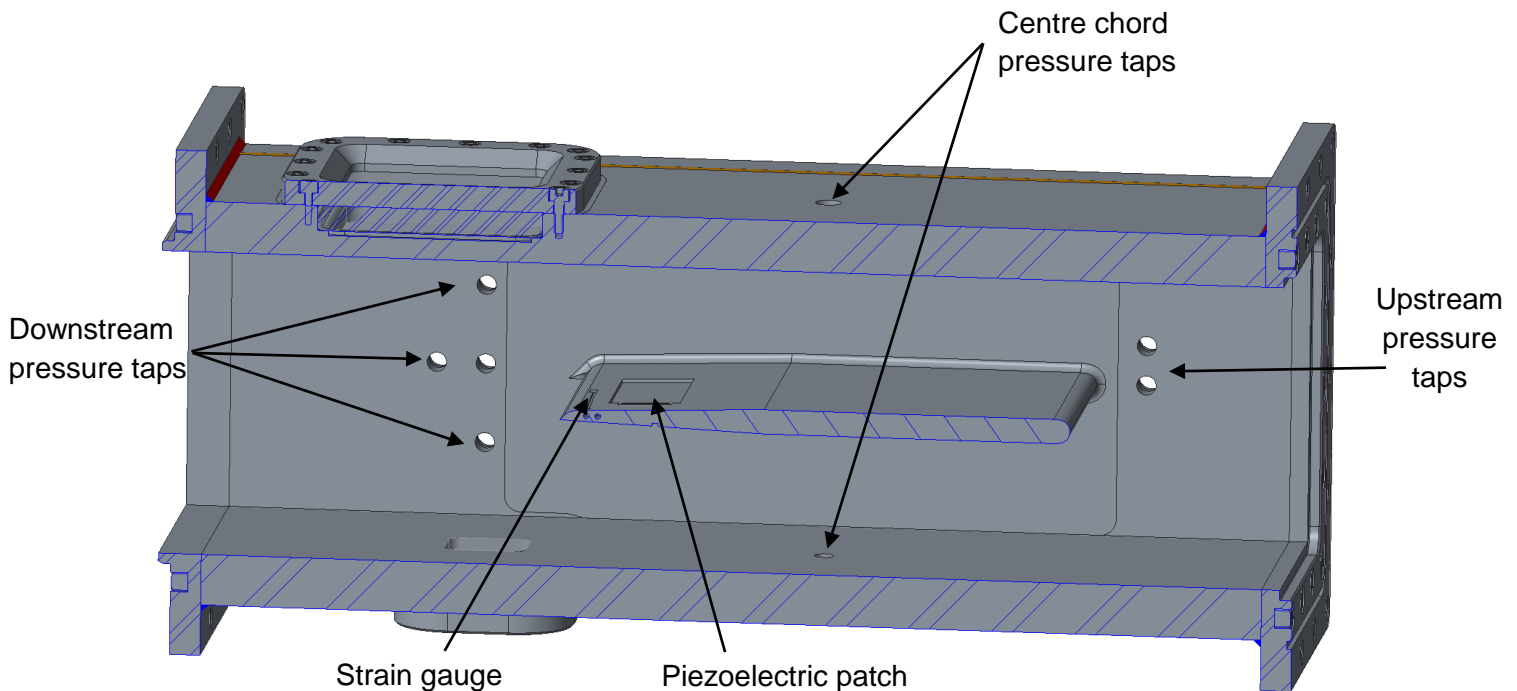| Part name	File name
Test section top wall	Test-tube-1.prt
Test section back wall	Test-tube-4.prt
Test section bottom wall	Test-tube-3.prt
Test section front wall	Test-tube-2.prt
Outer lid	Outer-lide.prt
Hydrofoil with instrumentation	Hydrofoil.prt

Test section instrumentation

Figure 9 Flow wise cross section

In Figure 9, a flow wise cross section where the instrumentation of the hydrofoil, along with both Plexiglas windows and pressure taps can be seen.

Downstream pressure taps
The middle pressure taps are positioned along the hydrofoil centre axis, four and six foil thicknesses downstream the trailing edge. The upper and lower pressure taps are placed the centre axis of the two additional hydrofoils planned for the three foil setup.

Upstream pressure taps
The lower pressure tap is placed two hydrofoil thicknesses from the leading edge, along the hydrofoil centre axis. The upper pressure tap is placed in the centre of the channel between the middle and upper hydrofoil planned for the three foil setup.

Centre chord pressure taps
The pressure taps are placed at the chord and span centre of the hydrofoil.

Piezoelectric patch
Placed in a milled recess to avoid flow interaction, two patches with symmetric placement around the chord of the hydrofoil with common cabling tunnel.

Strain gauge
Placed in a milled recess to avoid flow interaction, two patches with symmetric placement around the chord of the hydrofoil with separate cabling tunnels due to blade thickness close to the trailing edge.
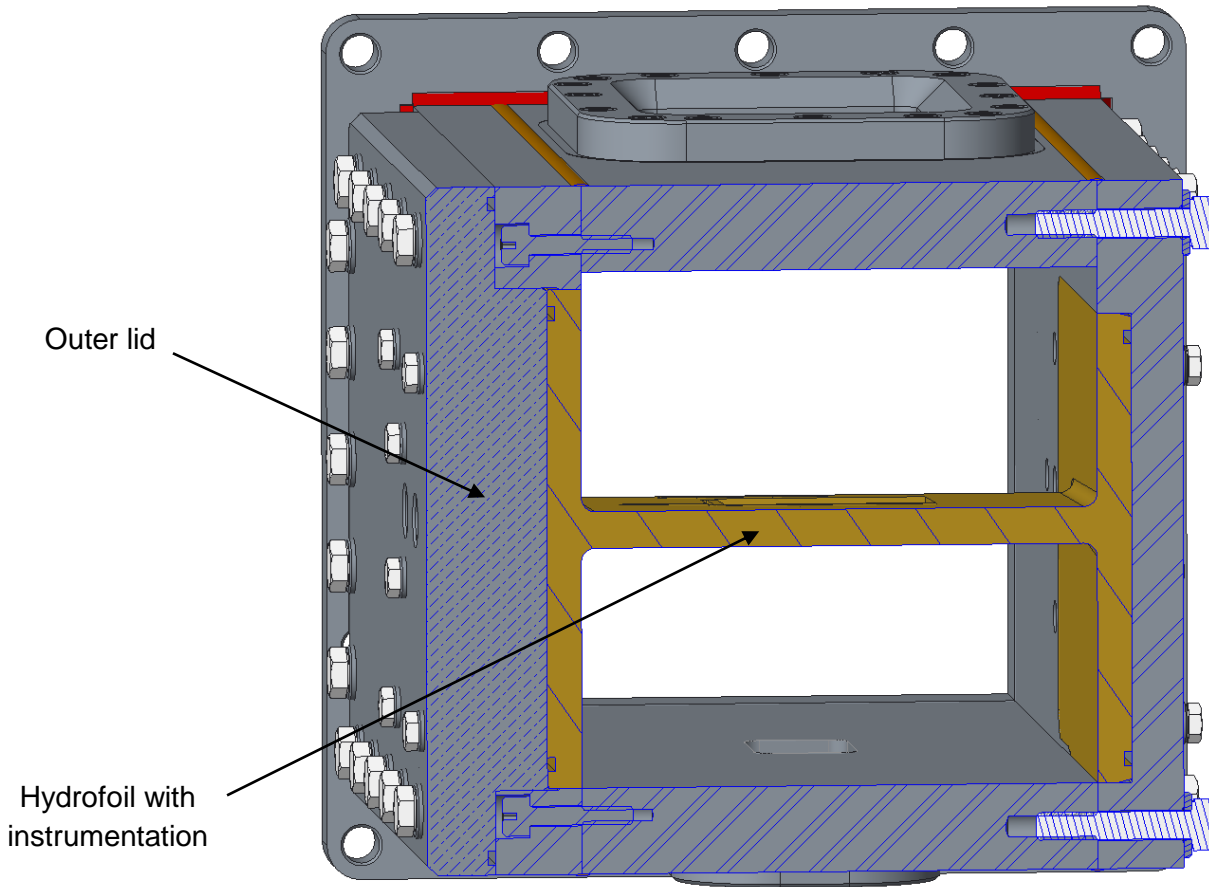
Hydrofoil installation

Outer lid

Hydrofoil with
instrumentation

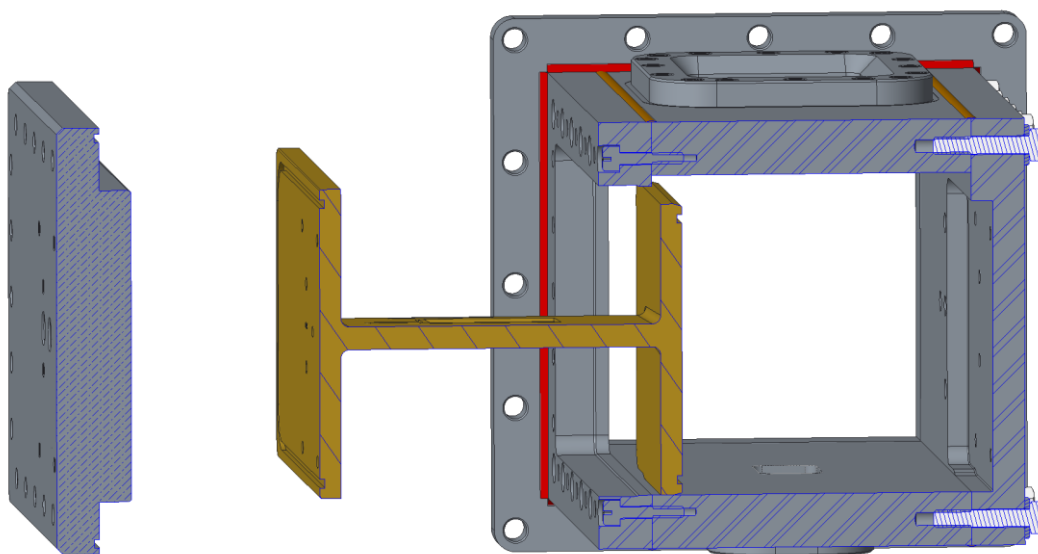*Figure 10 Span wise cross section (assembled)*

Figure 11 Span wise cross section (disassembled)

As seen in Figure 10 and 10 the test section is design to ease the installation and modification of the hydrofoil. The hydrofoil will rest against the socket in the back wall and a torque tightening of the front bolts will be used. The hydrofoil is milled from a solid block of Certal, an aluminium alloy. The material was chosen in order to improve the response to the excitation.

2.4.   Downstream diffuser
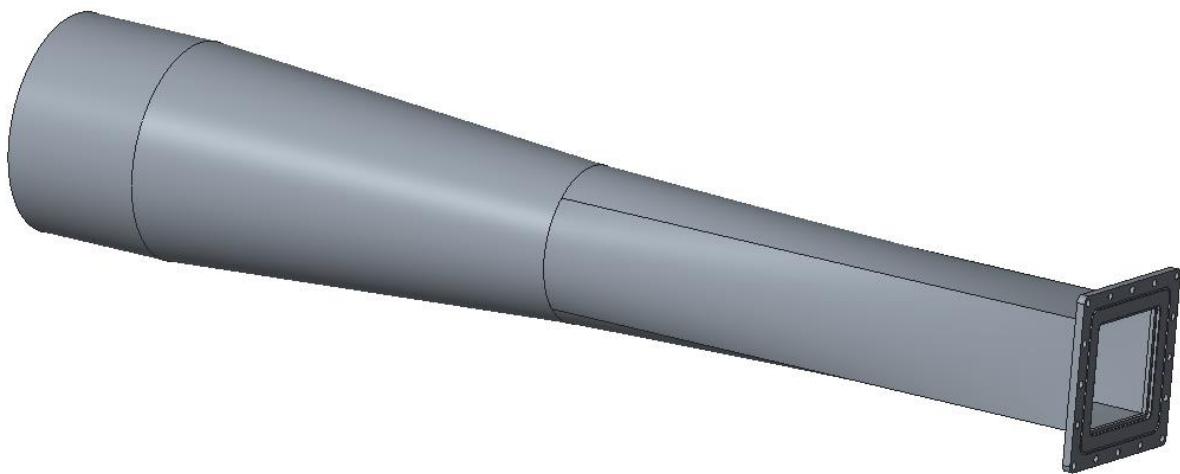

Figure 12 Downstream diffuser

The downstream diffuser changes the cross section from 150x150mm to a circular Ø300 pipe over two steps. First from 150x150 to Ø214 over 860mm, then from Ø214 to Ø300 over 640mm. This was done due to limitations in the manufacturing equipment. The design has been checked through CFD and found not to cause any separation at the highest flow velocity.

Appendix C - MATLAB script, FFT

The Matlab script containing the fast Fourier transform used to obtain amplitude-frequency plots from the simulated time-signal. The code was provided by Kristian Sagmo.

```matlab
function [Amp f] = FFTpwelch(x,Fs,varargin);
%   FFTPWELCH Welch's power spectral density estimate with amplitude
%   correction
%
%   Does an powerspectrum with pwelch function. Replaces PSD function in
%   Matlab.
%   Hanning window is set as default
%   Returns frequency and peak amplitudes (Vpk).
%
%   [Amp f] = FFTPWELCH(X, FS) returns an amplitude spectrum from the data
%   series X based on the logging frequency FS.
%
%   [Amp f] = FFTPWELCH(X, FS, FEXP) returns an amplitude spectrum from the
%   data
%   series X based on the logging frequency FS. FEXP is the expected
%   frecuency
%   of interest. It will adjust the window size based on this frequency. If
%   FEXP = [5 15]. The second input can be used to increase window size if
%   necessary.
%
%   [Amp f] = FFTPWELCH(X, FS, FEXP, WINDOW) returns an amplitude spectrum
%   from the data
%   series X based on the logging frequency FS. Define a WINDOW which
%   should be used. Hanning window is set as default. FEXP will not change
%   the input window.
%
%   [Amp f] = FFTPWELCH(X, FS, FEXP, WINDOW, NOVERLAP) returns an amplitude
%   spectrum from the data
%   series X based on the logging frequency FS. NOVERLAP will define the
%   overlap between window. Must between 0 and 1. This will increase number
%   of windows FEXP will not change the input window.

nfft = length(x);                   % number of samples
k = length(varargin);

if isempty(varargin);
%     fexp = 1;                        % fexp expected frequency of interest
%     estimateF = 1/fexp*Fs;
%     segmentsize=round(estimateF*10); % calculating window size. Should be
%   minimum 5 times the period
%     window = hanning(segmentsize);  % implementing Hanning-window as
%   default
%     noverlap = 0.5*segmentsize;     % overlap is 50% by default
    window = hanning(nfft);  % implementing Hanning-window as default
    noverlap = 0.5*nfft;     % overlap is 50% by default
elseif k == 1;
    in=varargin{1};
    estimateF = 1/in(1)*Fs;
    if length(in) == 2;
        segmentsize=round(estimateF*in(2)); % calculating window size.
            Should be minimum 5 times the period
    else
```

```matlab
            segmentsize=round(estimateF*10);
        end
        window = hanning(segmentsize);    % implementing Hanning-window as default
        noverlap = 0.5*segmentsize;       % overlap is 50% by default
elseif k==2;
%        fexp=varargin{1};
        window=varargin{2};
        noverlap = 0.5*length(window);       % overlap is 50% by default
else k==3;
%        fexp=varargin{1};
        window=varargin{2};
        noverlap=varargin{3}*length(window);
end
windowp=window;
noverlap2=noverlap;


probability = 0.95;                % Probalility for uncertainty band.
[pxx,f,pxxc] = pwelch(x,window,noverlap,nfft,Fs,'ConfidenceLevel',
    probability);
% pxx is the power spectrum density [V^2/Hz]
S1=sum(window);
S2=sum(window.^2);
ENBW=Fs*(S2/(S1^2));               % ENBW is the equivalent noise bandwidth [V
    ^2]
pxx=pxx*ENBW;                      % Power spectrum
Amp=sqrt(pxx)*sqrt(2);            % Linear spectrum/amplitude spectrum [V].
    Vpk = Vrms*sqrt(2);

end
```

Appendix D - Idun job script

```bash
#!/bin/bash

#SBATCH --job-name=finemeshSST
#SBATCH -t 300:00:00
#SBATCH --nodes=6 --ntasks-per-node=20
#SBATCH --partition=WORKQ
#SBATCH --mem=120000
#SBATCH --mail-type=ALL
#SBATCH --mail-user=solveite@stud.ntnu.no

#SBATCH --output=%j.out
#SBATCH --error=%j.err

## Recommended safety settings:
set -o errexit # Make bash exit on any error
set -o nounset # Treat unset variables as errors

# make sure the directory with chat case exists
# by setting the enviornmental variable ${w} to
# the subdirectory and test for its existence
# w=/cluster/work/users/$USER/$SLURM_JOB_NAME
# if [ ! -d $w ]; then mkdir -p $w;fi
# cd $w

cd /home/$USER/$SLURM_JOB_NAME

## create host list
srun hostname -s | sort > /tmp/hosts.${SLURM_JOB_ID}
nodes=`tr '\n' ',' < /tmp/hosts.${SLURM_JOB_ID}`

# echo "nodes= "$nodes

module load CFX/19.2

export CFX5RSH=ssh

## Run the application
cfx5solve -mdef CFX.mdef -double -parallel -batch -large -s 1.5 -start-method 'Intel MPI Distributed
Parallel' -par-dist $nodes

## clean up
rm /tmp/hosts.${SLURM_JOB_ID}
```

Appendix E - Risk Assessment

Hazardous activity identification process

Prepared by	Number	Date
HSE section	HMSRV2601E	09.01.2013
Approved by	Replaces	
The Rector		01.12.2006

Unit: *Department of Energy and Process Engineering*

Date: 05.06.2019

Line manager:

Participants in the identification process (including their function):

Short description of the main activity/main process: Master project for student Solveig Therese Elane.
Project title: CFD simulations in a blade cascade rig

Is the project work purely theoretical? (YES/NO): YES   Answer "YES" implies that supervisor is assured that no activities
requiring risk assessment are involved in the work. If YES, briefly describe the activities below. The risk assessment form need not be filled out.

Signatures: *Responsible supervisor:*   Student: *Solveig Therese Elane*

ID nr.	Activity/process	Responsible person	Existing documentation	Existing safety measures	Laws, regulations etc.	Comment
	Numerical analysis	Solveig T. Elane				